Ministry of Higher Education and Scientific

 Research

University of Technology

Electromechanical Engineering Department

Mechanical Property Modelling Of Steels

A thesis

Submitted to the Department of Electromechanical Engineering/ University of Technology in a partial fulfilment of the requirements for the degree of Doctor of philosophy in Engineering Instructional Technology/ Mechanical Engineering

By

Aseel Abdulbaky Al-Hamdany

2010

(25)

(   )

In the name of Allah, Most Gracious, Most Merciful

We sent aforetime our Messengers with Clear Signs and sent down with them the Book and the Balance (of Right and Wrong), that men many stand forth in justice; and We sent down Iron, in which there is awesome power, as well as many benefits for mankind, that Allah may test who it is that will help, unseen Him and His Messengers: for Allah is full of strength, Exalted in Might (and able to enforce His Will).

Life is a series of experiences, each of which makes us bigger, even though it is hard to realize this. For the world was built to develop character, and we must learn that the setbacks and grieves which we endure help us in our marching onward.

Henry Ford

To my parents & my aunt

With my all respect, appreciation, and love.

Aseel

Acknowledgement

Abstract

The purpose of this research programme is to develop quantitative models for the prediction of mechanical properties (hardness and fracture toughness) using experimental data collected from the literature, together with a powerful computational technique known as neural network. Creating a truly general model requires a combination of available data and metallurgical knowledge. These models are proposed for martensitic and ordinary bainitic steels in addition to the more recent class of non-structural super-bainitic steels. Super-bainitic steels are attractive for many applications such as armour.

Three general neural-network models are developed for the estimation of hardness, volume percent of bainite and fracture toughness. The first model of hardness is validated through new experiments, carried out in this work, for certain types of steels. The model gave precise predictions. The second neural network model is successfully used to predict the volume percent of bainite for a wide range of steels including super-bainitic steels. The third model of fracture toughness, whether based on mechanical properties alone or chemical composition alone did not yield good predictions for plane-strain fracture toughness. However, a refined version of this last model based on chemical composition, heat treatment and mechanical properties is proposed. The predictions of fracture toughness are generally acceptable but the uncertainties are high and more input data need to be collected for super-bainitic steels when available in the future to improve the predictions of this model.

For verification of the hardness model, some experiments were carried out in this investigation on different steels. It is possible, through the application of thermodynamics and kinetics principles, to control the microstructure and study the variation in mechanical properties. Accordingly, one of the alloys studied was free from thermal cracks and has been recommended for use in the automobile industry. Reduction of the austenitisation temperature to a level just above the upper critical temperature (A_{e3}) reduced the probability of the appearance of thermal cracks after direct quenching.

The super-bainitic microstructure of a high carbon, high silicon low alloy steel was found to be resistant to tempering, and the hardness and tensile properties of the alloy was not greatly affected by tempering. Fracture toughness however showed in general a decrease with increasing tempering temperature.

An instructional package was also designed and executed to study the principles of the phase of bainite and neural network it was found that the instructional package has a great effect on learner's behavior in steels learning.

Contents

Chapter 1

Introduction

1.1 Introduction

There are so many phases changes that occur in steels that it is possible to generate many varieties of microstructures and mechanical properties [1]. This permits a wide range of applications but the complexity makes it difficult to understand and design from first principles.

The aim of this thesis is to understand the phase transformation diagrams for a certain class of steels, and to study the effect of the microstructure on the mechanical properties. Also it is intended to develop quantitative models for the complex properties using experimental data collected from the literature, together with a powerful computational technique known as neural network analysis to estimate the mechanical properties (hardness and fracture toughness) as a function of many material variables.

Creating a model using this method requires a large amount of data and it is sometimes not possible to accomplish this task easily. Creating a

truly general model requires a combination of data and metallurgical knowledge. In building these models, the intention was to include data for super-bainitic steels (high carbon high silicon low transformation temperature bainite) in addition to the ordinary bainitic and martensitic steels. Super-bainitic steels have found application in armour because of their ballistic properties [2, 3].

Some examples of neural network models are as follows. Yescas-González has recently completed a model about the Vickers hardness in austempered ductile irons [4]. Many models have been developed in recent years. They are summerized in Dimitriu's thesis [5]. The latter includes prediction of the creep strength of austenitic stainless steel [6], modelling precipitation sequences in power plant steels [7, 8], irradiation hardening in low activation steels [9], the martensite-start temperature of steels [10], the Charpy toughness [11], modelling recrystallization in mechanically alloyed materials [12], the mechanical properties of hot rolled steels [13], and of the yield stress in highly irradiated ferritic steels [14].

Bayesian neural networks is adopted in this work in order to handle complex data and modelling uncertainties. The hardness, fracture toughness and bainite volume percent are modelled as a function of chemical composition and heat treatment. Some experimental work is carried out on specific steels to verify the output of the models.

1.2   Research work layout

This thesis contains eight chapters, the first one being the current chapter:

Chapter two describes the physical metallurgy of bainite (ordinary and super-bainitic) and its mechanical properties, followed by part two, which covers Bayesian neural network theory.

Chapter three includes details about the experimental work involving hardness and plane strain fracture toughness determinations.

Chapter four describes the neural network model which enables the estimation of hardness as a function of chemical composition, heat treatment and bainite volume fraction.

Chapter five deals with the estimation of the volume percent of bainite as a function of chemical composition, heat treatment and hardness.

 Chapter six concerns the construction of a neural network model which estimates the fracture toughness K_{Ic} in steels as a function of chemical composition, heat treatment and other mechanical properties.

Chapter seven presents the results of the experimental work.

Chapter eight has the conclusions of the work and lists suggestions for future subjects of research.

Chapter 2

Microstructure & Modelling: Review

The objective of this chapter is to reveal the mechanism of the formation of the structure of bainite and how it affects the mechanical properties. It is also intended to introduce neural network theory and how it can be used to represent complex relationships.

Transformation and Microstructure of Bainite

2.1 Bainite

It is found that bainite forms during the decomposition of austenite over a wide range of temperatures (200-550) °C. Neither pearlite nor martensite phases are formed during this transformation depending of course, on the composition of the steel. Figure 2.1 shows the time-temperature-transformation (TTT) diagram which consists of two separate C-shaped curves. The one at high temperatures describes the evolution of diffusional transformation phases such as ferrite and pearlite, the lower C- curve represents displacive reactions such as Widmanst tten ferrite, bainite and martensite (martensite forms below the M_s temperature). Bainite also forms during athermal treatments at

cooling rates too fast for pearlite to form and not rapid enough to produce martensite [15].

The microstructures of bainite are classified according to morphology, as upper and lower bainite as shown in figure 2.2. Upper and lower bainite consists of clusters of platelets of ferrite which share identical crystallographic orientation and which are intimately connected to the parent austenite phase in which they grow. Very thin bainitic plates are called subunits and they grow in clusters known as sheaves. Within each sheaf, the subunits are parallel and of identical crystallographic orientation and habit plane. Each bainitic ferrite plate is about 10 μm long and 0.2 μm thick [16].
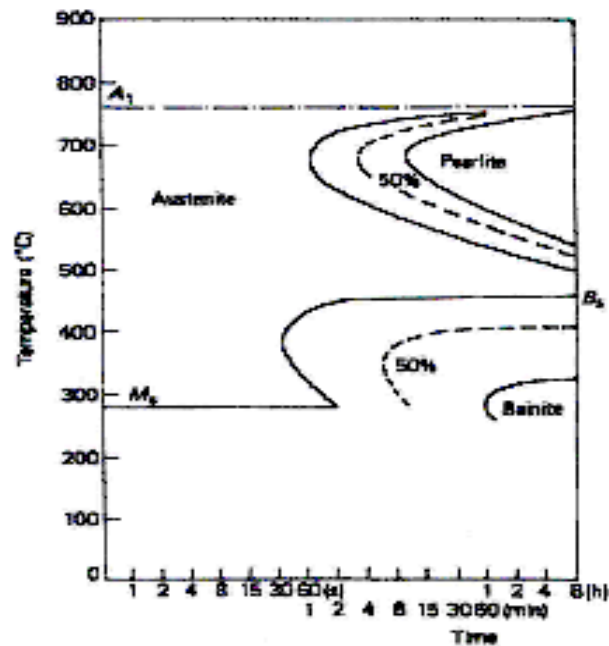
Figure 2.1: TTT curve for a Fe-0.5C-3Cr (wt%) steel [17].
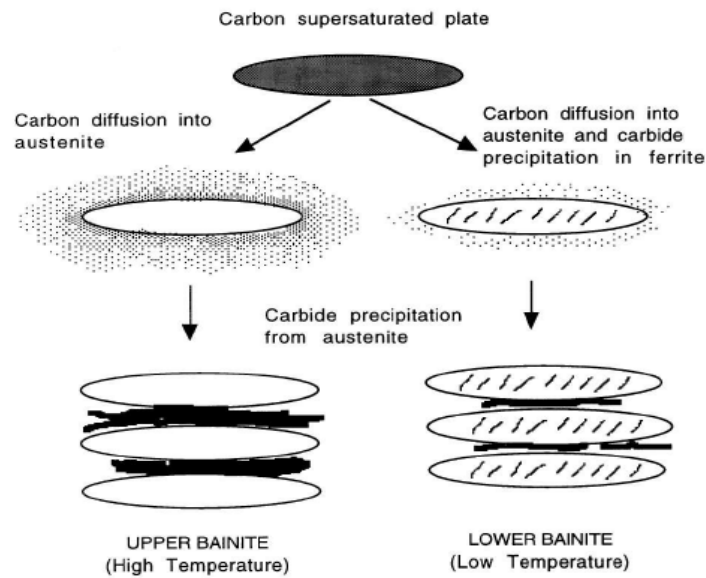
Figure 2.2: Illustration of upper and lower bainite showing the main differences in carbon partitioning and precipitation [18].

2.2 Mechanisms of transformation

There are two mechanisms of solid-state transformation in steel as shown in figure 2.3. The transformation of bainite is displacive (shear) with no diffusion of iron atoms and substitutional elements [16, 19], so atoms move in a disciplined manner in order to change the crystal structure from face-centred cubic (fcc) to body-centred cubic (bcc) or body-centred tetragonal (bct).

It is observed that the bainite phase forms at temperatures lower than that necessary for Widmanst tten ferrite to form [16]. Widmanst tten ferrite has the same mechanism of transformation as bainite (displacive) but the carbon must diffuse during paraequilibrium nucleation and growth. In contrast, with bainite carbon diffuses during paraequilibrium nucleation but growth is diffusionless.

As a result of transformation, surface relief has been observed in steels that undergo either the bainite or the Widmanstätten ferrite transformation [16]. Swallow and Bhadeshia directly observed the deformations [20]. However, the conclusive aspect concerning the evolution of these intermediate displacive transformation products is the kinetics associated with carbon partitioning.

Bhadeshia envisaged that both bainite and Widmanstätten ferrite have the same nucleus [16]. The stored energy for bainite and Widmanstätten ferrite are about 400 J mol^{-1} and 50 J mol^{-1} respectively [21]. The chemical free energy change has to be sufficient as to exceed the stored energy for a transformation to take place.

The much higher stored energy in bainite was explained in terms of the absence of favourable strain interactions `within' bainite sheaves [21]. Bainite growth is diffusionless but the transformation is able to occur above M_s because nucleation involves the partitions of carbon and hence has a larger driving force than the diffusionless nucleation of martensite [21].

Speer *et al.* [22, 23], Muddle and Nie [24] and Saha *et al.* [25] proposed the same growth mechanism for bainite, that bainite may grow by a martensitic growth mechanism which is diffusionless followed by, or along with, carbon partitioning into austenite with overall kinetics controlled by carbon diffusion. Table 1 summarises the essential details of the mechanisms of displacive transformations for Widmanstätten ferrite, bainite and martensite.
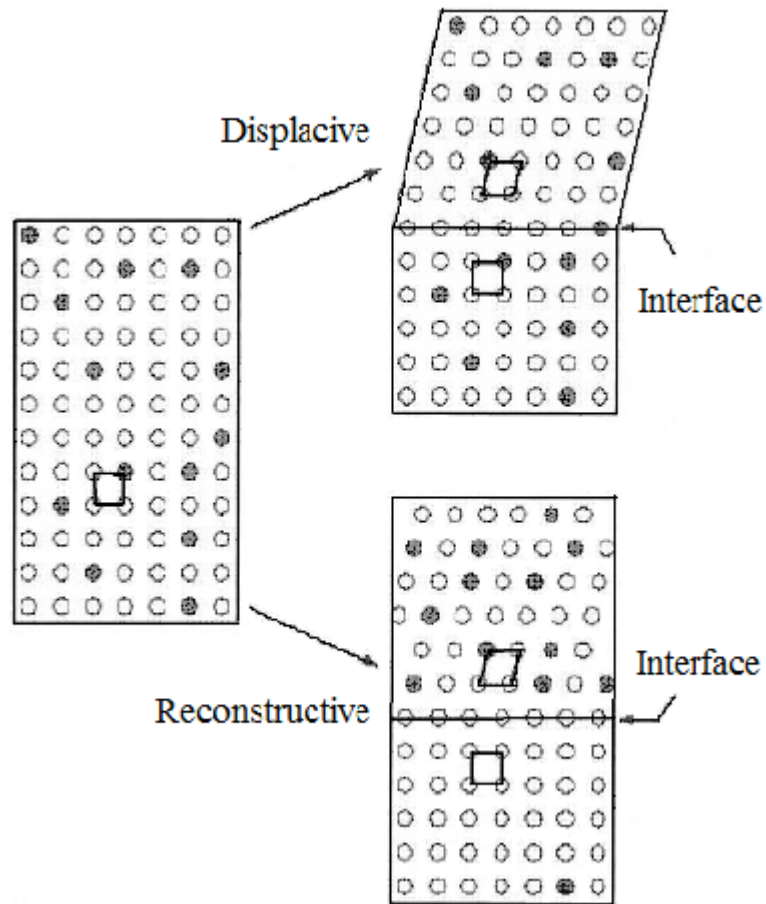
Figure 2.3: Schematic illustration of the types of transformation in steels [17].

Table 2.1: Mechanisms of displacive transformations [26].

Phase	Martensite $\in_c$	Bainite $\in_b$	Widmanstätten ferrite $\in_w$
Nucleation	Diffusionless	Paraequilibrium[1]	Paraequilibrium
Growth	Diffusionless	Diffusionless	Paraequilibrium

2.3 The T_0 concept

The structure of a bainitic steel is composed of retained austenite, bainitic ferrite and carbides. Carbides, however, can be suppressed by alloying with elements such as Si, Al and P [27, 28]. It is essential to understand the issues governing the formation of carbides in different varieties of steel and the mechanical properties achievable in greater detail.

The diffusionless mechanism of bainite growth has to occur at a temperature just below T_0 as shown in figure 2.4 when the free energy of bainitic ferrite drops below that of austenite of the same composition. The stored energy in bainitic ferrite is accounted for by raising its free energy curve by an amount equal to the strain energy due to transformation, giving the T_0' curve, figure 2.4.

The excess carbon in the bainite partitions into the residual austenite during isothermal transformation, forcing the next plate to grow

---

[1] Paraequilibrium implies partitioning of carbon between parent and product phases, subject to constraint that the ratio of substitutional solute to iron atoms in maintained constant.

from carbon-enriched austenite [16]. As the austenite carbon content reaches the T_0^C value, the process finally stops leading to the so-called incomplete reaction phenomenon [29]. It is important to realise that this scenario is valid only for carbide-free bainitic steels, since otherwise, the precipitation of cementite permits the reaction to proceed to completion.

Application of the lever-rule gives:

$$V_b = \frac{x_{T_0^C} - \bar{x}}{x_{T_0^C} - x_{\in_b}} \tag{2.1}$$

where V_b the volume fraction of bainite, $x_{T_0^C}$ the austenite carbon content given by the T_0^C boundary, $\bar{x}$ is the alloy average carbon concentration and $x_{\in_b}$ is the carbon concentration of the bainite.
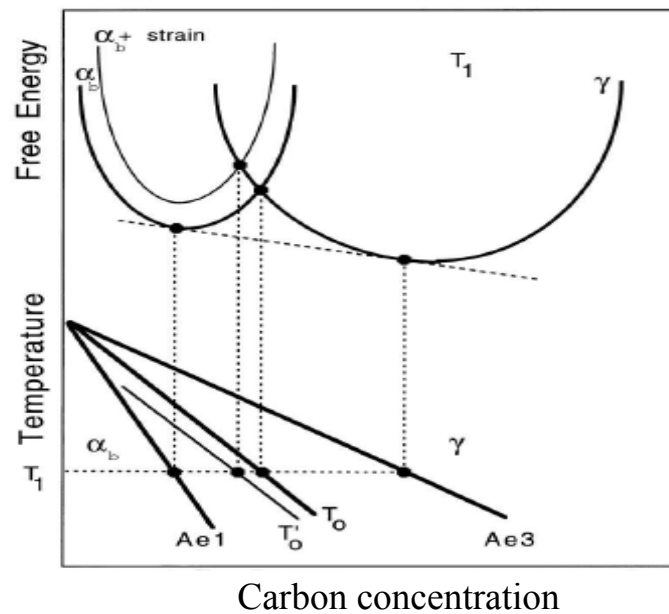
Figure 2.4: Schematic illustration of the construction of the T_0 and T_0^C curves [16]. T_1 is the temperature corresponding to the free energy curves, A_{e1} refers to the equilibrium (γ+α)/α phase boundary and A_{e3} refers to the equilibrium (γ+α)/γ.

The thermodynamic restriction imposed by the T_0^C curve on the extent of bainite transformation can result in the formation of pools of retained austenite with a coarse, blocky morphology. However, austenite also appears in the form of thin films trapped in between bainite plates, as shown in figure 2.5.
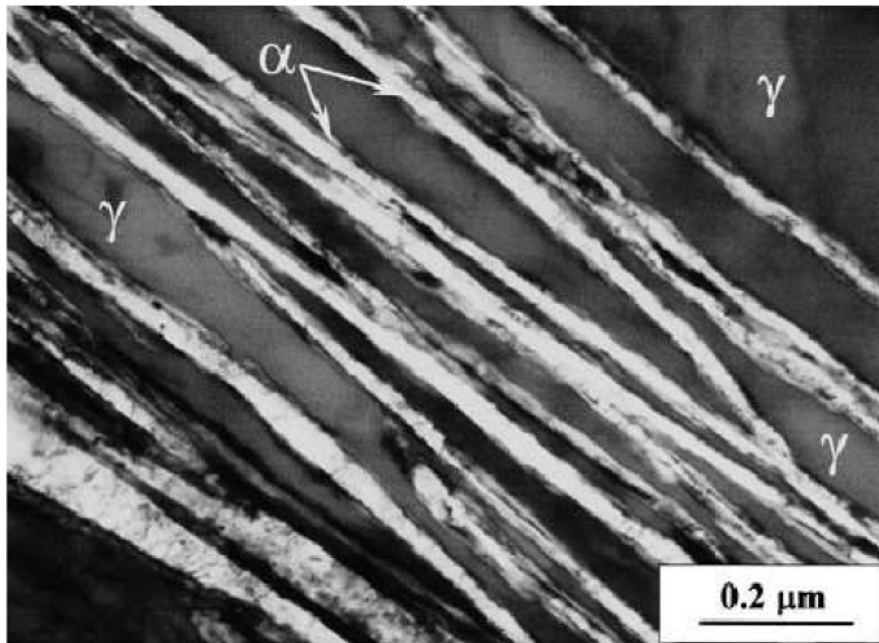
Figure 2.5: Bright-field TEM (transmission electron microscope) micrograph showing the fine scale of retained austenite films (γ) and a bainitic plates (α) [21].

2.4 Isothermal Transformation to Bainite

The mechanical properties of carbide-free bainite are dependent on the phase fraction and carbon concentration of retained austenite; both of which are dependent on the temperature and time of transformation [29-32].

The effect of the bainite transformation temperature on the extent of transformation is shown in figure 2.6 for the same holding time. It is clear that the fraction of bainite transformed is greater at higher temperatures. Figure 2.6 also shows that silicon enhances the retention of the residual austenite. Large concentrations of silicon in all the steels developed to generate super-bainite (nanostructured bainite) prevent the precipitation of cementite during the course of transformation [2, 33-36].

It may be possible to use lower concentrations and yet maintain a carbide-free phase mixture, but the theory necessary to reach this conclusion is not established.
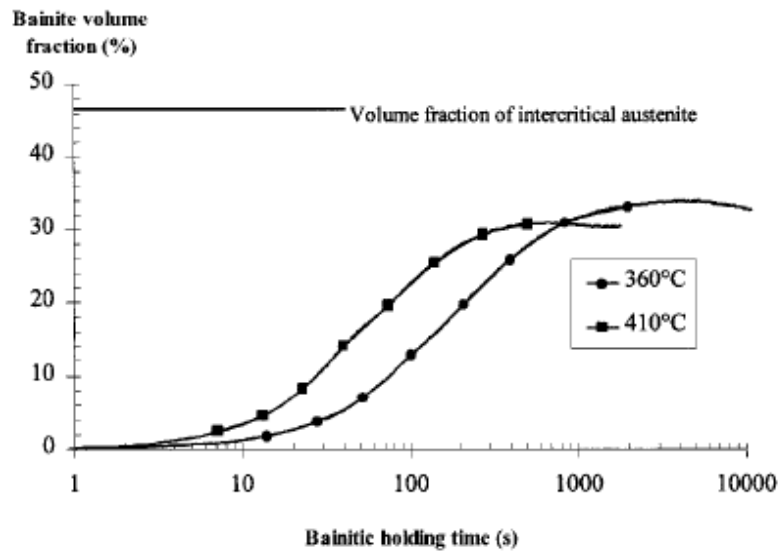
(a) High Si
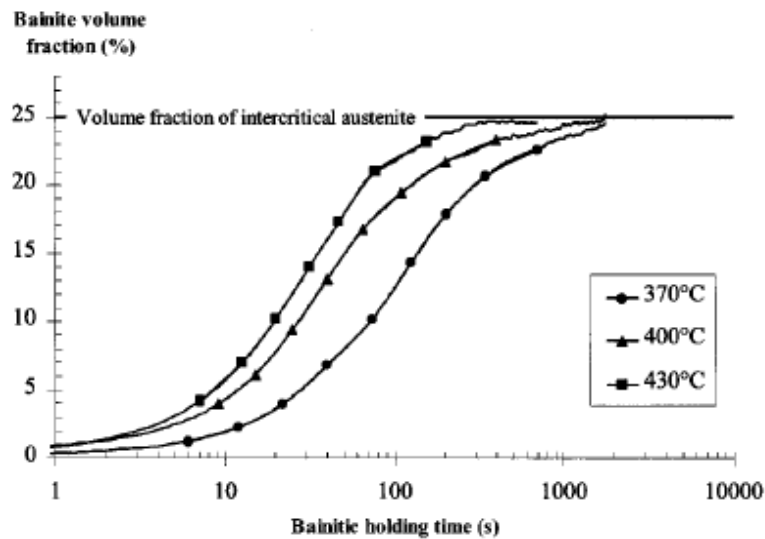
(b) Low Si

Figure 2.6: Volume fraction of bainite as a function of transformation time for (a) Fe-0.29C-1.4Mn-1.5Si; (b) Fe-0.16C-1.3Mn-0.38Si (wt%) [28].

2.5 Super Bainite

It would be nice to have a strong material which can be used for making components which are large in three dimensions and which do not require mechanical processing or rapid cooling to reach the desired properties. A steel designed on this basis has been manufactured and characterized by Caballero *et al.* [30] and Garcia-Mateo *et al.* [21, 31]. Many researches [5, 18-22] have developed a high carbon-high silicon carbide-free bainite with very thin austenite films forming an intimate composite, with a controlling scale of 20-30 nm.

The strength of bainite comes from the fine scale of the structure. There is a considerable plastic relaxation in the austenite adjacent to the bainite plates, figure 2.7. The dislocations generated in this process resist the advance of the bainite/austenite interface, the resistance being greatest for strong austenite. The strength of austenite is the most important factor which determines the thickness of bainite [32]. Because of that, the plates become thicker at high transformation temperatures since the yield strength of the austenite will then be lower.

There are also other factors such as the driving force and the transformation temperature itself [32]. A large driving force increases the nucleation rates. As a result, a larger driving force also leads to a finer microstructure [37]. Though austenite strength is the most important factor that determines the thickness of the bainite, austenite strength and free energy change during transformation are both influenced by temperature. A lower transformation temperature makes austenite strong and the driving force large. This leads to thinner plates of bainite. In order to get extremely fine bainite, it is necessary to transform at low temperatures. There are two equations which account for the relationship

between strength and grain size. One is the Hall-Petch equation and the other is due to Langford and Cohen. When the slip distance is less than about 1μm, the Langford and Cohen relationship is more reasonable [33]. For a given thickness t of a plate the mean linear intercept, $\bar{L}$, is roughly two times the thickness and the strength contribution ∞O due to the size of the plate is given by

$$\infty\Theta \quad 115\left(\bar{L}\right)^{21} \quad \text{MPa} \tag{2.2}$$

where $\bar{L}$ is in micrometers according to Langford and Cohen relationship [33]. That means it is possible to get $\Delta\sigma$=311 MPa for plates of thickness 185 nm, whereas $\Delta\sigma$=1642 MPa for plates of thickness 32 nm, giving an additional strength of more than 1 GPa without sacrificing toughness. Extremely fine bainitic structures which consist of bainite plates and carbon-enriched austenite without carbide precipitation have been developed [30, 34, 35]. The microstructure exhibits an excellent combination of strength and ductility. The strength comes mainly from the fine scale of the structure rather than carbon, even though the steels contain about 1 wt % of carbon.
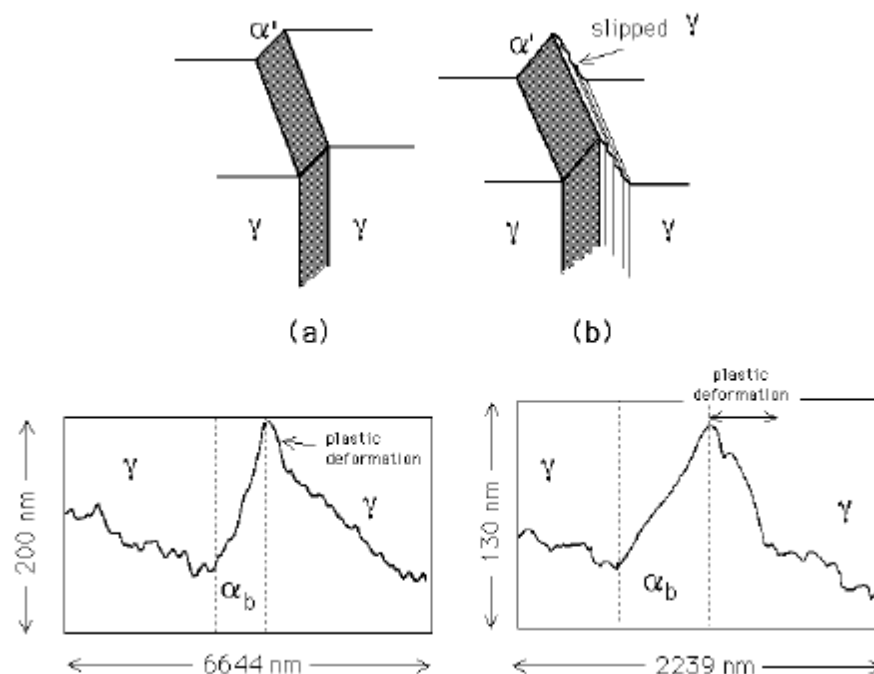
Figure 2.7: (a) A perfect invariant plane strain surface relief effect. (b) One where plastic relaxation of the shape change occurs in the adjacent matrix. (c), (d) An actual atomic force microscope scan across the surface relief due to a bainite sub-unit, the planes were flat before bainitic transformation [20, 28].

The applications, advantages, mechanical properties, characteristics and design strategies of these extremely fine, carbide-free bainitic structures are well documented [2, 3, 36, 38, 39]. Ultimate tensile strengths of 2500 MPa have been routinely obtained with ductilities in the range 5-30 % and toughness in excess of 30-40 MPa m$^{1/2}$. The bainite is also the hardest ever achieved, about 700 HV.

The most useful advantage of the steel is the simple way in which the process avoids rapid cooling so that residual stresses are avoided, even in large pieces. There are many adjectives that have been given to the bainitic microstructure described above: cold bainite, hard bainite, strong bainite and super bainite [36].

2.6 Tempering of Bainite

The microstructure and properties can change during tempering and this is dependent on how the sample deviates from equilibrium. The behaviour of bainite during tempering is expected to be different from that of martensite.

Rapid softening occurs when the plate-like structure of ferrite changes into equiaxed ferrite and the coarsening of cementite is associated with this change [16]. Further tempering has minimal effects.

Carbon is a very effective solid solution strengthener so the strength of martensite drops sharply as the carbon precipitates during tempering [16, 17]. With bainite the carbon is mostly present as coarse carbides which contribute little to strength.

Tempering of mixture of bainite ferrite and carbon-enriched returned austenite usually at temperatures in excess of 400 °C, induces the decomposition of the austenite into a mixture of ferrite and carbides. Secondary hardening occurs when fine (more stable) alloy carbides form, such as Cr, V, Mo and Nb at the expense of cementite. The secondary hardening reaction tends to be sluggish when compared with martensite, because the alloy carbides require the diffusion of substitutional solutes.

The hardness and tensile strength of fully bainitic microstructures decrease during tempering; the rate of change is large for lower bainite which has higher starting hardness. As might be expected, it is the highest strength steels which undergo the largest change in strength during tempering. The yield strength is found to be low in bainitic steels containing retained austenite due to the mixed microstructure and the presence of free dislocations.

Bhadeshia envisaged that there are significant differences in the tempering behaviour for both bainite and martensite [16].

2.7 Mechanical properties

There were difficulties in obtaining fully bainitic microstructures in sizeable samples of steel. It has long been recognised that the influence of bainite on the mechanical behaviour of steel is difficult to understand because of the inability to attain fully bainitic microstructures at all transformation temperatures, a consequence of the incomplete reaction phenomenon.

2.7.1 The Strength of Bainite

The strength of bainite can be factorized into a number of intrinsic components [16, 40]:

$$\sigma = \sigma_{Fe} + \sum_i \sigma_{ss} + \sigma_c + K_L \bar{L}^{-1} + K_D \rho_D^{0.5} + K_p \bar{\Delta}^{-1} \tag{2.3}$$

where c_i is the concentration of a substitutional solute which is represented here by a subscript (i); the other terms in this equation are K_L coefficient for strengthening due to lath size, 115 MN m^{-1}, assuming that the cementite particles are spherical and of uniform size, K_p is given approximately by 0.52 V_θ MPa, where V_θ is the volume fraction of cementite, K_D the coefficient for strengthening due to dislocations, 7.34×10^{-6} MN m^{-1}, the strength of pure annealed iron σ_{Fe}, substitutional solid solution strengthening contributions σ_{ss}, strengthening due to carbon in solid solution σ_c, and a variety of microstructural components, ρ_D dislocation density, typically 10^{16} m^{-2}, $\bar{L}$ is a measure of the ferrite plate size, typically 0.2 μm.

2.7.2 Hardness

The hardness of bainite increases linearly with the carbon concentration. The austenitising temperature does not influence the hardness unless it is not high enough to dissolve all the carbides [41]. For mixed microstructures, the hardness depends on the transformation temperature and composition [42]. This is because the stability of the residual austenite to martensitic transformation changes with carbon concentration, the limiting value of which depends on the transformation temperature according to the T_o curve of the phase diagram.

Figure 2.8 shows that for a series of Fe-Cr-C alloys, the hardness for the 0.08 wt% C alloy is insensitive to the isothermal transformation temperature. The low carbon concentration ensures that the microstructure is almost fully bainitic for all temperatures studied.

This contrasts with higher carbon alloys, where the hardness first decreases as the transformation temperature is reduced; this is because the fraction of bainite increases at the expense of residual phases like martensite and pearlite.

The micro-hardness of bainite, in a mixed microstructure of bainite and pearlite obtained by isothermal transformation, is found to be less than that of the pearlite, figure 2.9. This remains the case even when the pearlite and bainite have been generated at the same temperature. This behaviour is easy to explain once it is realised that the pearlite grows from carbon-enriched austenite and hence contains a much larger fraction of cementite than the bainite.

The hardness of bainite is insensitive to the austenite grain size, even though the latter influences the bainite sheaf thickness.

This is expected since the bainite sub-units size is hardly influenced by the austenite grain size. Since the sub-units are much

smaller, they exert an overriding influence on strength. For the same reason, the hardness of fully bainitic microstructures is not sensitive to the austenitising temperature [16].
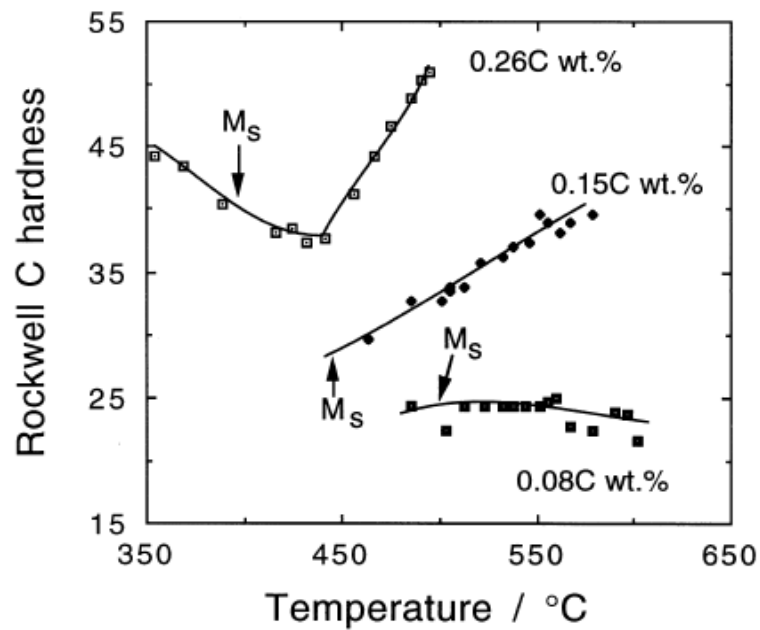
Figure 2.8: Variation in hardness as a function of the isothermal transformation temperature [16].
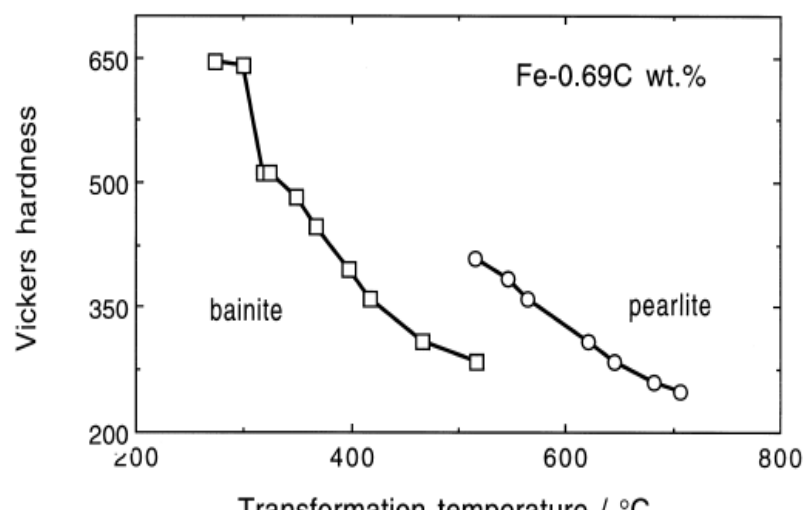
Figure 2.9: Micro-hardness data from plain carbon steels transformed isothermally to a mixture of bainite and pearlite [16].

2.7.3 Fracture Toughness

Fracture mechanics is a tool of engineering analysis that makes it possible to determine whether a crack of given length in a material of known fracture toughness is dangerous or not, and if it will propagate to failure at a given stress level. It also permits the selection of the design which is most resistant to fracture.

Most bainitic steels are used in high-strength applications, and failure is not usually accompanied by a large amount of plasticity, therefore elastic theory is used to represent the stresses.

Fracture toughness is an indication of the amount of stress intensity required to propagate a pre-existing flaw. It is an important material property since the occurrence of flaws is not completely avoidable in the processing, fabrication, or service of a material or component. Flaws may appear as cracks, voids, metallurgical inclusions, weld defects, design discontinuities, or some combination thereof. Since engineers can never be totally ensure that a material is flaw free, it is a common practice to assume that a flaw of some chosen size will be present in components and linear elastic fracture mechanics (LEFM) approach is used to design

critical components. This approach uses the flaw size and features, component geometry, loading conditions and the material property called fracture toughness to evaluate the ability of a component containing a flaw to resist fracture.

A single parameter called the stress intensity factor K represents the elastic stress field near a crack tip. The magnitude of this stress intensity factor depends on the geometry of the solid containing the crack, the size and location of the crack, and the distribution of the load imposed on the solid. The criterion for brittle fracture in the presence of a crack-like defect is that unstable rapid failure would occur when the stresses at the crack tip exceed a critical value. The crack tip stresses can be described by the stress intensity factor K, a critical value of which can be used to define the conditions for brittle failure.

The critical value of K is designated K_c which is considered as a material property that describes the inherent resistance of the material to failure in the presence of a crack-like defect. For a given type of loading and geometry, the relation is [43]:

$$K_{Ic} = \sigma Y \sqrt{a_c} \qquad (2.4)$$

where Y is a parameter which depends on specimen and crack geometry and a_c is the critical crack length. If K_{Ic} is known, it is possible to compute the maximum allowable stress for a given flaw size.

K_{Ic} is a basic material property in the same sense as yield strength. It changes with important variables such as temperature and strain rate. For the materials with a strong temperature and strain rate dependence, K_{Ic} usually decreases with decreasing temperature and increased strain rate. For a given alloy, K_{Ic} is strongly dependent on such metallurgical

variables as heat treatment, texture, melting practice, impurities inclusions, *etc.* [43].

There has been so much research activity and rapid development in the field of fracture toughness testing that in a period of few years, it has evolved from a research activity to a standardized procedure. In the discussion of the influence of a notch on fracture, it has been shown that a notch in a thick plate is far more damaging than in a thin plate because it leads to a plane strain state of stress with a high degree of triaxiality. The fracture toughness measured under plane strain condition is obtained under maximum constraint or material brittleness.

The plane strain fracture toughness when the crack is loaded in tensionis designated K_{Ic} and is a true material property. The minimum thickness to achieve plane strain conditions and valid K_{Ic} measurements is:

$$B = 2.5 \left(\frac{K_{Ic}}{\sigma_0} \right)^2 \qquad (2.5)$$

where σ_0 is the 0.2 percent offset yield strength.

Neural Network Modelling

2.8 Introduction

It is very important to understand the mechanical behaviour of metals. By using simple methods, it is possible to estimate, for example, the yield strength and elastic modulus, taking into account the size and distribution of defects and overall microstructure. When the number of variables becomes large and their effects are ill understood, it is very difficult to find a facility for estimating sophisticated properties. Neural networks have been used to deal with complex properties such as toughness [44, 45] and fatigue [46, 47].

A neural network is a powerful non-linear regression method [48-50]. The function to which the data are fitted is an outcome of the process. Neural networks are able to capture almost arbitrarily non-linear relationships.

2.8.1 Bayesian Neural Networks

Bayesian probability theory provides several benefits:

1. Solve the over-fitting problems using Bayesian method to control model complexity.
2. Find significance the weight variance σ_w of each input [49].

    The details of the operation and construction of neural networks has been reviewed elsewhere [48-54], but it is useful to summarise the main features here. It is assumed that the material property of interest, for example the plane strain fracture toughness K_{Ic}, can be expressed as a non-linear function, f, of a number of experimental variables in the database.

$$K_{Ic} = f(C_i, T_a, T_1, T_2, HV, \ldots) \tag{2.7}$$

where C_i represents the chemical composition of the steel, T_a is the austenitising temperature, T_1 and T_2 represent the transformation

temperature due to first and second stages, t_1 and t_2 the time incurred for the first and second stages of transformation, σ_y the yield stress of the material, σ_u the ultimate tensile stress, *HV* the Vickers hardness and "..." represents all the other parameters that might influence the K_{Ic}.

The purpose of neural network training is to make as few assumptions as possible about the form of a function, and attempting at the same time to find and copy its shape. In fact, the only assumptions are that the function is continuous and differentiable. It has been shown that a three-layer network of the form described below can produce such function [51, 54, 55]. The network is thus able to react flexibly to capture any non-linear interactions between the parameters.

2.8.2 Structure of neural network

The present work has been represented, as shown in figure 2.10, by a three-layer feed-forward network of the type used commonly for material property applications. The first layer consists of the inputs to the network; the next layer consists of a number of non-linear functions which form the "hidden" layer of neurons. h_i can be any non-linear, continuous and differentiable function, depending on the complexity of the model, hyperbolic tangents has been used in this work (Equation 2.8). Many hyperbolic tangents can be used if one function is not flexible enough to represent the complexity in the data. Figure 2.11 shows the summation of two hyperbolic tangents. The third layer consists of the output function, *y*. The hidden layer activation function for a neuron *i* is given by [51]:

$$h_i = \tanh\left(\sum_j w_{ij}^{(1)} x_j + \theta_i^{(1)} \right)$$

$$(2.8)$$

The output y is a linear combination of many hidden units h_i together with bias:

$$y = w^{(2)} + \sum_i h_i^{(2)} \quad N^{(2)} \tag{2.9}$$

The x_j are the inputs, and w the weights which define the network. $^{(1)}$ and $^{(2)}$ denote weights and biases in the hidden layer and in the output layer, respectively. The aim of training a network is to find the optimum values for w. The parameters θ are known as biases, and are like the constants that paper in regression analysis
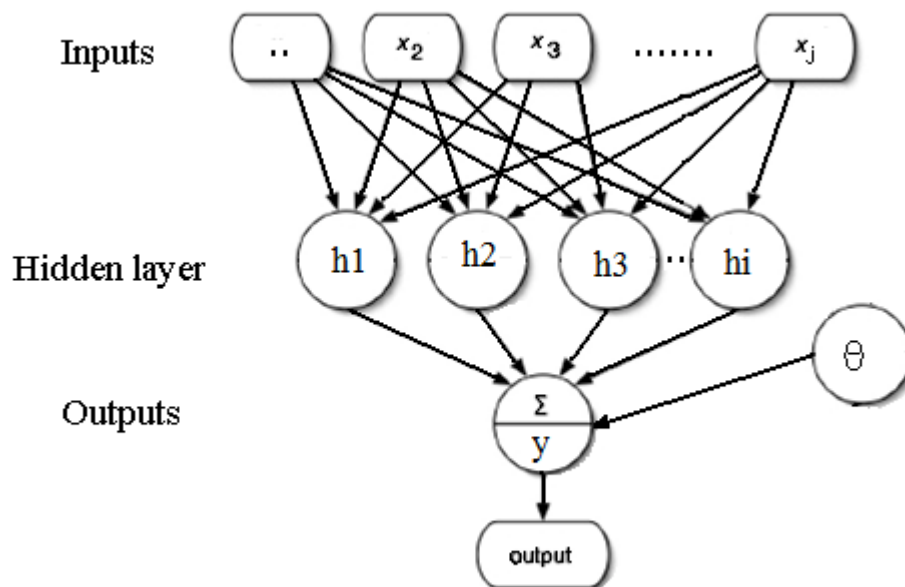
Figure 2.10: A schematic diagram of a three-layer feed-forward network. The model's complexity is controlled particularly by the number of neurons in the second layer, known as hidden units.
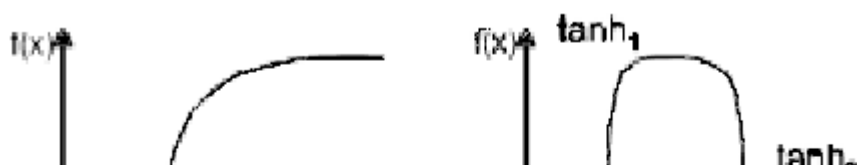
(a) (b)

Figure 2.11: (a) Flexibility of a hyperbolic tangent function. A model with one hidden unit (left) may not be sufficiently complex. (b) The combination of two hyperbolic tangent functions tanh$_1$ and tanh$_2$ can form a more complicated model (right) [55].

2.8.3 Training of neural network

The data are divided randomly into a training and testing set, and normalised within a range of ±0.5, in order to simplify the interpretation of the weight. The normalisation function is

$$x_j = 2\frac{x - x_{min}}{x_{max} - x_{min}} - 0.5 \qquad (2.10)$$

where x is the original value, x_{min} and x_{max} are the minimum and maximum values in the database for that input, and x_j is the normalised value. The purpose of normalising, which is not an essential for the neural network, is to give a convenient way to compare the results of predictions for different inputs each of which otherwise may have vastly different range.

The number of "hidden" units is related to the complexity of network models, as the number of hidden units increases the complexity increases. The trained network is not a black box because the inputs and outputs are known, and the weights can be examined, although they may

be difficult to interpret directly because of the complexity of non-liner problems. The best procedure is to steady a large number of trends in the predictions made using the trained network.

Due to the flexibility of neural network, there is the possibility of over-fitting the training data. Training a network therefore includes finding a set of weights and biases which minimise an objective function (Equation 2.11), and balances both of complexity and accuracy:

$$M(E) = E_{wD}$$ (2.11)

where E_w is a regulariser; it is a function which favours small values of w and thus encourages the model to find simpler solutions with less tendency to over-fitting, and is given by:

$$E_{W_{ij}} = \frac{1}{2} \sum_{ij}{}^2$$ (2.12)

E_D is the overall error given by:

$$E_{D} = \frac{1}{2} \sum_{k} \left({}^{kk} \right)^2$$ (2.13)

where t^k is the set of outputs for the set of inputs x^k, while y^k is the set of corresponding network outputs, α and β are control parameters which determine the complexity of the model. MacKay's algorithm allows the inference of these parameters from the data, permitting automatic control of the model complexity [48, 51]. Figure 2.12 shows a set of data which was split into training (the filled triangles) and testing (the stars) sets. Based on the training set, two models were trained. The first one (a) represents linear regression and it can be seen that it only gives a poor representation of both the training and the testing data. The second model

(b) represents a complex function which gives an excellent representation of the training data but a poor one for the testing data [5].

<div align="center">

(a) linear regression model   (b) over-fitted model
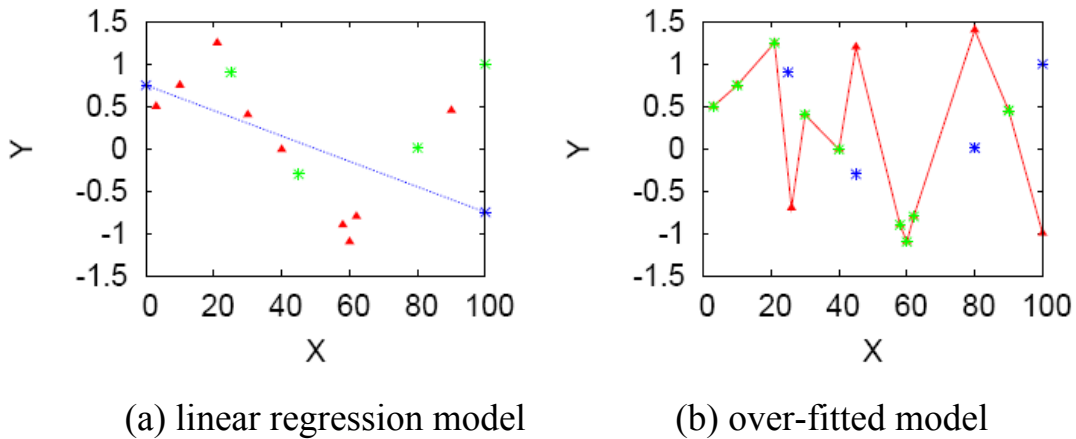
Figure 2.12: Under-fitting and over-fitting [5].

</div>

2.8.4 Optimization of model complexity

To carry through the training, the data are split at random into two sets, a training set and a test set. The model is trained on the training set, and then is compared against the test set of unseen data. Figure 2.13 shows how increasing the complexity continuously lowers the training error, while the test error goes through a minimum and increases again. As the model's complexity increases, over-fitting causes the test error to increase as the number of hidden units increases. The aim of the training is to minimise the test error against the data set and against new data not seen by the model.

For these models, the fitting method is based on a Bayesian approach and treats training as an inference problem, allowing estimates to be made of the uncertainty of the model fit figure 2.14. Rather than trying to identify one best set of weights, the algorithm infers a probability distribution for the weights from the data presented.
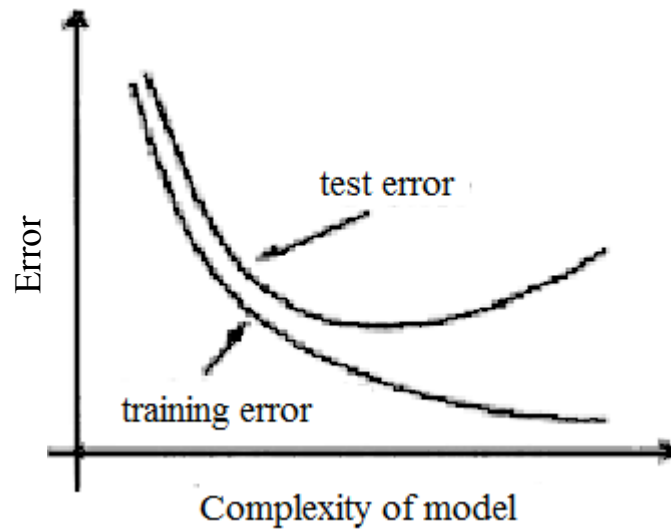
Figure 2.13 Comparison of error on training and testing set as a function of network complexity, illustrating the problem of over-complex models.

In this context, the performances of different models are best evaluated using the log predictive error (LPE) rather than the test error. This error penalises wild predictions to a lesser extent when they are accompanied by appropriately large error bars [51] and is defined by:

$$LPE = \frac{1}{2} \sum_{k} \left[\frac{\left(t^k - y^k \right)^2}{\left(O_y^k \right)^2} + \log\left(M \left(O_y^k \right)^2 \right) \right] \tag{2.14}$$

where t^k and y^k are as previously defined , and O_y^k is related to the uncertainty of fitting for the set of inputs x^k. Starting from the best model, the committee models are selected until the minimum test error is obtained.

Therefore the committee of models is used for a final prediction. The following formula gives the error bars for predictions using a

committee of the models. The prediction $\bar{y}$ of a committee of models is the mean prediction of its members, and the uncertainty is:

$$\sigma_{\bar{y}}^2 = \frac{1}{L}\frac{1}{L}\sum_{l}\left(y^{ll}\right)^2 - \left(\bar{y}\right) \qquad (2.15)$$

where L is the number of networks in the committee and the exponent l refers to the model used to give the corresponding prediction y^l. During training, it is usual to compare the performances of increasingly large committees on the testing set of data. Usually, the error is minimised by using more than one model in the committee. The selected models are then retrained on the entire database. Modelling uncertainties are often given for $\pm 1\sigma$ and are presented as error bars.
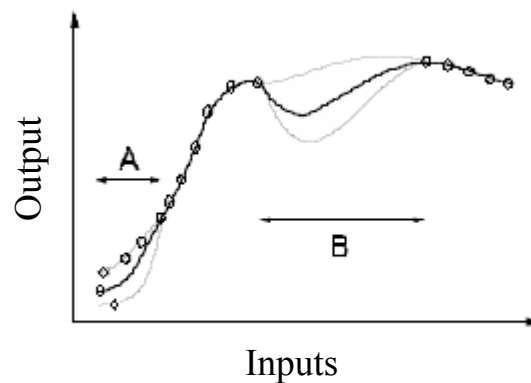
Figure 2.14: Schematic illustration of the uncertainty in defining a fitting function in regions where data are sparse (B) or where there is scatter (A). The thinner lines represent error bounds due to uncertainties in determining the weights [54].

2.8.5 Significance

A neural network based on a Bayesian framework can estimate the significance of individual input parameters influencing the outputs. A high value of significance implies that the input parameter concerned explains a relatively large amount of the variation in output and it is not an indication of the sensitivity.

From the software, there is a function of the values of the regularisation constants for the weights associated with an input, σ_w is a weight variance:

$$\sigma_w^2 = \frac{1}{\in} \tag{2.16}$$

where α is a control parameter which determines the complexity of the model. The weights of an input with a large value of α tend to zero, so such an input is not significant in the regression [49, 51]. This measure is similar to a partial correlation coefficient in that it represents the amount of variation in the output that can be attributed by any particular input.

To determine the sensitivity of the model to an individual input parameters, requires predictions must be made varying one parameter only whilst keeping all the others constant.

The "testing" of various physical models – input parameters based on those models can be included in the training data, and those parameters which are not useful in explaining the output will have much lower significance than those which are useful, figure 2.15.
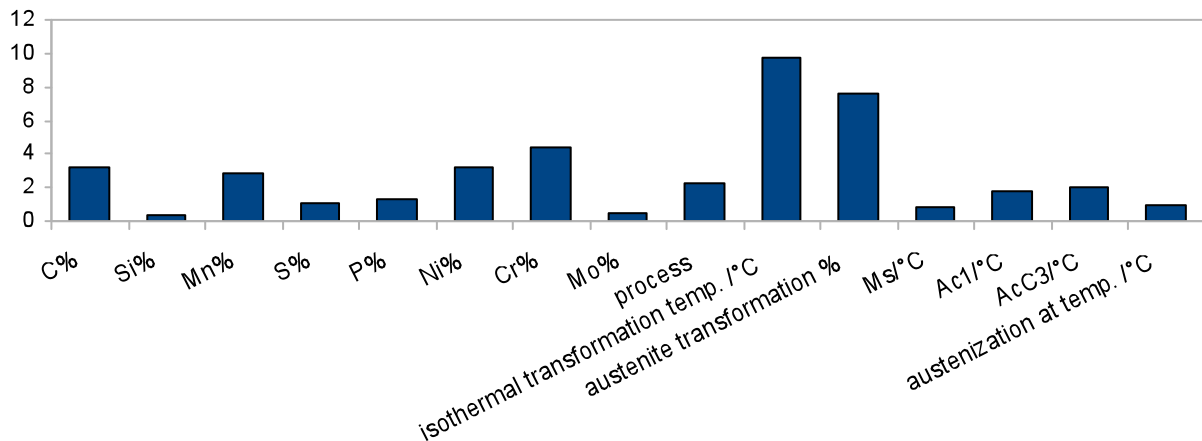
Figure 2.15: Example of a selected set of significance σ_w values from a committee. In this case the committee has 9 members.

2.8.6 Procedure to create an optimised model from neural network

To build a model with a neural network structure as described above, it is necessary to note a few points that should be followed to obtain a good model.

1- A data set should be collected first, with the principle that the input variables have relevant influence on the output. Anything missing in the input variables means that there is additional noise in the model.

2- An over ambitions set of many lead to an incompatibly small data set since not all publications report the full set of variables.

3- There are two useful terminologies that should be known; one is called noise and the other uncertainty. Noise means vibrating in the results when the experiment is repeated number of times because of uncontrolled parameters [56, 57]. The second terminology is representing the extent to which the same data may reasonably be represented by a variety of different mathematical formulations without exorbitantly compromising the fit in the region where experiments exist [56, 57]. Large modelling

uncertainty occurs when a wide range of different functions behaviour away from the data vary markedly.

4- Some functions can be included with the input variables as additional inputs, for example log (time) is used by some researchers [55]. The function should have meaning to the output if it is not effectively ignored by the network through association with near- zero weights.

The model needs to be assessed after getting the final committee. Comparison between the error standard deviation (root mean square residual, RMS) and the average size of the error bar gives a good indication of the performance of the model.

The root mean square residual R_{test} and the average size of error bars E_{bar} were calculated as follows [55]:

$$R_{test} = \sqrt{\frac{1}{N}\sum_{i=1}^{N}(T_i - Q_i)^2} \qquad (2.17)$$

$$E_{bar} = \frac{1}{N}\sum_{i=1}^{N}E_i \qquad (2.18)$$

where N represents the total number of predictions, T_i and O_i the experimental and calculated values respectively and E_i the error accompanying each prediction. The residual R_{test}, by quantifying the gap between the prediction and the actual value, is a good tool to evaluate the accuracy of the model for known data.

Chapter 3

Experimental Procedure

3.1   Introduction

This chapter introduces details of the experimental procedures that are followed in this study. The performed experiments are used to validate the mathematical models described in the latter chapters. Figure (3.1) is the general flow chart of the experimental procedures.
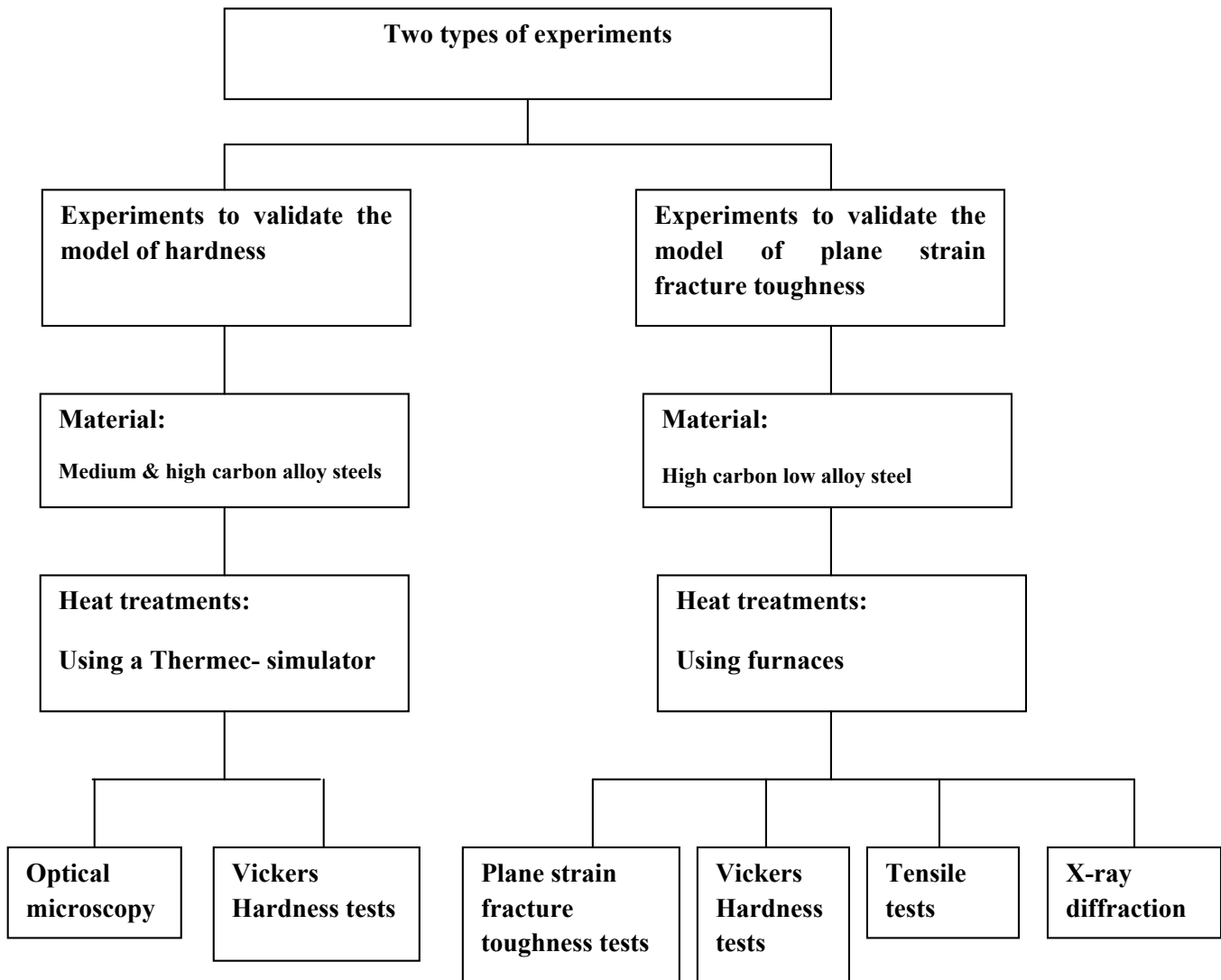
Figure 3.1: Flow chart illustrating the experimental procedures.

3.2 Experiments to validate the hardness model

3.2.1 Material

A variety of alloys are used in the experiments as shown in table 3.1. These steels are used in the experiments to validate the model for hardness, and to estimate the volume fractions of bainitic ferrite. Solid cylindrical specimens with dimensions of 3 mm diameter and 8 mm length are prepared for the heat treatment experiments. All of the alloys contain manganese, chromium and molybdenum with different concentration to achieve hardenability.

Table 3.1: Chemical composition (wt %) of steels.

Alloy	C	Si	Mn	Ni	Cr	Mo	Cu	Al	S
EE22	0.5436	0.0656	1.361	0.185	1.3176	0.0853	0.2143	0.0153	0
EE23	0.731	0.072	1.398	0.184	1.282	0.085	0.212	0.0127	0.021
EE24	0.519	0.221	0.746	0.614	0.553	0.164	0.291	0	0.0193
EE25	0.711	0. 222	0.743	0. 614	0.535	0.15	0.292	0.0126	0.02

3.2.2 Dilatometry Heat Treatments

The thermo-mechanical simulator "Thermecmastor Z" is used to perform heat treatments at different thermal cycles on small samples under accurate computer control. This simulator is manufactured by Fuji Electronic Industrial Co. Ltd. The temperature and diametrical dilatation of the specimen are measured and thus the progress of phase transformations within the material can be followed.

The sample inside the chamber of the "Thermecmastor Z" simulator is shown in figure. 3.2. Both of the upper and lower dies can be

raised using a hydraulic ram to hold the sample in its position. A platinum thermocouple is spot-welded to the specimen in a central position with the wires 1 mm apart.

The diametrical dilation of the sample is measured by a monitor using a laser beam, which moves and scans with the ram to ensure that the same location on the sample is measured throughout the experiment. The sample should be kept in the right location to ensure that the temperature and dilation measurements are for the same location. A closed chamber is under a vacuum of 10^{-2} Pa to prevent oxidation of the specimen. Helium was used in all the experiments as the cooling medium. Time, temperature and dilation are recorded and can be stored on a computer for analysis.
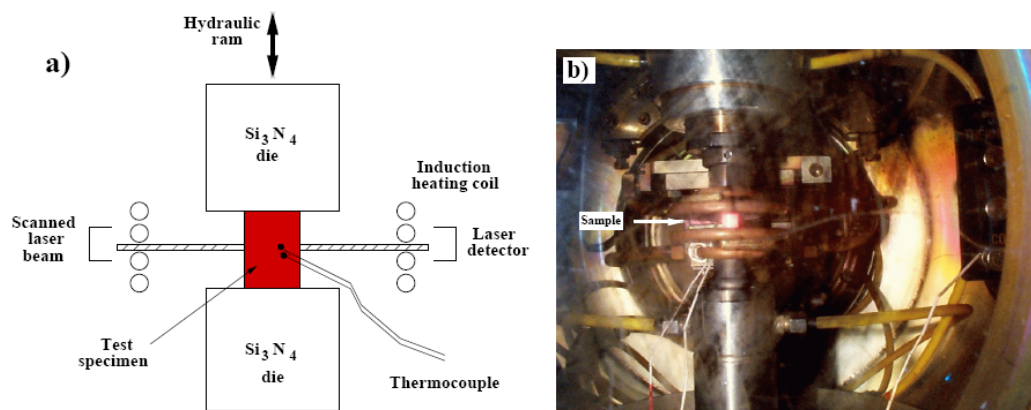
Figure 3.2: The sample inside the chamber within the thermecmastor Z thermomechanical simulator. (a) Drawing of the arrangement inside the chamber. (b) Photograph of the actual chamber [58].

3.2.2.1 Isothermal hardening experiments

Each of the dilatomertric samples is austenitised at 930°C for 30 min, followed by quenching to the isothermal temperature. The isothermal transformation temperatures used for each alloy are shown in table 3.2. Samples are kept at the constant temperature for different times according to the transformation kinetics. After isothermal heat treatment, they are cooled at a rate of 10 °C s^{-1}.

Table 3.2: The values of the isothermal transformation temperatures.

Alloy	Isothermal transformation temperatures (°C)
EE22	160, 260, 280, 300, 330
EE23	160
EE24	160, 280, 300, 350, 400
EE25	160, 250, 300, 320

3.2.2.2 Quenching experiments

Each sample is austenitised at 930 °C for 30 min, followed by cooling at a constant rate of 10 °C s^{-1} to room temperature. The heating and austenitisation treatments are carried out in a vacuum chamber, and the cooling is achieved using helium gas.

3.2.3 Hardness measurements

A Vickers hardness testing machine with 30 kg load is used to measure the macro-hardness of the steel samples after heat treatments. The load is applied for 15 seconds during testing. Five readings are taken over metallographic specimen area. The average of the readings is used to represent hardness.

3.2.4 Optical microscopy

Metallograpic analysis is carried out for the samples after heat treatment. A slice of 4 mm thickness is cut from each specimen and mounted in Bakelite. The surface is ground on four SiC papers ranging between 600-1200 grit and polished in two successive stages with 6 μm and   1 μm diamond paste. The samples were then cleaned and etched using 2% nital (2% concentrated nitric acid in methanol solution).

3.3 Experiments to validate the plane strain fracture toughness model

3.3.1 Material

A high carbon low alloy steel PP1 is used in the tests to validate the model of plane strain fracture toughness. The chemical composition of this alloy is shown in Table 3.3 [59]. The material is made in the form of 50 kg ingot by vacuum induction melting [59].

Table 3.3: Chemical composition of alloy PP1 wt %.

C	Si	Mn	P	S	Cr	Ni	V
0.97	1.43	1.59	0.0018	0.0012	0.26	0.04	0.09

3.3.2 Furnace heat treatments

The as received material is austenitised at 1000°C for one hour in a salt bath and then isothermally transformed at of 200°C using a salt pot for 9 days. The samples are then oil quenched to room temperature. All the samples were as blanks, and the final notch was machined after the heat treatment. Some of the samples were tempered at different temperatures and different times as listed in table 3.4.

Table 3.4: The values of tempering temperature and tempering time on the alloy PP1.

Tempering Temperature °C	Tempering time
300	6 hours and 1 month
400	(50,100,150,200,250,300) minutes and (2, 6 and 8) hours
450	6 hours
500	6 hours
600	6 hours

3.3.3 X-ray diffraction analysis

X-ray diffraction was used to determine the volume fraction of retained austenite V_{rr} using a *Cu K$_\alpha$* radiation at 40 kV and 40 mA. X-ray scanning was done for an 2θ=30-150°. The profile was analyzed for γ and α phases. The volume fraction was determined using the Rietveld analysis [60, 61], where the whole diffraction pattern is fitted at once was also applied to the data using Philips Highscore-plus software.

3.3.4 Plane strain fracture toughness tests

The fracture toughness test was conducted according to ASTM E 399-90 standard [43, 62] in order to obtain the plane strain fracture toughness K_{Ic} of the material. Compact tension specimens of the shape and dimensions shown in figure 3.3 were machined from the blanks. One sample was used for each tempering temperature, and the test was conducted in laboratory air at ambient temperature.
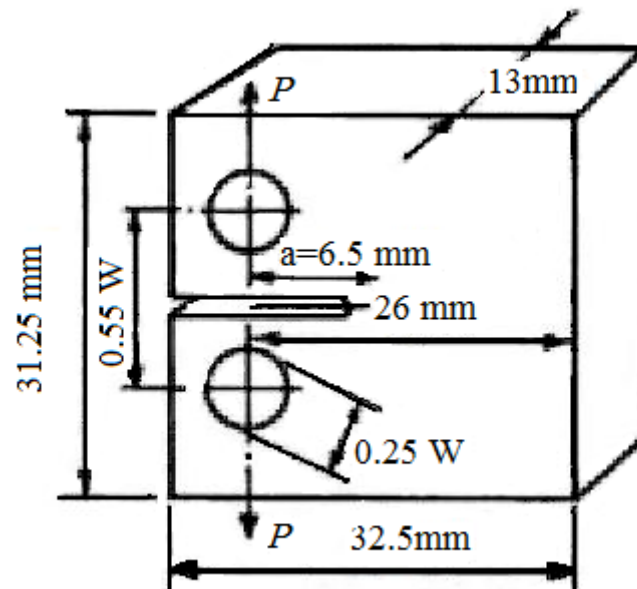
Figure 3.3: The dimensions of the compact tension samples.

The samples were tested on two different machines, the first machine was Mayes 100 kN Servo Hydraulic Machine, shown in figure 3.4, to fatigue pre-crack the sample using a sine wave loading with a frequency of (50 Hz). A step-down loading method was used during fatigue pre-cracking. After the pre-crack has reached the required length, the sample was removed and prepared for the fracture toughness test.

The second machine was an LCF tester with a maximum load capacity of (100 kN), figure 3.5. The sample carve was loaded with a very slow loading rate of 1 mm/min. The load-displacement was digitally recorded by a computer and the Bluehill®2 Software was used for data output.

Figure 3.4: Mayes 100 kN servo hydraulic axial fatigue testing machine [63].

Figure 3.5: LCF testing machine with a maximum load of 100 kN plane strain fracture toughness test [64].

3.3.5 Tensile tests

Enough material was not available to make specimens according to the ASTM standard. The specimens were machined to the shape and dimensions shown in figur 3.6. The samples were tested on a Hounsfield Low Load Electric Screw machine with maximum load of 5 kN as shown in figure 3.7.
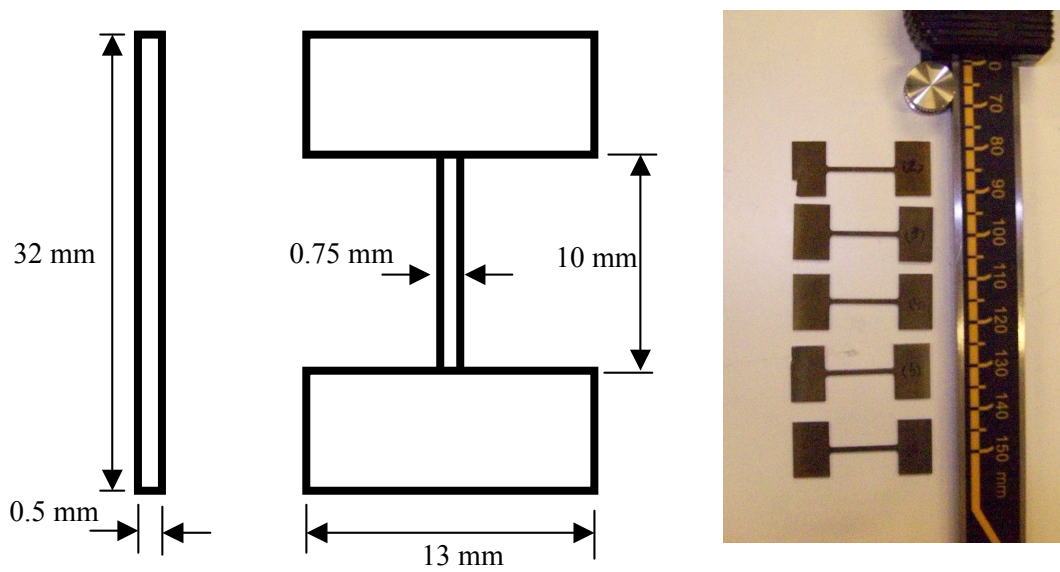
Figure 3.6: (a) Shape and dimensions of tensile specimen. (b) Photograph of the specimens used for tensile test.

Figure 3.7: Hounsfield Low Load Electric Screw Machine, maximum load 5 kN [65].

Chapter 4

Hardness Model

4.1 Introduction

Materials science and metallurgy have been developed over the years but there are phenomena which are too complex to fully understand because of their multivariate nature. The hardness of steels is affected by many variables and this is the reason why a general method for the prediction of final hardness is lacking. The hardness of steels depends on the microstructure which is determined by the chemical composition and heat treatment. There are no formal models that satisfactorily capture the relations between these variables. The neural network technique described in chapter two is of great use in this context.

Hardness is the simplest way of determining the resistance of metal to plastic deformation; it is easily measured and widely reported. Hardness is used as a quality control parameter to ensure that the process and materials used behave in a reproducible manner [4, 58].

Artificial neural networks have been used for the prediction of Vickers hardness for austempered ductile cast iron (ADI) using a Bayesian framework [4]. Another prediction system for a forging steel has been developed by adopting finite element method (FEM) with a neural network for modelling the hardness distribution in steel after forging and cooling [66].

In this work, neural networks are used to model the Vickers hardness as a function of chemical composition, transformation temperature, including isothermal transformation or isothermal transformation and direct quenching, for a wide range of steels. The design of the model is described, and to test its validity, predictions are compared with experimental values and expectations.

4.2 Vickers Hardness

The indentation test is used to measure the hardness in steels, both yielding and work hardening characteristics are important in determining the hardness. Yielding and work hardening properties are dependent on the chemical composition and heat treatment.

The production process can be optimised, by controlling the microstructure, which is correlated to hardness. For example the hardness of super-bainite is greater than ordinary bainite with the same carbon concentration. For mixed microstructures, the hardness depends on the transformation temperature and composition [35]. As the transformation temperature changes, the microstructures also change. Depending on the amounts of bainite and carbon-rich austenite.

4.3 Hardness database

Most steels in commercial use are heat treated either by low or high cooling rate from the austenitizing temperature or by quenching to martensite, and subsequently tempering to obtain optimum properties. In contrast, isothermal heat treatments in the bainite transformation range have not found wide applications, partly due to the uncertainties associated with optimizing mechanical properties by such treatments, but also because of the difficulties involved in controlling the microstructures involved [42]. Therefore in this work, three separate committee models

were produced to enable comparisons between the different databases, it discuss below.

It is likely that a better model will result when the data are uniformly distributed but such data are difficult to extract from the publish literature.

The hardness is a function of chemical composition and heat treatment. Therefore, in this investigation, the choice of the inputs is as follows:

$$HV = f(C_i, V_b, T_a, T_t, T_{temp}, t_{temp}) \qquad (4.1)$$

where C_i represent the chemical composition (carbon, manganese, silicon, chromium, nickel and molybdenum). Phosphorus and sulphur are excluded because they are present in very small concentrations and hence unlikely to influence hardness. Furthermore, they did not show large variation with dataset. T_t transformation temperature °C, V_b volume percent of bainite, was used instead of the time needs for the transformation, T_a austenitisation temperature °C, T_{temp} tempering temperature°C and t_{temp} tempering time. Tempering temperature and time have been used only to build the third data set committee. The lower and upper critical temperatures, A_{c1} and A_{c3} respectively and martensite start temperature M_s were not included in the input variables, because these are related to chemical composition [10, 67-69], and when they were removed, there was no significant difference in the output.

The data set is made of experimental data collected from a published atlas of isothermal transformation diagrams [70]. Data concerning super-bainite were also included [21, 30, 31, 34].

Three sets of data are used for modelling in this work, as described in tables 4.1 to 4.3, which give the maximum, minimum, average and standard deviation for each input parameter. Figure 4.1 presents the distribution in parameters in the second data set committee in model hardness_2. Some parameters are homogeneously distributed, such as carbon and volume fraction of bainite, while others, such as silicon and molybdenum, are clustered as shown in figure 4.1. This is recognised by Bayesian framework [49], which associates large modelling uncertainties with regions where the data are sparse or noisy.

Table 4.1: The variables in the first data set consist of 458 experiments. The transformation temperature is the isothermal transformation temperature only.

Parameter	Minimum	Maximum	Average	Standard Deviation
C / wt%	0.11	1.08	0.56	0.33
Si / wt%	0.09	1.59	0.32	0.33
Mn / wt%	0.30	1.98	0.74	0.42
Ni / wt%	0.00	4.33	2.01	1.46
Cr / wt%	0.10	1.65	0.89	0.13
Mo / wt%	0.01	0.74	0.16	0.13
Transformation temperature / °C	125	760	489.17	145.5
Volume percent of bainite	0	100	74.50	36.3
Austenitisation temperature / °C	770	1020	412.8	165.3
Hardness / HV	158	826	412.8	165.3

Table 4.2: The variables in the second data set consist of 511 experiments. The transformation temperature includes the isothermal transformation temperature and direct quenched temperature.

Parameter	Minimum	Maximum	Average	Standard Deviation
C / wt%	0.11	1.08	0.56	0.33
Si / wt%	0.09	1.59	0.31	0.32
Mn / wt%	0.30	1.9	0.73	0.41
Ni / wt%	0.00	4.33	1.94	1.44
Cr / wt%	0.10	1.65	0.87	0.40
Mo / wt%	0.01	0.74	0.16	0.13
Transformation temperature / °C	30	760	461.5	180.2
Volume percent of bainite	0	100	70.4	39.4
Austenitisation temperature / °C	455	1020	852.7	71.2
Hardness / HV	158	940	415.1	166.8

Table 4.3: The variables in the third data set consist of 613 experiments. The transformation temperature includes the isothermal transformation temperature and direct quenched temperature, with other two input parameters tempering temperature and time.

Parameter	Minimum	Maximum	Average	Standard Deviation
C / wt%	0.11	1.08	0.49	0.34
Si / wt%	0.09	1.59	0.30	0.30
Mn / wt%	0.30	1.9	0.63	0.39
Ni / wt%	0.00	4.33	2.01	1.46
Cr / wt%	0.10	10.6	1.77	2.72
Mo / wt%	0.01	1.05	0.25	0.27
Transformation temperature / °C	30	760	389.00	230
Volume percent of bainite	0	100	58.57	44.55
Austenitisation temperature / °C	455	1020	877.47	85
Tempering temperature / °C	30	750	129.11	223
Tempering time / h	0.50	579	15.77	72
Hardness / HV	158	940	399.01	148.10
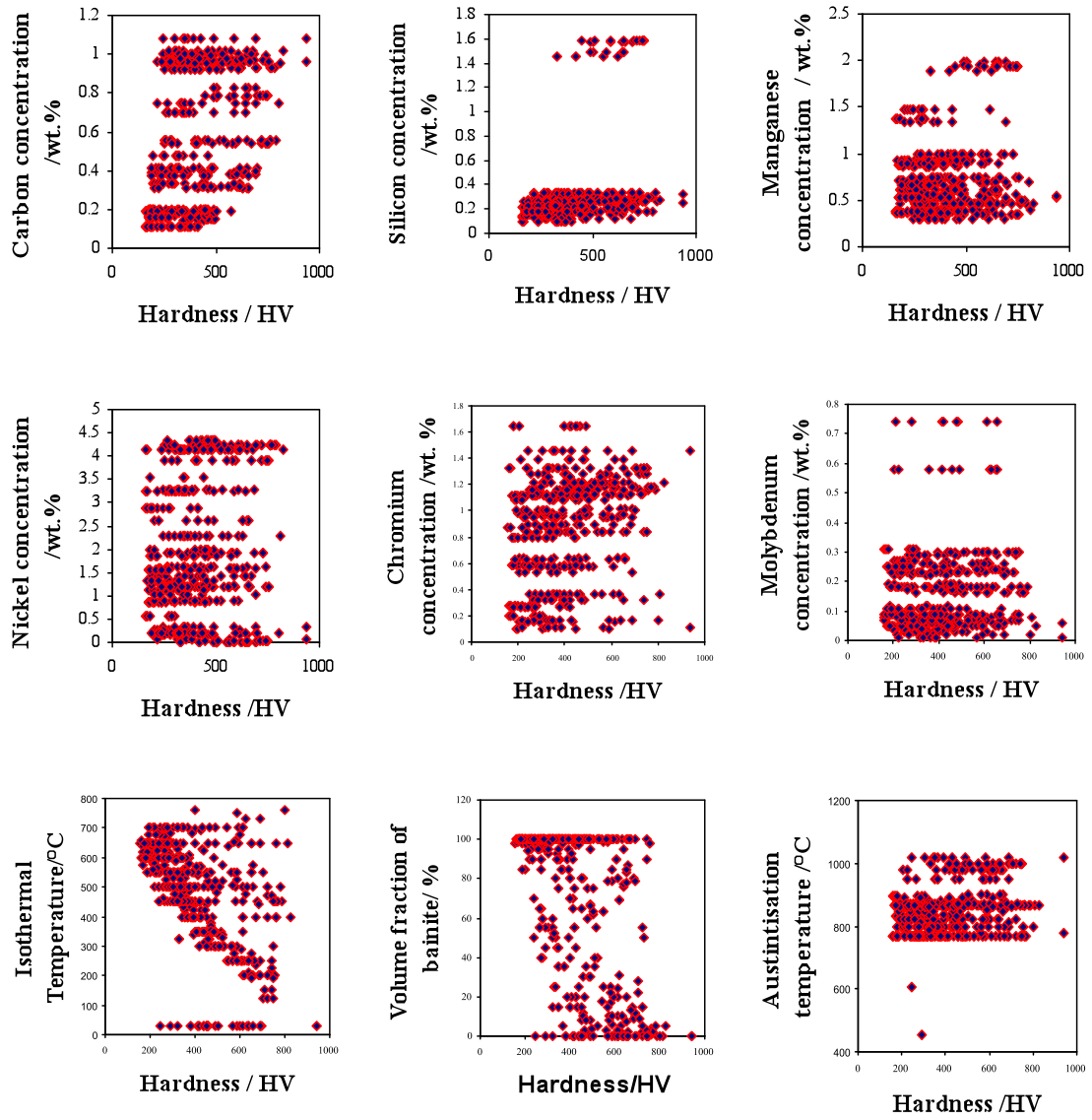
Figure 4.1: The distribution of inputs against hardness in the second dataset.

4.4 Model training

The data were randomized as described in chapter two and then divided equally into two, the test and training sets respectively. The training set is used to create a large number of neural networks models. The test data set is used to see how the trained models behave on unseen data. One hundred sub-models are trained using the training dataset. Each model has different number of hidden units and random seeds used to initiate the values of the weights. Figure 4.2 gives the training and test results of 98 models for committee model hardness_2. The perceived level of noise σ_v decreases as the number of hidden units increases, which means that a more complex function will be achieved and the model has lower σ_v, figure 4.2a. The log predictive error (LPE) reaches a maximum at five hidden units, figure 4.2c. The number of hidden units is set by examining the performance of the model on unseen test data, and the test error reaches a minimum at three hidden units, figure 4.2b. The neural network program ranks the models according to the test error in order to find the optimum committee model. One containing two of the best models is found to be the optimum with the smallest over all test error, as shown in figure 4.2d. The selected committee then is retrained on the entire data set without changing the complexity of its member models. Figure 4.3 shows a plot of measured versus predicted output using the committee model hardness_2 on the whole dataset. There are a few points that lie outside the 45° line and small error bars which represent the combined effect of modelling uncertainty and the perceived level of noise.
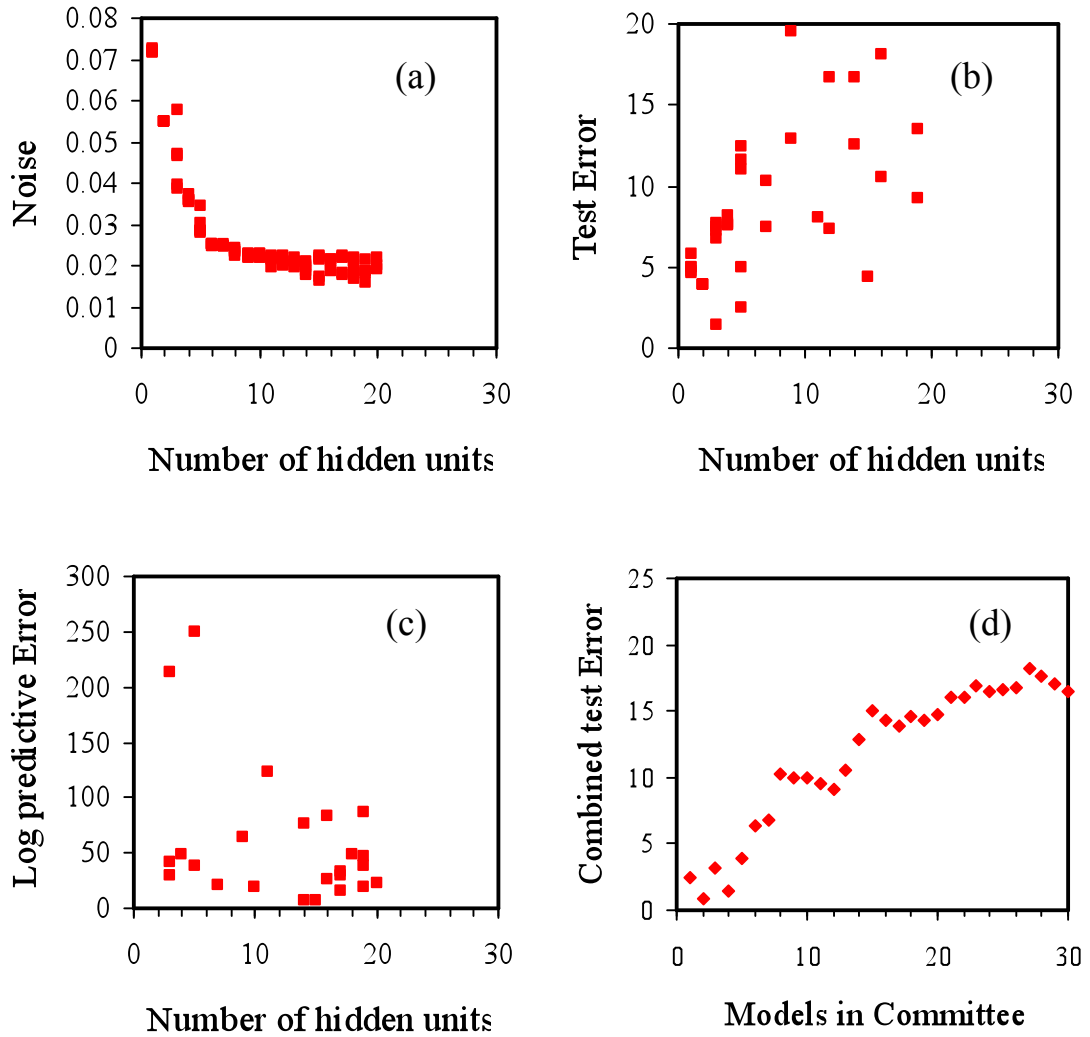
Figure 4.2: The training and testing results of the committee model hardness_2. (a) Perceived level of noise against hidden units (b) Test error against hidden units (c) Log predictive error against hidden units (d) Test error against number of models in the committee.
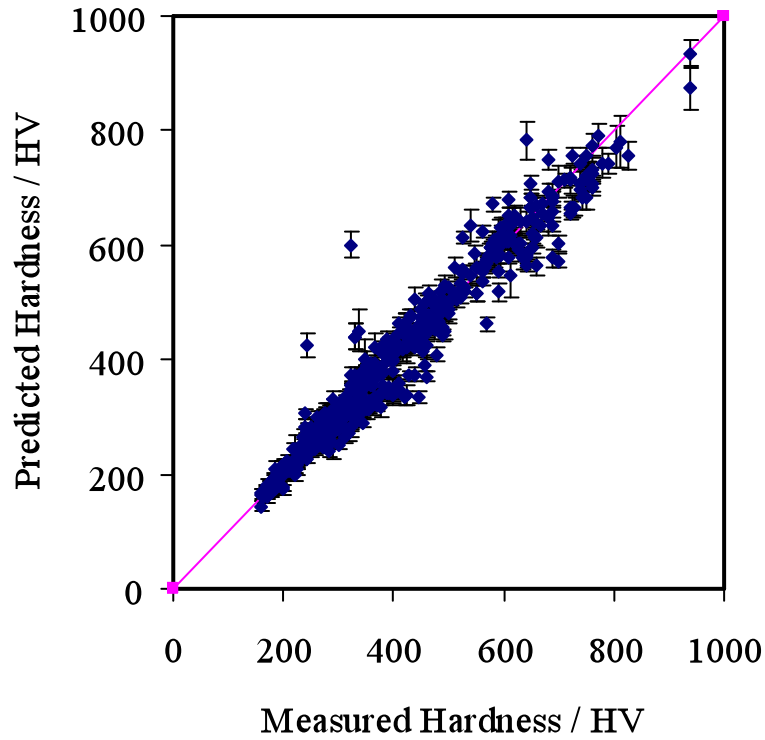
Figure 4.3: Predicted hardness against measured hardness of the committee model hardness_2.

     All the committee models from one to three are trained and tested in the same manner, and their training and test results are shown in table 4.4. This table shows the (LPE), test error, number of hidden units and test error of the best model of each committee. The hardness_3 model shows relatively high test error.

Table 4.4: Training and test results of the committee models.

Hardness model name	Data	LPE	Test error	Number of hidden units	Number of models in committee	Test error in committee
Hardness_1	The first data 458 experiments	305	0.53	3	8	0.47
Hardness_2	The second data 510 experiments	250	2.4	5	2	0.87
Hardness_3	The third data 613 experiments	165	3.2	2	2	2

Figure 4.4 indicates the significances, σ_w, of the input variables, as perceived by the committee model hardness_2. The significance indicates the level of contribution to the output, rather like a partial correlation coefficient in linear regression analysis. Transformation temperatures, carbon content, volume fraction of bainite and silicon have relatively large contributions to hardness.
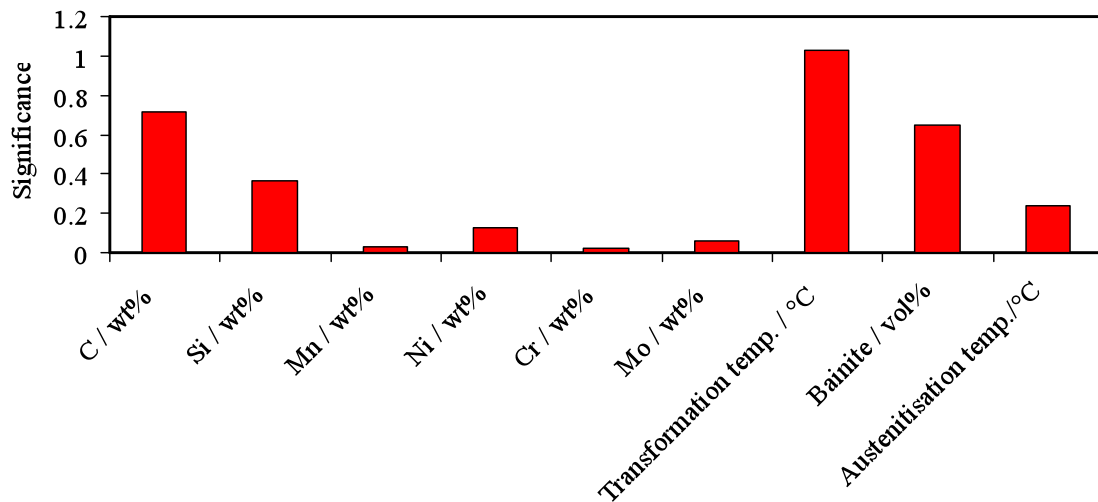
Figure 4.4: Significance of each variable of committee model hardness_2.Transformation temperature °C, V_b and Si give the largest contributions to hardness, in descending order.

4.5 Application of model

The optimised committee consisting of two sub-models, hardness_2, is used to study the effects of individual variables to check whether the results are compatible with known metallurgical principles and other published trends not incorporated in the models. Predictions were made for the steel with the composition (0.98C- 1.46Si- 1.89Mn- 1.26Cr- 0.26Mo wt%) [21, 71], by varying a particular input while the others are fixed. The isothermal transformation temperature is set at 200°C; the bainite volume percent is sixty nine with austenitisation at 1000°C.

4.5.1 Effect of alloying elements on hardness

The influence of alloying elements was studied with a particular emphasis on the carbon content and silicon. All error bars represent the combined effect of the uncertainty and noise in the committee model. C, Si, Mn, Ni, Cr, and Mo contribute to the outputs as shown in figure. 4.5 to 4.10. Figure 4.5 shows that the hardness increases as the carbon concentration of steels varies from 0.1 to 0.6 wt% and then decreases as the carbon content increases. The reduction at large carbon concentration is expected due to the greater retention of relatively soft austenite.

To check the general trend of this effect of carbon concentration on hardness, the law of mixtures [42] has been used to predict the hardness:

$$HV v_b H_b + v_\gamma H_\gamma + v_{\alpha'} H_{\alpha'} \qquad (4.1)$$

where V_b, v_γ and $v_{\alpha'}$ are the volume fractions of bainite, retained austenite and martensite respectively, H_b is the hardness of bainitic ferrite (480 HV), H_γ the hardness of retained austenite (taken to be 240 HV even though it might change slightly with carbon content [42]) and $H_{\alpha'}$ that of martensite, calculated as follows [42]:

$$H_{\alpha'} = H_o + Q(\bar{x} - s) \qquad (4.2)$$

where Q the dependence of martensite hardness on carbon content, found to be 1020 HV/ wt% of carbon in solid solution [42], s is the amount of carbon trapped in the bainitic ferrite [42], either in solid solution (s=0.03 wt%) or in the form of carbides (s=0.27 wt%), H_o the martensite hardness at a carbon content of $\bar{x}$ =0.43 which is 795 HV [42]. A program mucg-73 has been used to calculate M_s in order to estimate the volume fraction of retained austenite as a function of martensite-start temperature [72].

$$v_B = \frac{M Fe 2}{2} \exp[1.1010()]^{22} \qquad sq \tag{4.3}$$

where T_q represents the lowest temperature reached during quenching. Figure 4.6 shows the two predictions and both show similar trends.

Figure 4.7 shows that the hardness decreases as silicon content increases with low error bars. The silicon makes the carbon constrict the precipitation of carbides during the bainite transformation [73]. It is interesting that transmission electron microscopy in the work by Zhang *et al.* [74] revealed that the bainite was free from carbides in spite of the fact that the silicon concentration of steel was less than 0.6 wt.%. Larger concentrations of silicon have been used in all of the steels developed to generate nanostructured bainite, in order to prevent the precipitation of cementite during the course of transformation. It may be possible to use lower concentrations and yet maintain a carbide-free phase mixture [75].
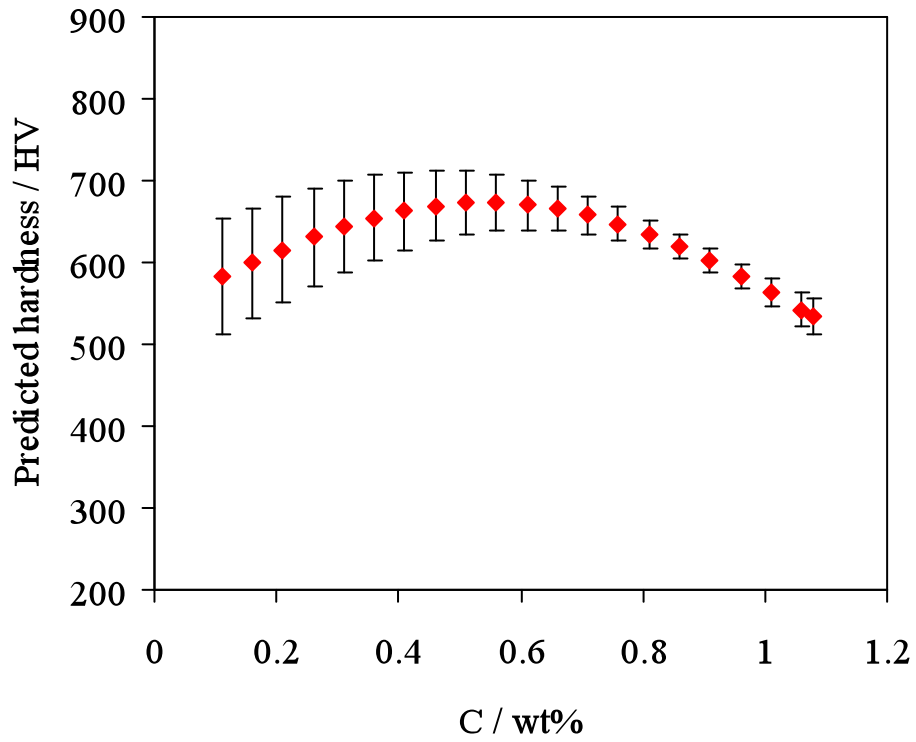
Figure 4.5: Predictions of hardness in HV against carbon content in wt%, using the committee model hardness_2 and the inputs listed in table 4.2.
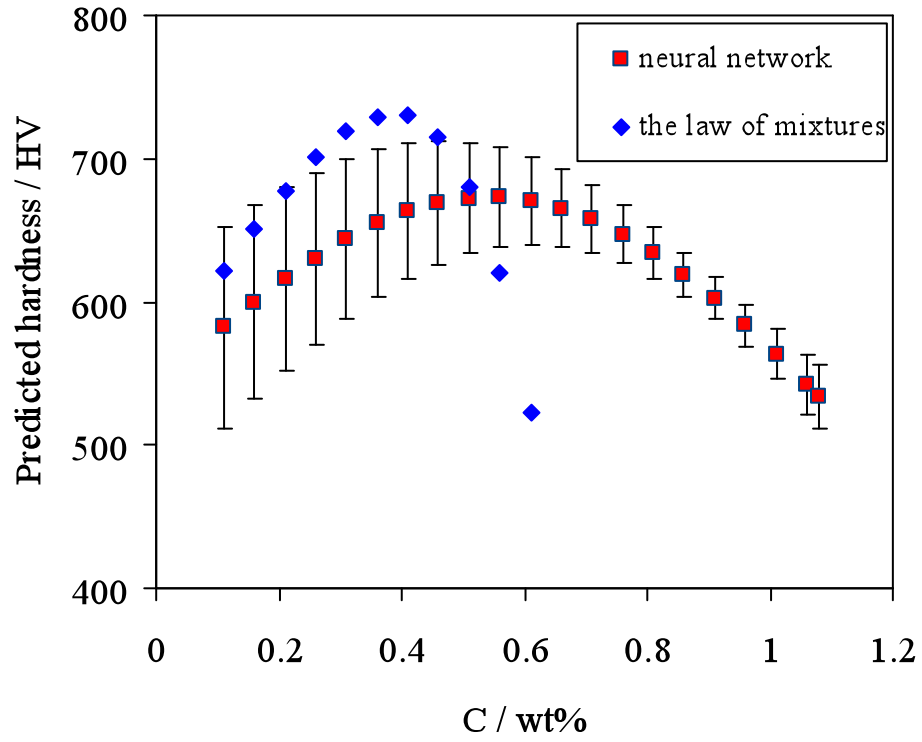
Figure 4.6: Hardness / HV as a function of carbon content wt% for both neural network and the law of mixtures calculations.
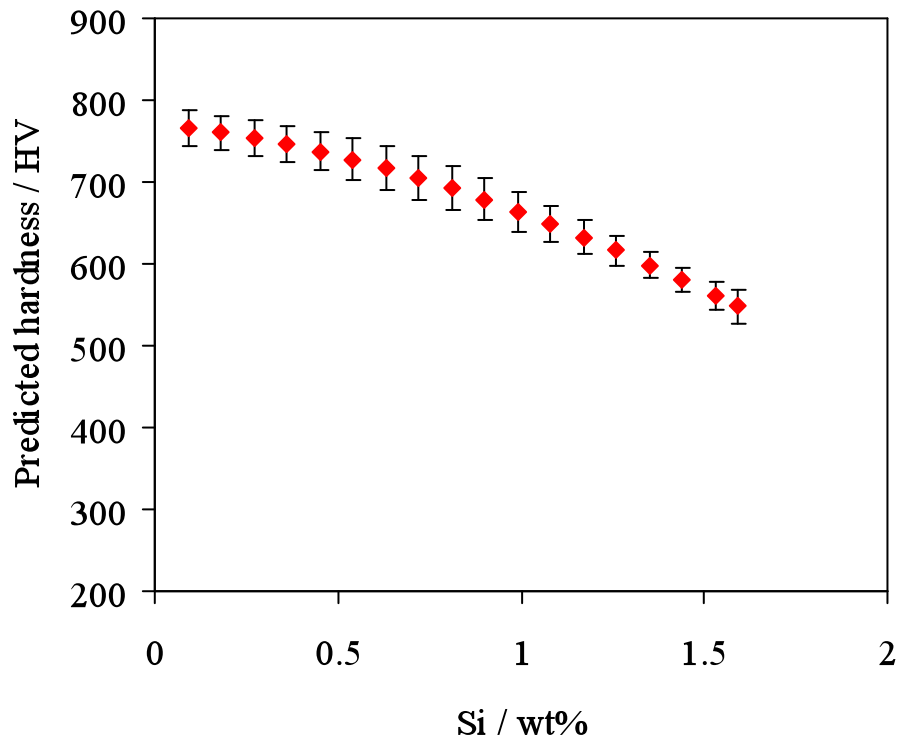
Figure 4.7: Predictions of hardness in HV against silicon content in wt%, using the committee model hardness_2 and the input listed in table 4.2.

Figure 4.8 shows that for a fixed transformation temperature manganese slightly increases the hardness. This is because it retards transformation by increasing the hardenability. The fraction of martensite in the microstructure therefore increases causing a corresponding increase in hardness. There is of course, a small substitutional hardness effect as well. Figurs 4.9-4.11 show the effect of nickel, chromium and

molybdenum on hardness respectively. There appear to be only minor effects. That is in agreement with the significance of input variables that was shown in figure 4.4, *i.e* the model perceives low significance for Ni, Cr and Mo.
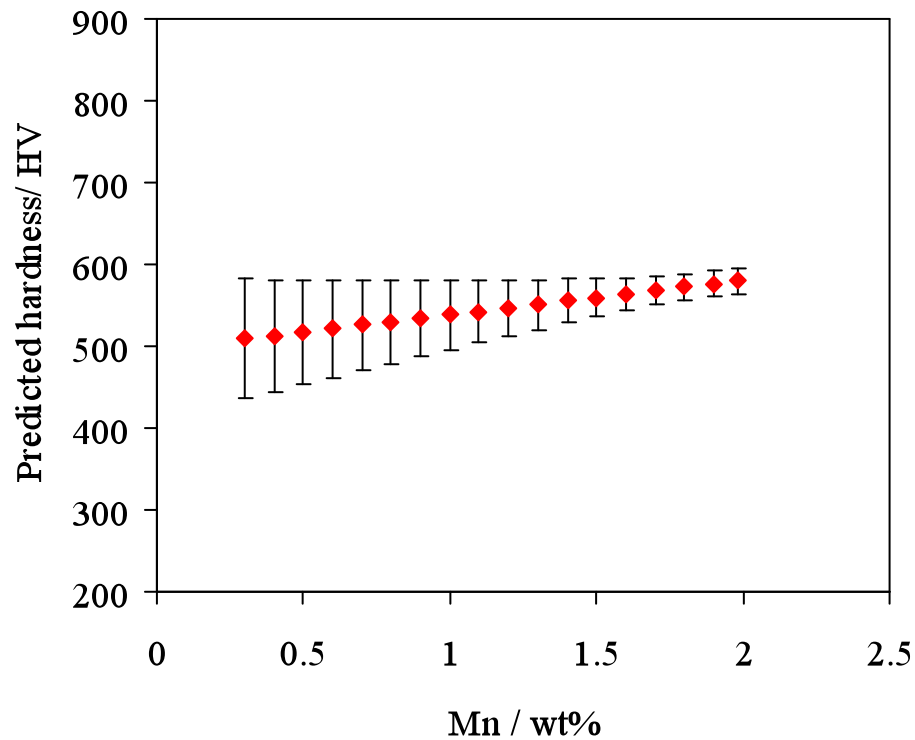
Figure 4.8: Predictions of hardness in HV against manganese content in wt%, using the committee model hardness_2 and the input listed in table 4.2.
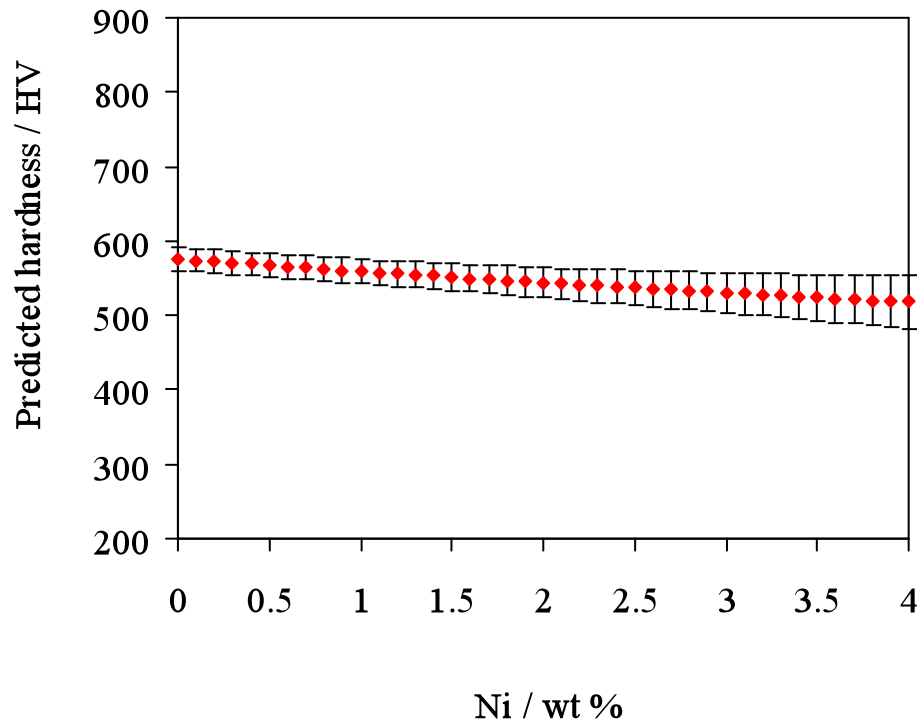
Figure 4.9: Predictions of hardness in HV against nickel content in wt%, using the committee model hardness_2 and the input listed in table 4.2.
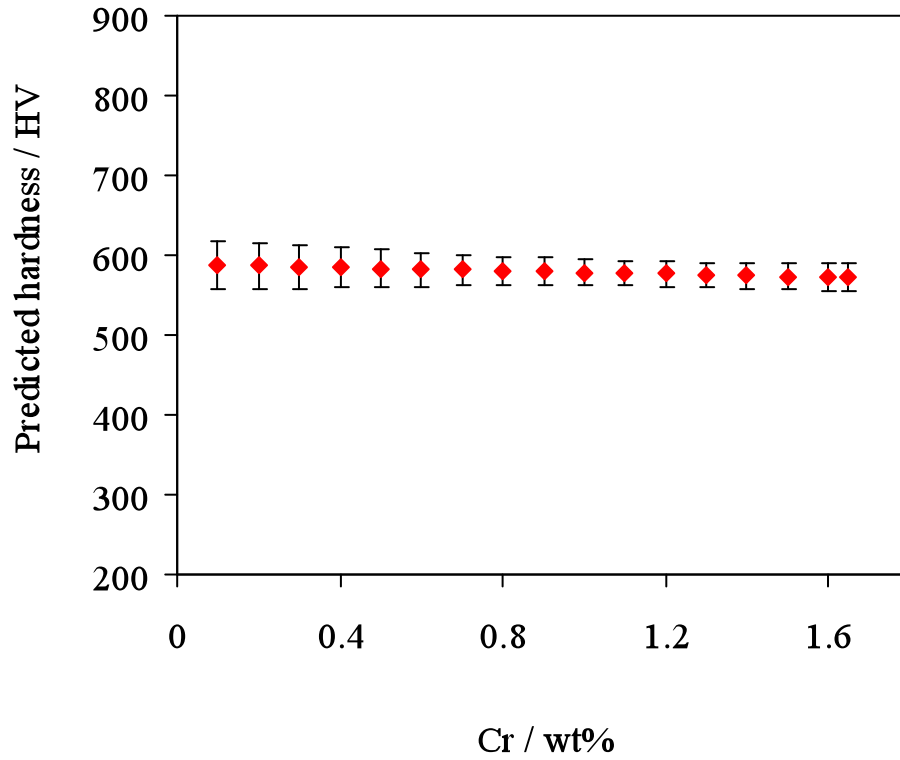
Figure 4.10: Predictions of hardness in HV against chromium content in wt%, using the committee model hardness_2 and the input listed in table 4.2.
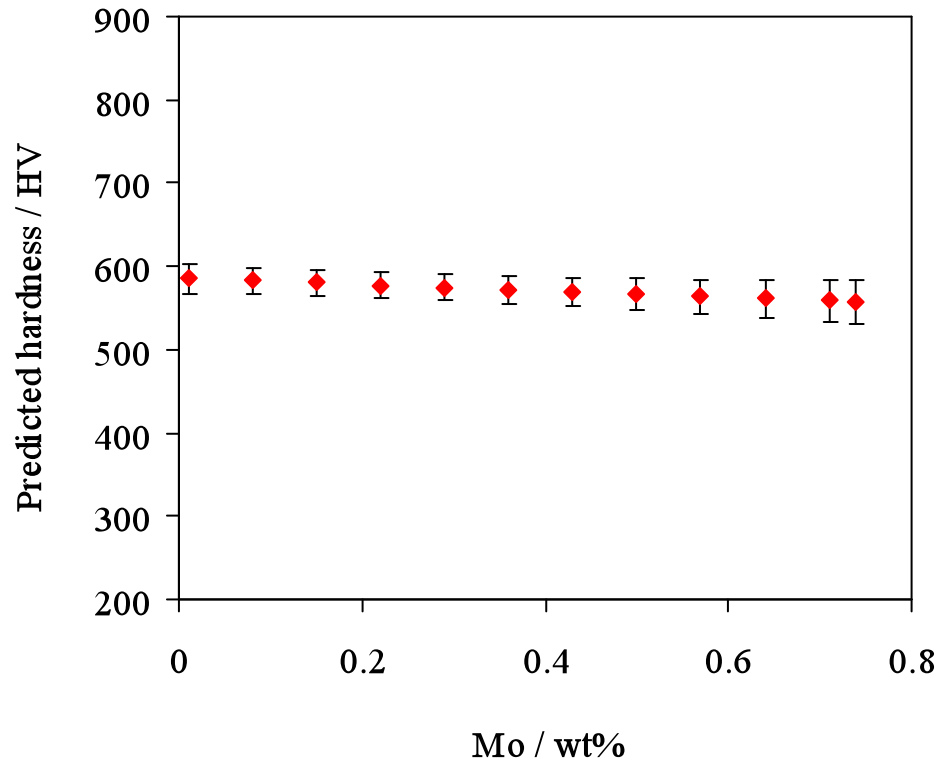
Figure 4.11: Predictions of hardness in HV against molybdenum content in wt%, using the committee model hardness_2 and the input listed in table 4.2.

4.5.1 Volume fraction of bainite and transformation temperature

The effect of the bainite the volume fraction and the transformation temperature on hardness were studied. Figure 4.12 shows that the hardness decreases as the transformation temperature increases;
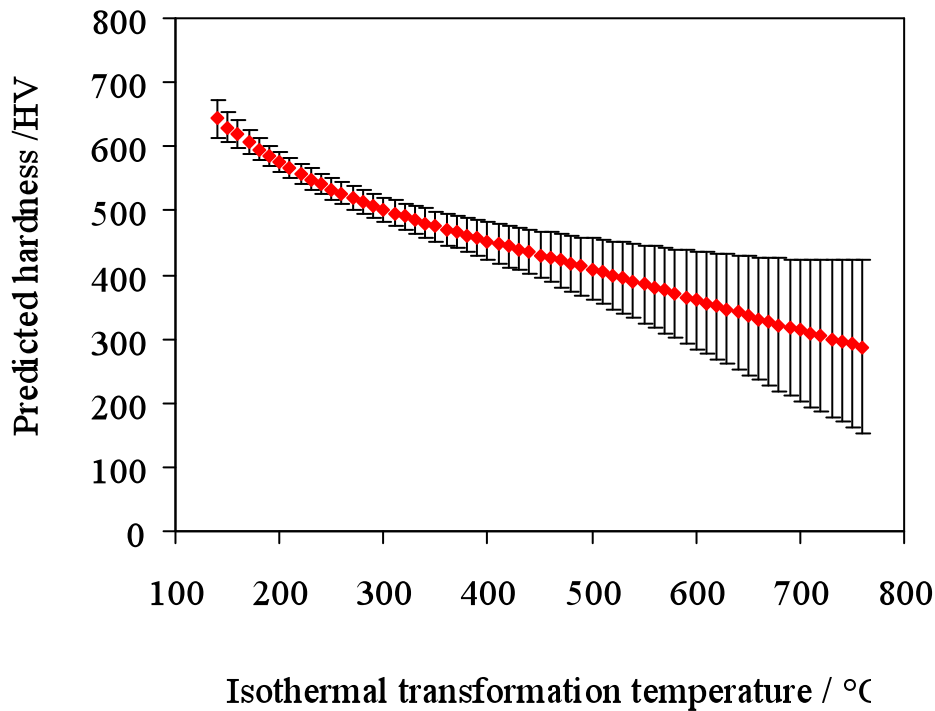
Figure 4.12: Predictions of hardness in HV against transformation temperature, using the committee model hardness_2 and the input listed in table 4.2.

Figure 4.13 shows that the hardness decreases as the volume percent of bainite increases from 0 to 50 and then increases as the volume percent become larger. This is because the hardness first decrease as bainite replace martensite, but as the fraction of fine-bainite increase so the hardness increase [21]. Than the increases mean for slip distance reduced as more fine-bainite forms.
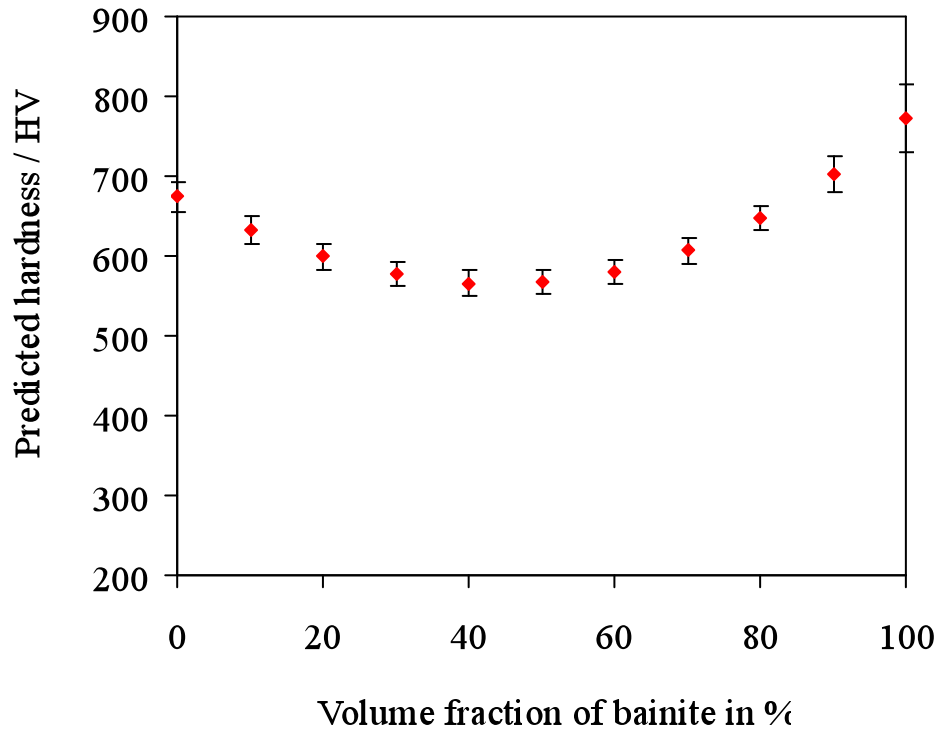
Figure 4.13: Predictions of hardness in HV against volume fraction of bainite in wt%, using the committee model hardness_2 and the input listed in table 4.2.

Figure 4.14 shows that the austenitisation temperature has almost no effect on hardness, the error bars are high between 700°C to 800°C, this is due to the fact that not enough input data were available in the range of these temperatures.
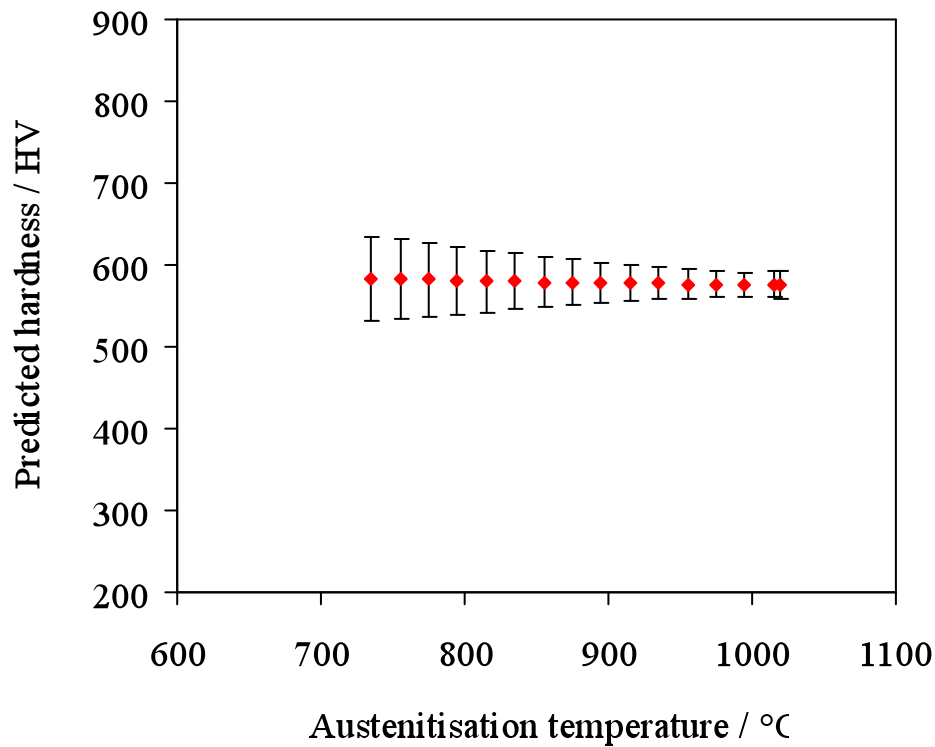
Figure 4.14: Predictions of hardness in HV against austenitisation temperature, using the committee model hardness_2 and the input listed in table 4.2.

Figure 4.15 shows the combined effect of transformation temperature and bainite volume fraction on hardness for the same alloy[2] used previously for the prediction of the effect of alloying elements on hardness. They show the non-linear relationships that are not captured by linear regression methods [42]. Neural network models can capture more complex interactions. As can be seen in this figure, the highest hardness (700 HV-800 HV) is with high volume percent of bainite (90-100) and low transformation temperature (200-240 °C). This may be due to the development of an extremely fine and hard bainite at low isothermal transformation temperature [35]. This super-bainite phase is the hardest

---

[2] (0.98C- 1.46Si- 1.89Mn-1.26Cr- 0.26Mo wt%)

ever been produced [75]. There are also two regions which have relatively high hardness (600 HV-700 HV), the first has low volume percent of bainite in the range (0-20) and the second has high volume percent of bainite in the range (70-100) and with relatively low transformation temperatures less than 285 °C. In the low bainite volume percent region, the rest of the microstructure because martensite which is also a hard phase. The relatively high hardness in the second region is again due to the development of a relatively fine and hard bainite at low isothermal transformation temperature. As the isothermal transformation temperature increases, the hardness drops.

Figure 4.16 shows the combined effect of carbon content and transformation temperature on hardness in steels. The transformation temperature has the most significant effect on hardness; super-bainite forms at the low isothermal transformation temperatures and hence contributes to the highest hardness.

Figure 4.17 shows the combined effect of transformation temperature and silicon concentration on hardness. The transformation temperature has the main effect on hardness that masks the effect of silicon. As the transformation temperature decreases from (600-200) °C, hardness increases from 200 HV-800 HV. This is mainly due to the refinement of the bainitic structure with decreasing transformation temperature.

Figure 4.18 shows the combined effect of bainite volume fraction and carbon concentration on hardness. All the hardness values in this figure are higher than 500 HV which indicates that hard phases are present (martensite and ∕or bainite). There are two regions which show the highest hardness (700-800) HV. The first region is at low bainite volume

fraction (V_b > 0.2) and at a range of carbon content of (0.33-0.91 wt%) which may be due to the formation of martensite. The second region is at a high bainite volume fraction (V_b > 0.8). There are also two regions where the hardness is the least (500-600) HV. The first is at low carbon content C > 0.15 wt% where the martensite and bainite becomes leaner in carbon and hence less hard. The second region is at high carbon content C < 0.88 wt% where the M_s temperature decreases and the isothermal transformation temperature of 200 °C, which is assumed constant in the construction of these contours, leads to coarser and less hard bainite.

Figure 4.19 shows the combined effect of bainite volume fraction and silicon content on hardness. All the hardness values are above 500 HV. The highest hardness (800-900) HV is at low bainite volume fraction and low silicon concentration of Si < 0.76 wt%. Here the volume fraction of martensite is the greatest. Content of Si greater than 1.28 wt% inhibit the precipitation of carbides during the transformation to bainite [73] and hence leads to the least hardness (500-600) HV.
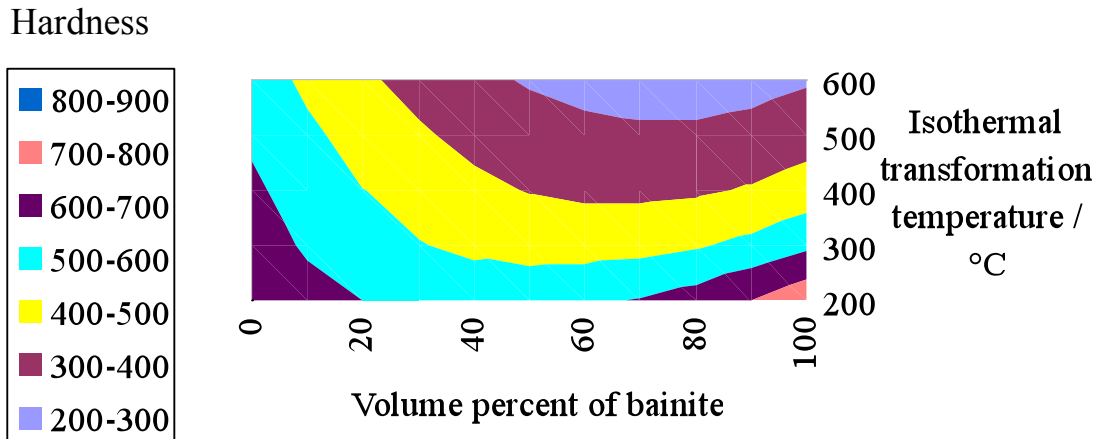
Hardness

Figure 4.15: Contours for predicted Vickers hardness against transformation temperature and volume percent of bainite for committee model hardness_2.
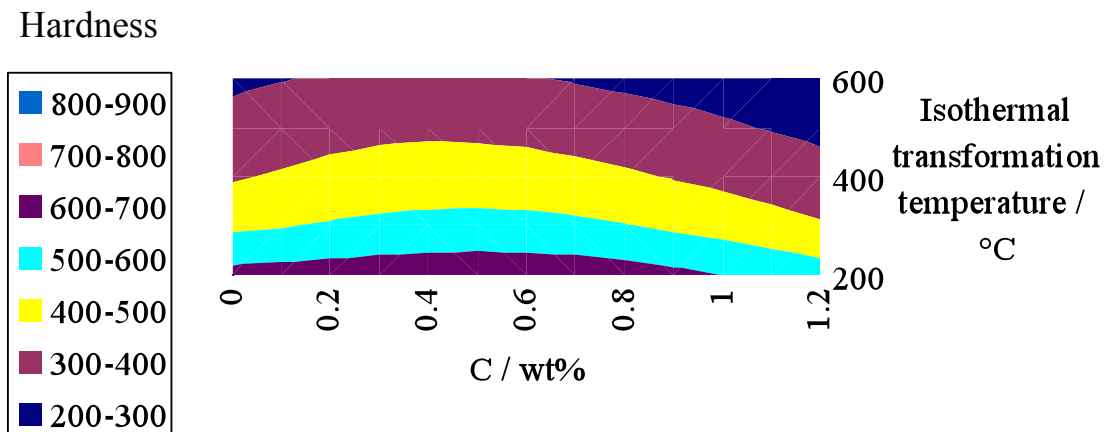
Hardness

Figure 4.16: Contours for predicted Vickers hardness against transformation temperature and carbon content for committee model hardness_2.
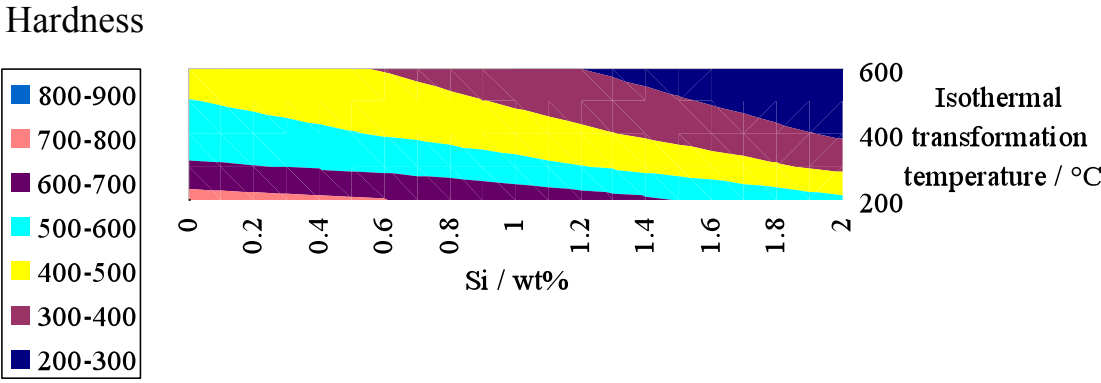
Figure 4.17: Contour for predicted Vickers hardness against transformation temperature and silicon content for committee model hardness_2.
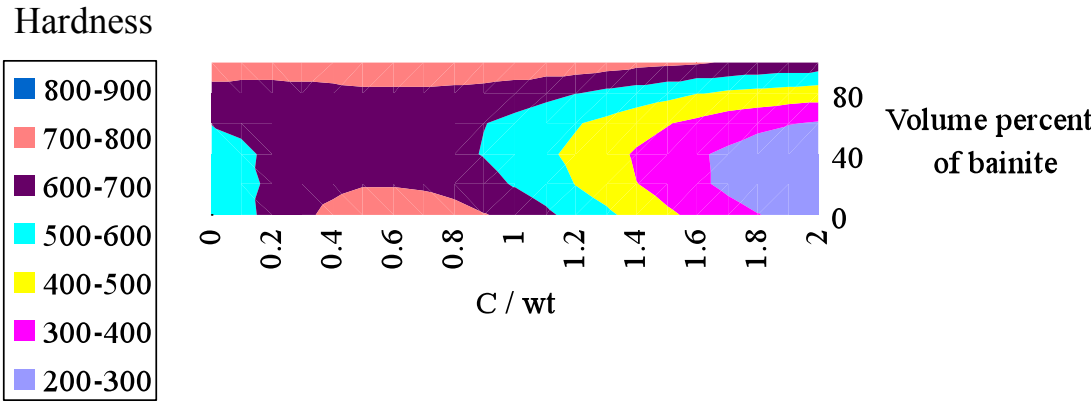
Figure 4.18: Contour for predicted Vickers hardness against volume fraction of bainite and carbon content for committee model hardness_2.
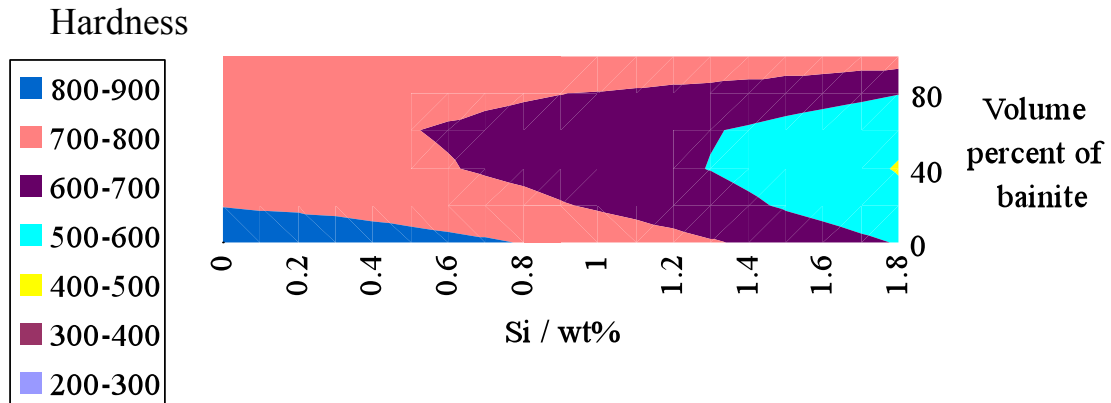
Hardness

Figure 4.19: Contour for predicted Vickers hardness against volume fraction of bainite and silicon content for committee model hardness_2.

4.6 Comparisons between models

Further data not used in creating the model were collected from published results [42, 71, 76-78] The data also included the steels which have been studied in this work (EE22, EE23, EE24, EE25 and PP1) and their chemical compositions are shown in table 3.1 and table 3.2. The chemical compositions for the unseen data are shown in table 4.5; some of these data are outside the range of the training data used in building the model. These were used to demonstrate the predictive abilities of neural network models and to verify their general applicability.

Figures 4.20 to 4.22 show plots of the measured values versus predicted values for hardness of the alloys according to the three committee models (hardness_1, hardness_2 and hardness_3). The neural

network model trained on the first data set shows large uncertainties and rough predictions for these alloys as shown in figure 4.20.

On the other hand, the neural network model trained on the second data set gave more acceptable results, figure 4.21. It confirms that the incorporation of direct quenching in the second data set can raise the predictive power of the model and reduce the uncertainties. In addition, the prediction results of the model which include isothermal and direct transformation temperature model (hardness_2) is more compatible with the experimental results than those of models that were trained on the data set with only isothermal transformation temperature (hardness_1), and the isothermal transformation temperature, direct quench and tempering data set (hardness_3), figure 4.22.

Table 4.6 shows the perceived error of the models, and the root mean squared error, to compare the performances of these three models. The committee of model hardness_2 has the least difference between the perceived error and the root mean squared error among the three models. From this test we can confirm that committee model hardness_2 is the best one among these three models for a data concern data both within and out of the training range.

Table 4.5: Compositions for the steels used to test predictive capability.

References	C / Wt%	Si / Wt%	Mn / Wt%	Ni / Wt%	Cr / Wt%	Mo / Wt%
[42, 76]	0.43	2.02	3	0.01	0.01	0
[76]	0.22	2.03	3	0.01	0.01	0.01
[76]	0.39	2.05	0	4.08	0	0
[77]	0.32	1.45	1.97	0.02	1.26	0.26
[77]	0.31	1.51	0.01	3.52	1.44	0.25
[77]	0.3	1.51	0.01	3.53	1.42	0.25
[71]	0.98	1.46	1.89	0	1.26	0.26
[17]	1	1.5	1.9	0	1.3	0.25
[78]	0.78	1.6	2.02	0	1.01	0.25

Table 4.4: The prediction ability of three committee models against the unseen data within and out of the range of training data.

Model	Root mean squared error	Perceived error
Hardness_1	95.1	58.88
Hardness_2	53.5	29.76
Hardness_3	129.5	24.56
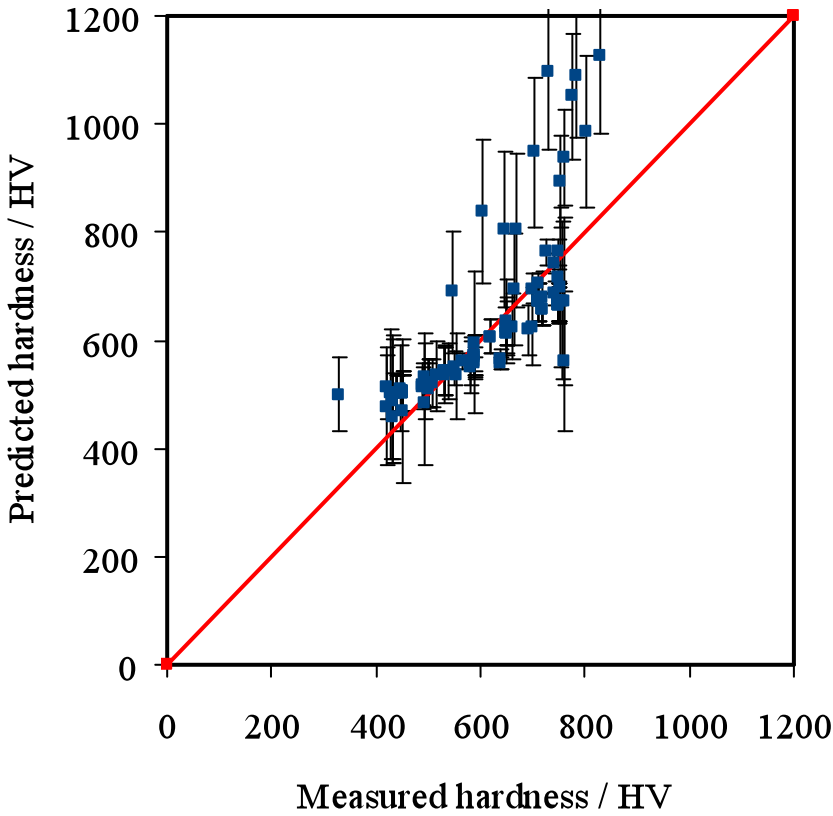
Figure 4.20: predicted values against measured values for model (hardness_1).
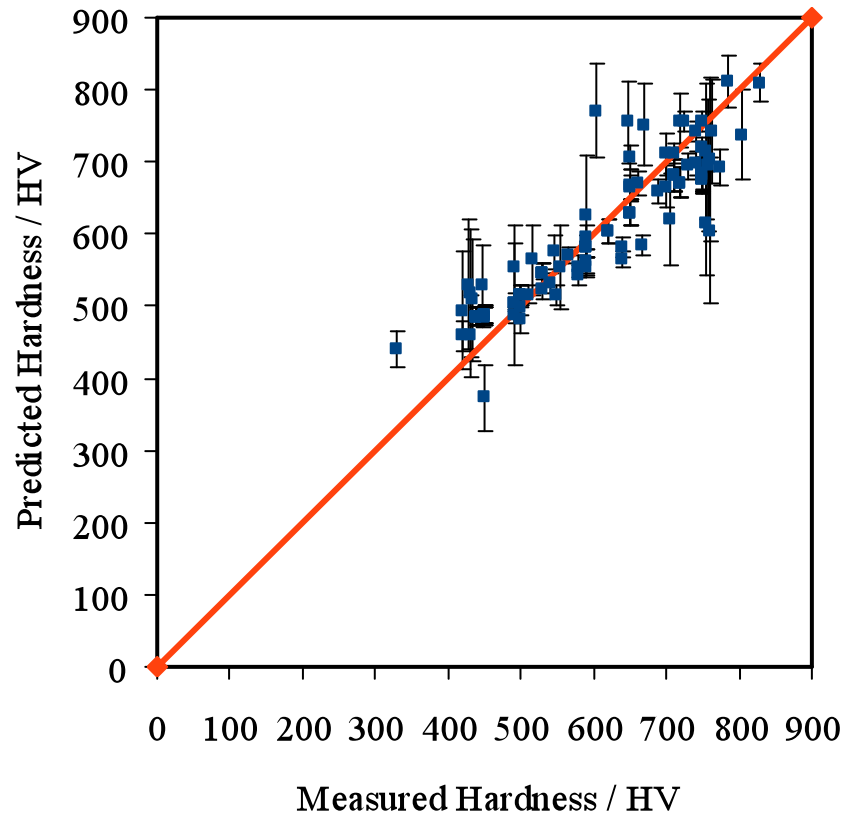
Figure 4.21: Predicted values against measured values for model (hardness_2).
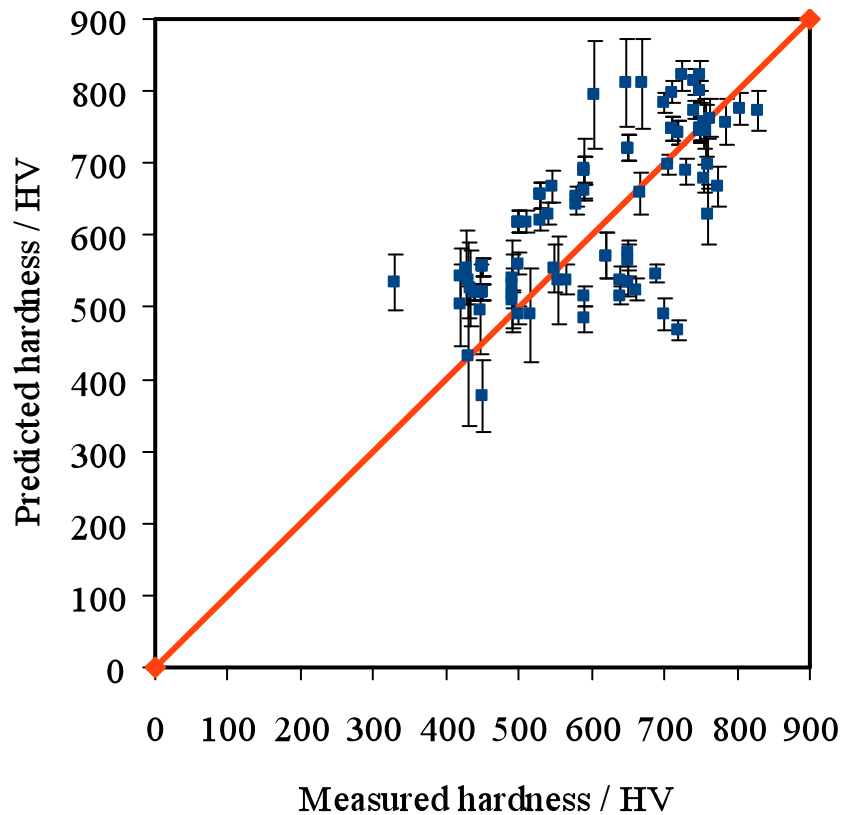
Figure 4.22: Predicted values against measured values for model (hardness_3).

4.7 Conclusions

Three neural network models are presented with different data sets to predict the hardness for steel and to make comparisons between the performances of these models. It is found model hardness_2 has the least difference between the perceived error and the root mean squared error.

The model hardness_2, which is based on direct quenching and isothermal transformation dataset, proved to be the most compatible with the experimental results. This is used to demonstrate some of the trends, by varying the contents of one variable and keeping the others constant.

The model has interpreted the behaviour of the alloying elements in considering with metallurgical theory and has been found to be reliable, i.e. carbon has the highest effect on hardness against all other alloying elements; the transformation temperature and volume fraction of bainite are also form to be segregate.

With a neural network technique, interpretation of the combined effect of variables can also be carried out using contour plots.

The best model in prediction hardness_2 is found applicable even for data outside the range used for training the models.

Chapter 5

Bainite

5.1 Introduction

Bainite is formed during the decomposition of austenite by isothermal transformation in a temperature range where neither pearlite nor martensite form. The steels which have been studied have a microstructure containing in general a mixture of carbon free bainitic ferrite, austenite and some martensite.

The large concentration of silicon typically present in bainitic steels is a key in the development of this fine microstructure. The silicon hinders the precipitation of cementite during the bainite transformation [73].

One of the most common hardening heat treatments is isothermal transformation. The isothermal process to form bainite is defined in two stages, the first involved the formation of bainitic ferrite and the second the decomposition of carbon-enriched austenite into cementite [79]. Between the two stages, there is what is called "a processing window" where heat treatment can be conducted without danger of carbide precipitation, figure 5.1. The first stage starts without any bainite and at

the end of stage I, both bainite and retained austenite contents are maximised. In the second stage, further bainite does not form but continuous carbide precipitation leads to a reduction in the amount of austenite. The isothermal transformation temperature defines the maximum volume fraction of bainite that can be observed [16].

This chapter describes a neural network model to estimate the volume percent of bainite for a wide range of steels as a function of chemical composition, austenitisation temperature, isothermal transformation temperature and Vickers hardness.
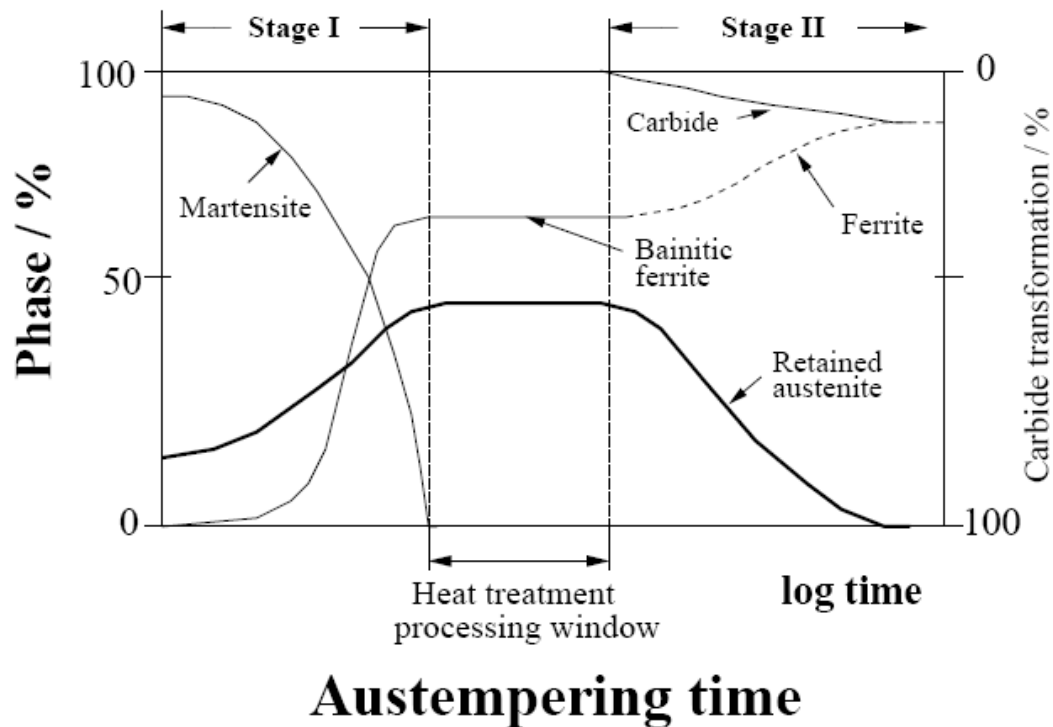
Figure 5.1: Schematic representation of the development of microstructure during austempering, together with an illustration of the "processing window" [80].

5.2 Previous models

There are two previous artificial neural networks to estimate the volume percent of retained austenite. The model was intended to create a mechanism-based model capable of estimating the maximum volume percent in austempered ductile irons [81]. The intention of the second model was to estimate the amount of retained austenite in transformation-induced plasticity assisted steels [82, 83]. These two models have been published and were used to optimize the microstructure of these steels. No model was found which is based on neural network to estimate the volume percent of bainite. Some models dealt with the kinetics of the bainite transformation, such as the physical mechanism of transformation [84, 85].

5.3 The Inputs and output

The model was built by analysing a data set which is based on experimental results published in an atlas of isothermal transformation diagrams [70]. The set of inputs in table 5.1 has approximately the same inputs as the model used to estimate Vickers hardness in the previous chapter except that the bainite volume percent is an output and the hardness an input. A total of 449 experimental data were collected from [70], including information about super-bainite [21, 31, 34, 86]. The martensite-start temperature was not removed from the input data as in chapter four, only A_{e1} and A_{e3} were removed from the input variables for the same reason as explained in chapter four. Some values of martensite-start temperature were calculated from the program mucg-73 if they were missing from the publish set [87].   The data were only collected for the isothermal transformation process to form bainite; direct quenching or tempering data were excluded in this data set.

Table 5.1: The variables in the data set.

Parameter	Minimum	Maximum	Average	Standard deviation
C / wt%	0.11	1.08	0.58	0.34
Si / wt%	0.09	1.57	0.29	0.27
Mn / wt%	0.30	2	0.72	0.38
Ni / wt%	0.00	4.33	2.03	1.45
Cr / wt%	0.10	1.55	0.87	0.39
Mo / wt%	0.01	1.05	0.25	0.27
Transformation temperature / °C	190	750	485	142
Ms / °C	53	455	257	115.3
Austenitisation temperature / °C	770	1000	882	89.9
Hardness / HV 30 kg	158	945	412	154
Volume percent of bainite	0	100	77	35
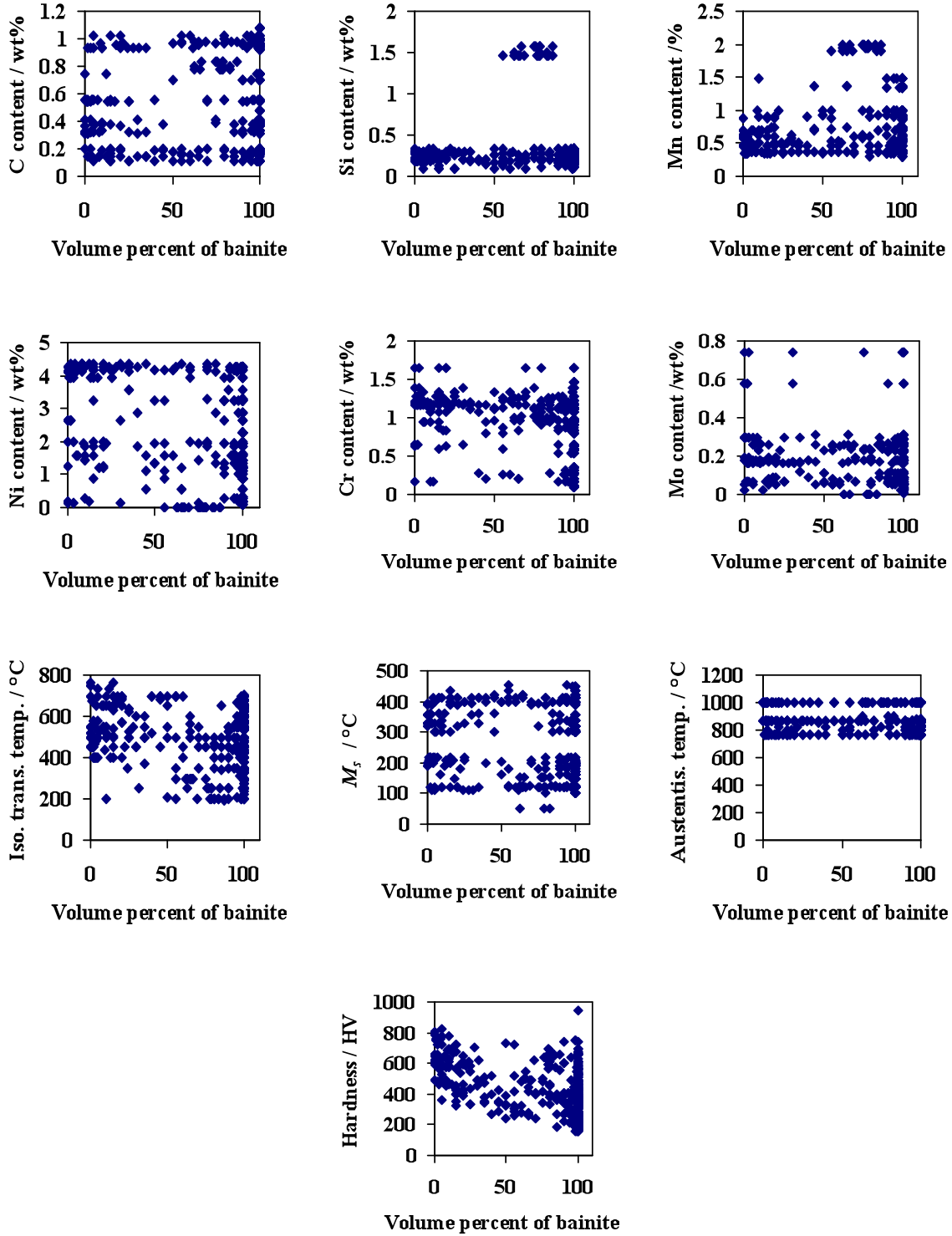
Figure 5.1: The distribution of inputs against volume percent of bainite.

5.4 Model training

The data were normalised between -0.5 and +0.5 and split into two sets, training set and testing set, as explained previously in chapter two. The maximum number of hidden units was twenty and the maximum number of seeds was five, the total number of models created during training was a hundred. Figure 5.2a shows the noise level decreases as the number of hidden units decrease. Examining the performance of the model is come from testing unseen data (testing set). Figure 5.2b shows the test error tends to reach a minimum value when the hidden units was eight. The ranked models depend on the values of the test error and maximum value for LPE it was reach maximum value when the hidden units was ten figure 5.2c, committees are then formed depend on best few models figure 5.2d shows the combined test error reaches minimum value with thirty four models.

The final committee is used to make predictions on the whole database in figure 5.3. There are number of outliers, *i.e*, points in the middle of the figure which are away from the line of perfect fit. Figure 5.4 shows that the hardness correlates best with V_b, followed by the isothermal transformation temperature and martensite start temperature. For the alloying elements, silicon is found to be significant because it hinders the precipitation of cementite, the formation of cementite leads to a reduction of carbon concentration in the residual austenite, thereby permitting the growth of a further amount of ferrite [16].

The influence of hardness and its effect on the amount of the volume percent of bainite in these types of steels is explored in detail later in the text.
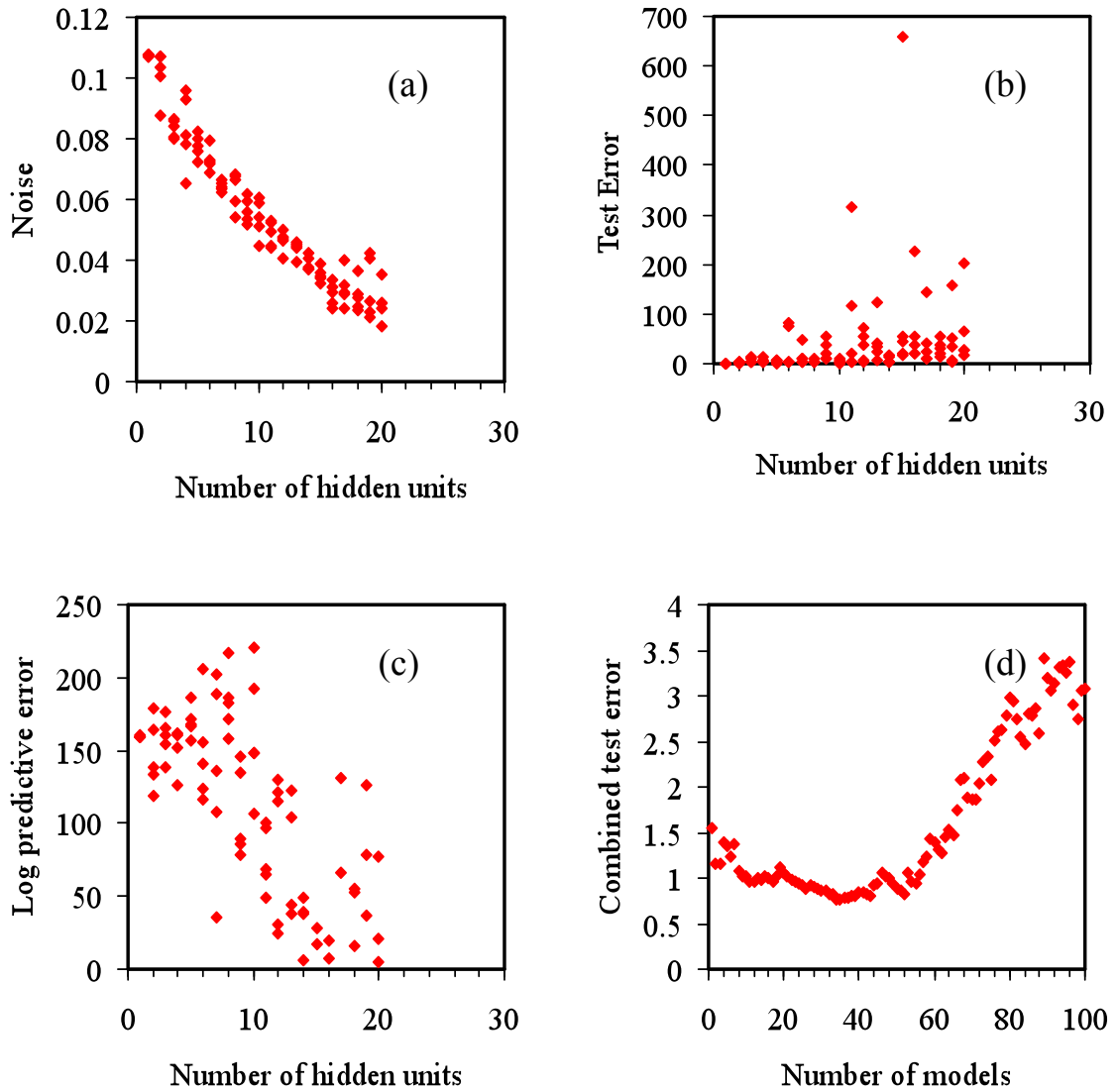
Figure 5.2: The training and testing results of the committee model. (a) Perceived level of noise against hidden units. (b) Test error against hidden units (c) Log predictive error against hidden units. (d) Test error against number of models in the committee.
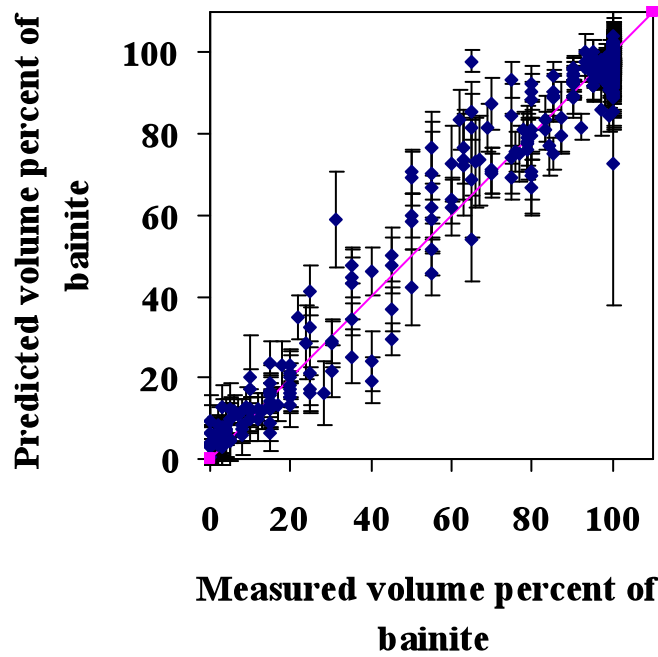
Figure 5.3: Predicted verses measured volume percent of bainite, the predictions being based on of the committee model.
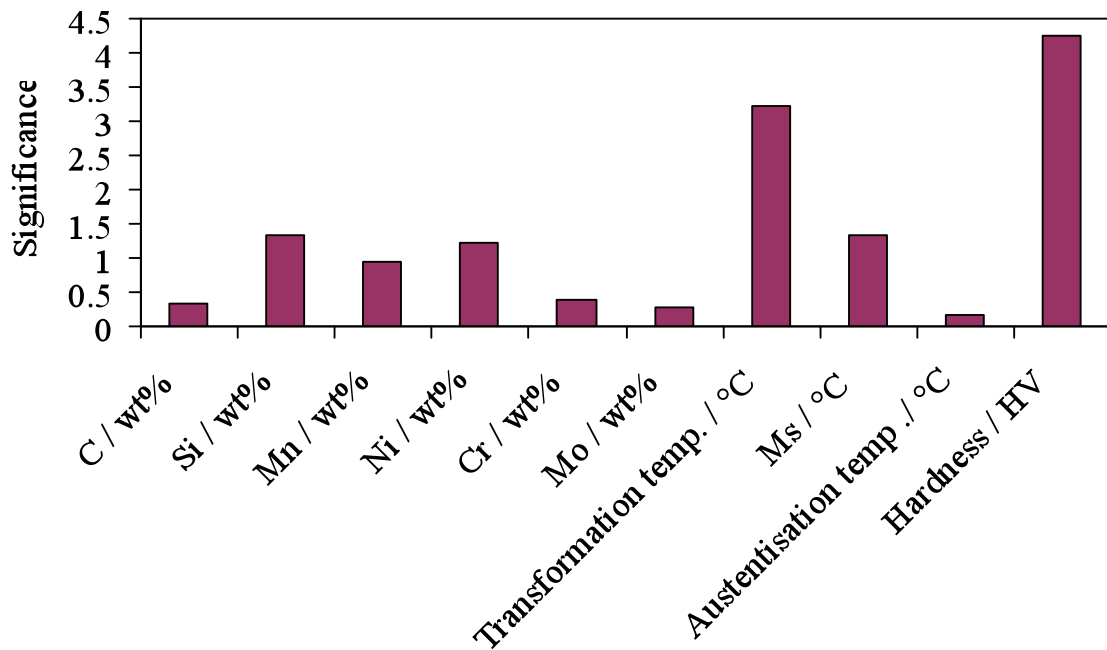
Figure 5.4: Significance of each variable of committee model.

5.5 Application of model

The committee is usually used to study the effects of individual variables on the output, but in this case it is impossible to study these effects on volume percent of bainite because one of these inputs, *i.e.* Vickers hardness, has correlation with all other parameters, specially with composition and heat treatments [42], as was explained in chapter two. Therefore, real values for hardness should be available for each case and then this work can make a prediction for these cases. For example, if it is intended to use the model to predict the volume fraction of bainite as the concentration of each of the alloying elements changes for the alloy of super-bainite which was used in chapter four and six with the composition 0.98C- 1.45Si- 1.89Mn-1.25Cr- 0.25Mo wt% [88], it should be taken into consideration that the hardness for this composition will change with any change in the concentration of the alloying elements. In physical terms, care must be taken of the metallurgical principles.

The simple metallurgy of steels concerned with super-bainite can be summarized as follows [89]:

- Maximization of the fraction of bainite, involves transformation at lowest possible temperature.

- Silicon can be added to suppress brittle cementite in high strength steels.

- Both pearlite and allotriomorphic ferrite should be avoided during cooling [16].

Consistent with the first stage reaction, V_b first increases, but then stops according to the concept of T_0 curve with the beginning of stage II which

is connected with carbide precipitation and ferrite formation as shown in figure 5.1.

5.5 Predictability

The general performance of the model can be tested by predicting on unseen data. Table 5.2 shows the values of the unseen data within the range of the model [70]. Figure 5.5 shows the predictability of the volume percent of the bainite against the measured values.

Predictions were also made for the alloys of the super-bainite. Table 5.3 shows the input variables of these alloys which were unseen by the model. Figure 5.5 shows the predictability of the volume percent of bainite against measured values, these values fall on the forty five degrees fit line.

Table 5.2: The unseen data used for testing the predictive ability of the model, the chemical composition in wt%.

C / wt%	Si / wt%	Mn / wt%	Ni / wt%	Cr / wt%	Mo / wt%	Isothermal temperature / °C
0.11	0.21	0.35	2.89	0.28	0.09	700
0.11	0.21	0.35	2.89	0.28	0.09	550
0.95	0.25	0.4	2.29	0.35	0.08	550
0.15	0.18	0.53	1.55	0.25	0.25	500
0.15	0.18	0.53	1.55	0.25	0.25	555
0.99	0.29	0.55	1.51	0.32	0.29	355
0.99	0.29	0.55	1.51	0.32	0.29	212
0.7	0.15	0.35	3.24	0.95	0.05	525
0.7	0.15	0.35	3.24	0.95	0.05	590
1	0.12	0.3	3.27	0.9	0.07	510
1	0.12	0.3	3.27	0.9	0.07	550
1	0.12	0.3	3.27	0.9	0.07	440
0.11	0.09	0.38	4.15	1.33	0.07	500

0.11	0.09	0.38	4.15	1.33	0.07	450
0.54	0.25	0.34	3.92	1.28	0.07	550
0.54	0.25	0.34	3.92	1.28	0.07	550
1.02	0.27	0.47	4.15	1.22	0.05	250
1.02	0.27	0.47	4.15	1.22	0.05	200
0.15	0.2	0.38	4.33	1.15	0.17	700
0.17	0.22	0.88	0.85	0.59	0.05	500
0.17	0.22	0.88	0.85	0.59	0.05	450
0.92	0.3	0.93	0.9	0.57	0.03	581
0.92	0.3	0.93	0.9	0.57	0.03	550
0.2	0.15	0.71	1.13	0.8	0.05	500
0.2	0.15	0.71	1.13	0.8	0.05	450
0.95	0.25	0.74	1.19	0.84	0.09	700
0.95	0.25	0.74	1.19	0.84	0.09	580
0.18	0.25	0.93	1.34	1.11	0.11	500
0.18	0.25	0.93	1.34	1.11	0.11	450
1	0.28	0.99	1.42	1.12	0.11	530
1	0.28	0.99	1.42	1.12	0.11	580
0.33	0.21	0.52	0.89	0.1	0.05	530
0.33	0.21	0.52	0.89	0.1	0.05	420
0.19	0.14	1.37	0.55	0.2	0.31	580
0.19	0.14	1.37	0.55	0.2	0.31	550
0.31	0.2	0.52	2.53	0.54	0.58	400
0.8	1.5	2	0	1	0	250
0.78	1.45	1.95	0	0.97	0	200
0.83	1.57	1.98	0	1.02	0.24	300
0.83	1.57	1.98	0	1.02	0.24	250
0.78	1.45	1.95	0	0.97	0	300

Table 5.2(continued): The unseen data used for testing the predictive ability of the model, the chemical composition in wt%.

Austenitisation temperature / °C	Ms / °C	Hardness / HV	Predicted Volume percent	Error bars	Measured Volume percent
855	450	280	35.3	5.778	40
855	450	198	82.4	4.542	85
855	120	810	18.5	15.1	0
855	455	174	99.4	2.403	100
855	455	230	92.9	4.038	90
770	159	474	100	2.992	100
770	159	752	91.5	9.971	100
850	189	252	97.5	3.039	100
850	189	309	94.25	2.552	100
850	100	282	99	3.325	100
850	100	354	95.8	3.509	100
850	100	454	88	7.371	80
770	400	372	25.8	4.887	35
770	400	332	52	5.219	52
855	219	593	12.9	4.259	20
855	219	312	92	3.444	100
770	121	570	89.4	3.959	100
770	121	720	45.4	7.192	25
855	352	490	7.8	7.513	3
830	421	235	99	2.345	100
830	421	274	101	3.19	100
870	150	250	99.8	2.573	100
870	150	284	99.4	2.031	100
800	410	285	94.2	3.852	100
800	410	321	98.47	3.079	100
855	120	595	15.2	4.484	20
855	120	242	99.7	3.383	99
800	400	393	59.78	5.5	50
800	400	310	98	2.75	98
880	120	325	99	2.381	100

880	120	375	98.3	2.828	100
1000	357	302	95.75	3.743	100
1000	357	445	91.48	5.805	100
1000	420	289	50	5.707	45
1000	420	159	97.5	2.501	100
1000	357	355	92	3.751	90
900	53	589	78.97	7.955	79
1000	155	550	80.78	4.498	83
1000	120	500	74	10.42	75
1000	120	540	75	4.933	75
1000	155	490	73	11.04	55
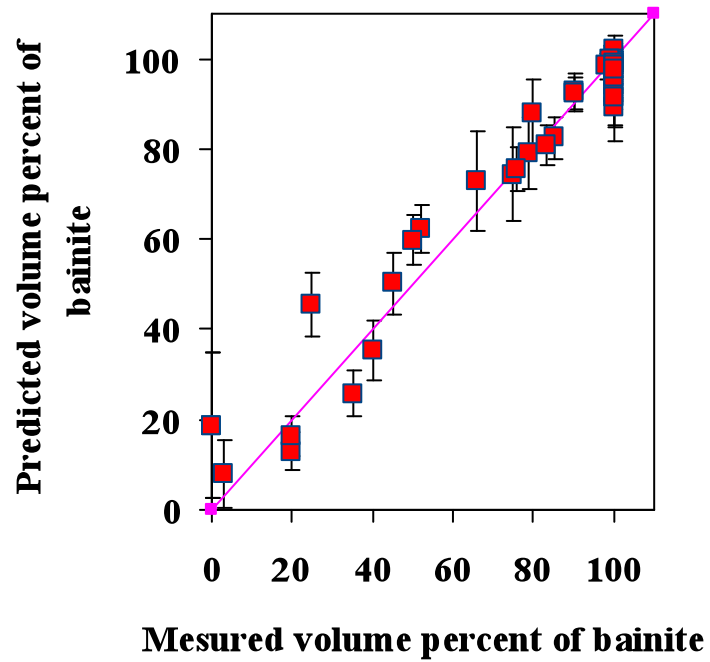
Figure 5.5: Predicted volume percent of bainite against measured volume percent of bainite of the committee model for unseen data.

Table 5.3: The unseen data used for testing the predictive ability of the model concerning super-bainite.

C / wt%	Si / wt%	Mn / Wt%	Ni / wt%	Cr / wt%	Mo / wt%	Isothermal temperature / °C
0.97	1.43	1.59	0.04	0.25	0	200
0.98	1.45	1.89	0	1.25	0	200
0.98	1.45	1.89	0	1.25	0	190
0.98	1.45	1.89	0	1.25	0	250
0.98	1.45	1.89	0	1.25	0	300
0.8	1.59	2	0	1	0	200
0.8	1.59	2	0	1	0	250
0.8	1.59	2	0	1	0	300
0.78	1.49	1.95	0	0.79	0.24	200
0.78	1.49	1.95	0	0.79	0.24	250
0.78	1.49	1.95	0	0.79	0.24	300
0.97	1.43	1.59	0.04	0.25	0	200
0.79	1.55	1.98	0	1.01	0.24	200
0.79	1.55	1.98	0	1.01	0.24	250
0.79	1.55	1.98	0	1.01	0.24	300

Table 5.3 (continued): The unseen data used for testing the predictive ability of the model concerning super-bainite.

Ms / °C	Austenitisation temperature / °C	Hardness / HV	Predicted Volume percent	Error bars	Measured Volume percent
120	1000	720	87.73	17.19	80
120	1000	519	80.12	7.74	59
120	1000	550	80.34	5.23	87
120	1000	575	75.01	9.47	84
120	1000	440	55.1	17.55	55
80	900	550	82.89	5.07	83
80	900	589	78.59	7.92	79
80	900	500	72.5	12.22	53
155	1000	550	82.15	5.77	87
155	1000	555	79.58	7.55	79
155	1000	500	75.14	9.87	74
110	1000	545	87.49	19.31	80
132	920	540	83.8	5.84	58
132	920	530	77.35	5.85	72
132	920	500	75.25	9.33	50

Table 5.5 shows the perceived error of the models and the root mean squared error, to compare the performances of the model. The committee of the model has good predictability; the perceived error and the root mean squared error have a small difference between them for seen and unseen data.

Table 5.5: The performance of the model in terms of the root mean squared error and perceived error.

Type of data	Root mean squared error	Perceived error
Seen data	5.9	4.3
Unseen data	7.1	5.2
Unseen data for super-bainite	5.1	9.9
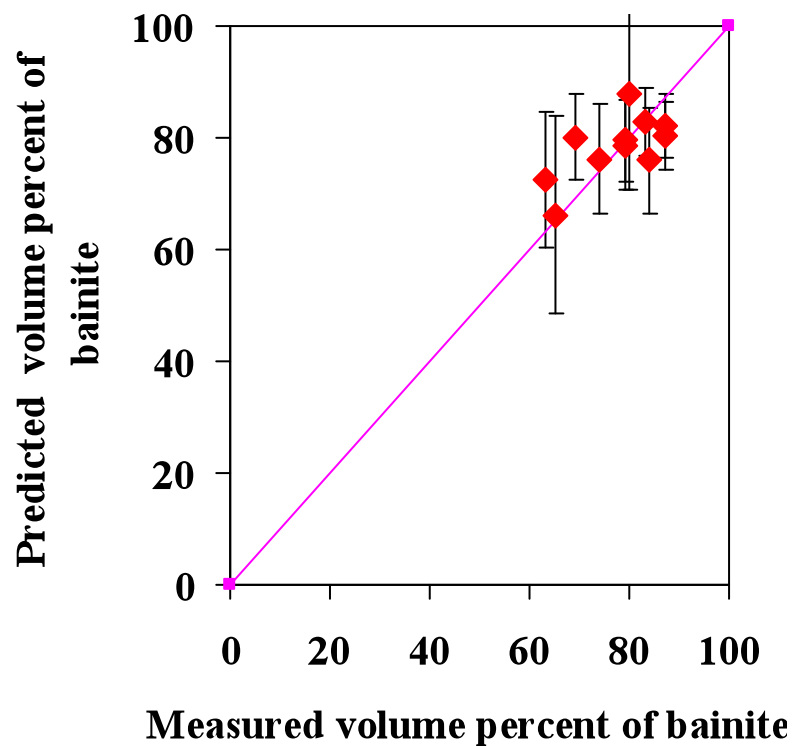
Figure 5.5: Predicted volume percent of super-bainite against measured volume percent of bainite for the committee model for unseen data.

5.7 Conclusions

A neural network has been used to estimate the volume percent of bainite as a function of chemical composition, heat treatment and hardness. It has successfully made predictions for a wide range of steels. This model can be used to predict the fraction of bainite for super-bainite steels by knowing the input variables. New experiments can then be considered. Hardness has shown high significance in the model, because it is directly correlated to the time needed to form bainite.

Chapter 6

Plane strain fracture toughness

6.1 Introduction

The Bayesian neural network method used here was previously described in chapter two. It has been successfully applied in complicated materials problems which include the modelling and optimisation of Charpy impact energy and strength of steel weld metals [11], the yield and ultimate tensile strength of nickel-base superalloys, the behaviour at high-temperature of creep resistant steels, and properties of polymeric and inorganic compounds and ceramics. A review of these applications is given in [50]. In addition, this modelling method has been also applied to plane strain fracture toughness for specific types of steels [90-92].

Diverse models exist for predicting plane strain fracture toughness. These include microstructural parameters with general functions [6, 7]. As the microstructural parameters vary according to material and plane strain conditions, this approach is only weakly predictive.

Simple dispersed barrier models do not predict plane strain fracture toughness and more complex versions have fitting parameters which cannot be generalised [93]. As it stands, there are no previous models

which flexibly estimate a range of observed behaviour and are quantitative. Bayesian network models are both flexible and quantitative, and also provide a measure of modelling uncertainty, allowing calculations from far outside the knowledge base to be identified and approached with caution [94, 95].

The aim of this chapter is to predict the plane strain fracture toughness; the data have been collected from published literature. Different types of steels and austempered ductile irons have been included in these data to create the model.

6.2 Plane strain fracture toughness database

Many attempts were made to build the best model capable of estimating the value of K_{Ic} correctly. Three general models have been created which depend on the choice of input variables. These models are:

1- Mechanical properties model.

2- Chemical composition model.

3- Chemical composition, heat treatment and mechanical properties model.

Since the K_{Ic} is a function of many variables, the choice of the inputs for the third model is as follows:

$$K_{Ic} = f(C_i, T_a, T_{t1}, t_{t1}, T_{t2}, t_{t2}, M) \tag{6.1}$$

where C_i is the chemical composition (carbon, manganese, silicon, chromium, nickel and molybdenum), T_a the austenitisation temperature °C, T_{t1} the transformation temperature °C, t_{t1} the hold time at temperature in minutes , T_{t2} the second step temperature °C, t_{t2} the hold time for the

second step temperature in minutes and M_p mechanical properties (yield, ultimate, elongation and hardness).

6.2.1 Input variables for mechanical properties model.

A data set was built up by collecting, a total of 269 data from published literatures (Appendix A). The input variables included yield stress, ultimate tensile stress and elongation for a wide range of steels as well as super-bainitic steels [89]. Table 6.1 shows the maximum, minimum and standard deviation of the database and figure 6.1 shows a graphical representation of the database.

The data set did not include any artificial input parameters which are functions of the inputs.

Table 6.1: Data used to build the mechanical properties model.

Variables	Minimum	Maximum	Average	St. Dev
Yield stress / MPa	260	2678	1151	430
UTS / MPa	390	2722	1421	470
Elongation / %	0.06	74.7	10	8
K_{Ic} / MPa m$^{0.5}$	11.39	295	71	37

6.2.2 Input variables for chemical composition model

The input to this model is only the chemical composition in wt%. A total of 1017 experimental data were collected from the published literature (Appendix A) for nine variables. The minimum and maximum

values for each variable are listed in table 6.2, and figure 6.2 shows the distribution of inputs against the target.
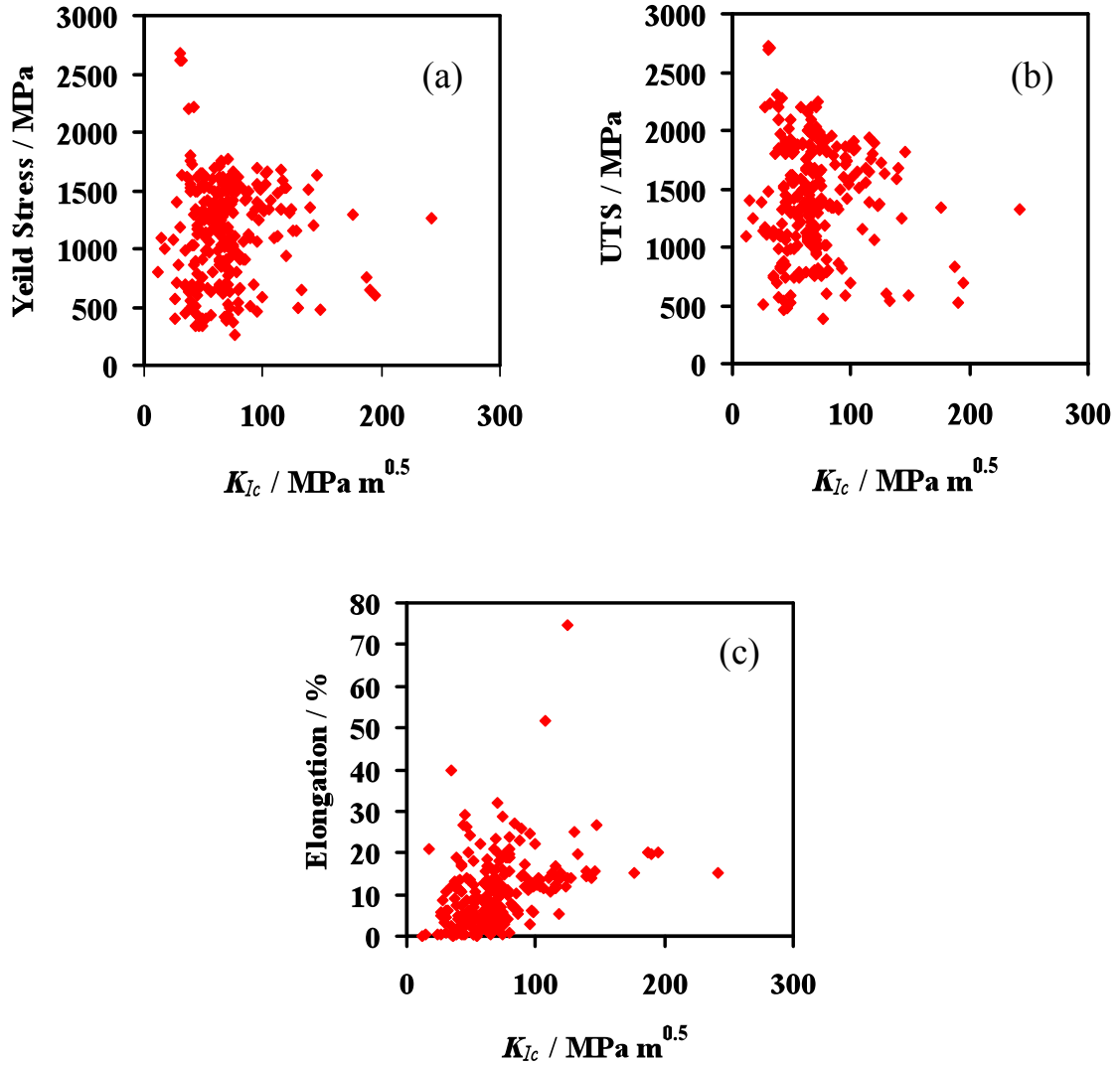
Figure 6.1: Distribution of inputs against K_{Ic} for the mechanical properties model.

Table 6.2: Data used in the chemical composition model.

Variables	Minimum	Maximum	Average	St. Dev
C / wt%	0.0020	3.8	1.03	1.18
Si / wt%	0.0	3.2	0.92	0.97

Mn /wt%	0.0	13.2	0.62	0.57
P / wt%	0.0	0.48	0.0154	0.02
S / wt%	0.0	0.46	0.02	0.06
Mg / wt.%	0.0	2	0.03	0.16
Cu / wt%	0.0	1.6	0.109	0.23
Cr / wt%	0.0	18.9	1.47	2.67
Ni / wt%	0.0	70	1.64	3.52
K_{Ic} / MPa m$^{0.5}$	5.5	445	63.26	42.94
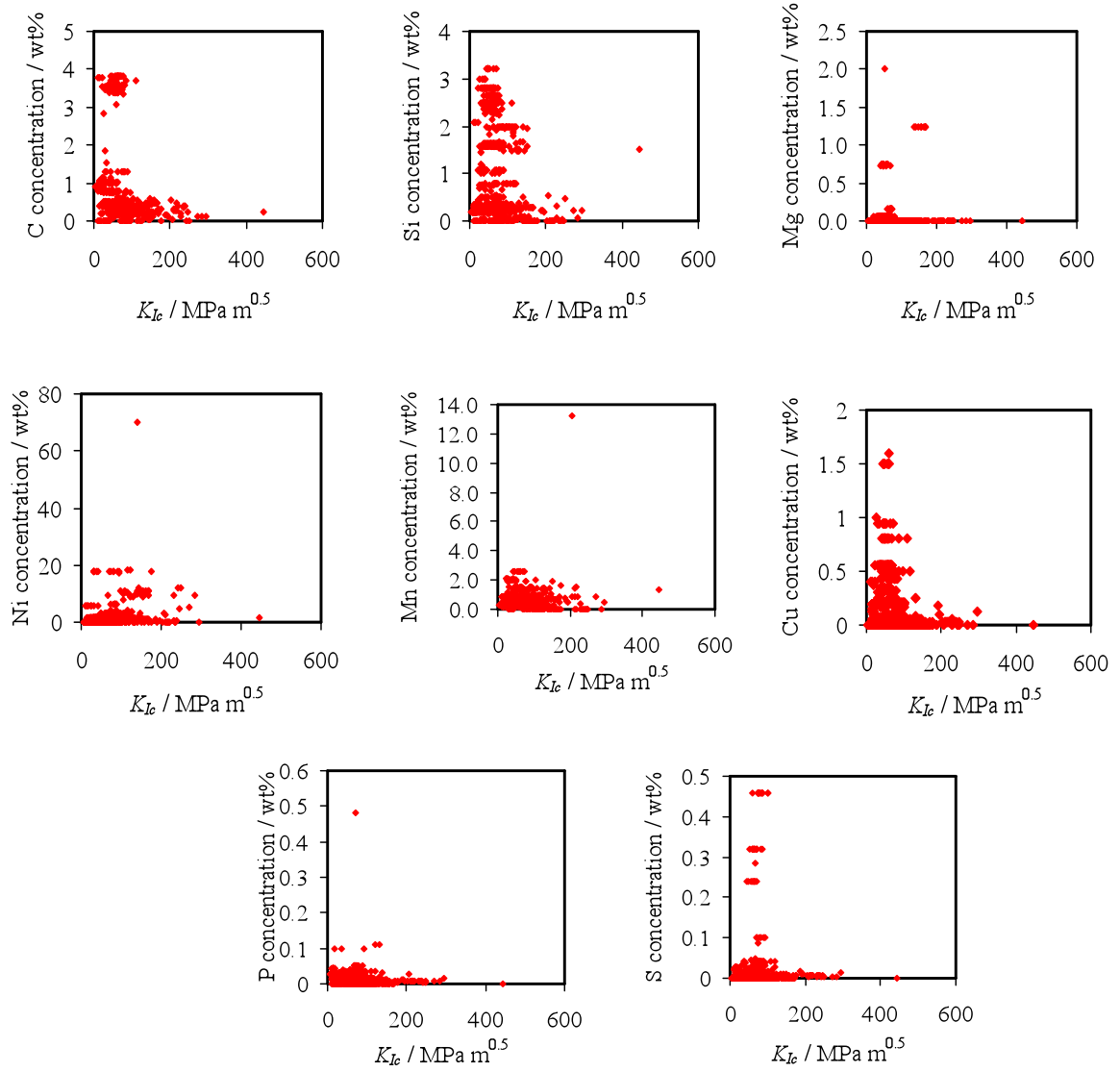
Figure 6.2: Distribution of inputs against K_{Ic} for the chemical composition model.

6.2.3 Input variables for chemical composition, heat treatment and mechanical properties model

There are data which are currently available and reported for the fracture toughness of different types of steel. This new data set has more inputs than the other datasets which were explained in the previous sections. A data set consisting of 394 experiments was compiled (Appendix A) including seventeen variables. The decision was made to exclude the dimensions of the test sample, the orientation of the notch and the loading direction of the sample. This may add noise to the calculation of toughness but including these variables would limit the size of the dataset. When the austenitizing temperature was missing in the data, it was estimated from other data with approximately similar carbon content or from the A_{e3} temperature for that steel. When either the hardness or yield strength was a missing, it was estimated from the relationship $\sigma_y = h/3$. When the UTS was missing in the data, it was estimated by adding 300 MPa to the yield stress value. Hardness values in Rockwell and Brinell were converted to Vickers hardness before being fed to the data [8]. The minimum and maximum values for each variable are presented in table 6.3, and figure 6.8 shows the distribution of input against the output.

All the data which were collected from literature represents tests carried out at room temperature.

Table 6.3: Data used in the chemical composition, heat treatment and mechanical properties model.

Variables	Minimum	Maximum	Average	St. Dev
C / wt%	0.040	3.81	1.52	1.43
Si / wt%	0	3.21	1.33	1.10
Mn / wt%	0.04	2.58	0.63	0.42
P / wt%	0	0.48	0.015	0.02
S / wt%	0	0.46	0.03	0.102
Mg / wt%	0	1.25	0.07	0.21
Cu / wt%	0	1.60	0.183	0.31
Cr / wt. %	0	16.91	1.28	2.94
Ni / wt%	0	10.06	1.157	1.21
Austenitisation temp. / °C	816	1423	936	104
Temperature step 1 / °C	30	780	161	150
Time step 1 / min	2	14400	137	812
Temperature. Step 2 / °C	28	720	226	205
Time step 2 / min	30	5400	112	402
Yield stress / MPa	236	2300	1174	388
UTS / MPa	436	3600	1441	500
Hardness / HV	48.96	889	547	188
K_{Ic} / MPa m$^{0.5}$	9.8	295	62.7	35
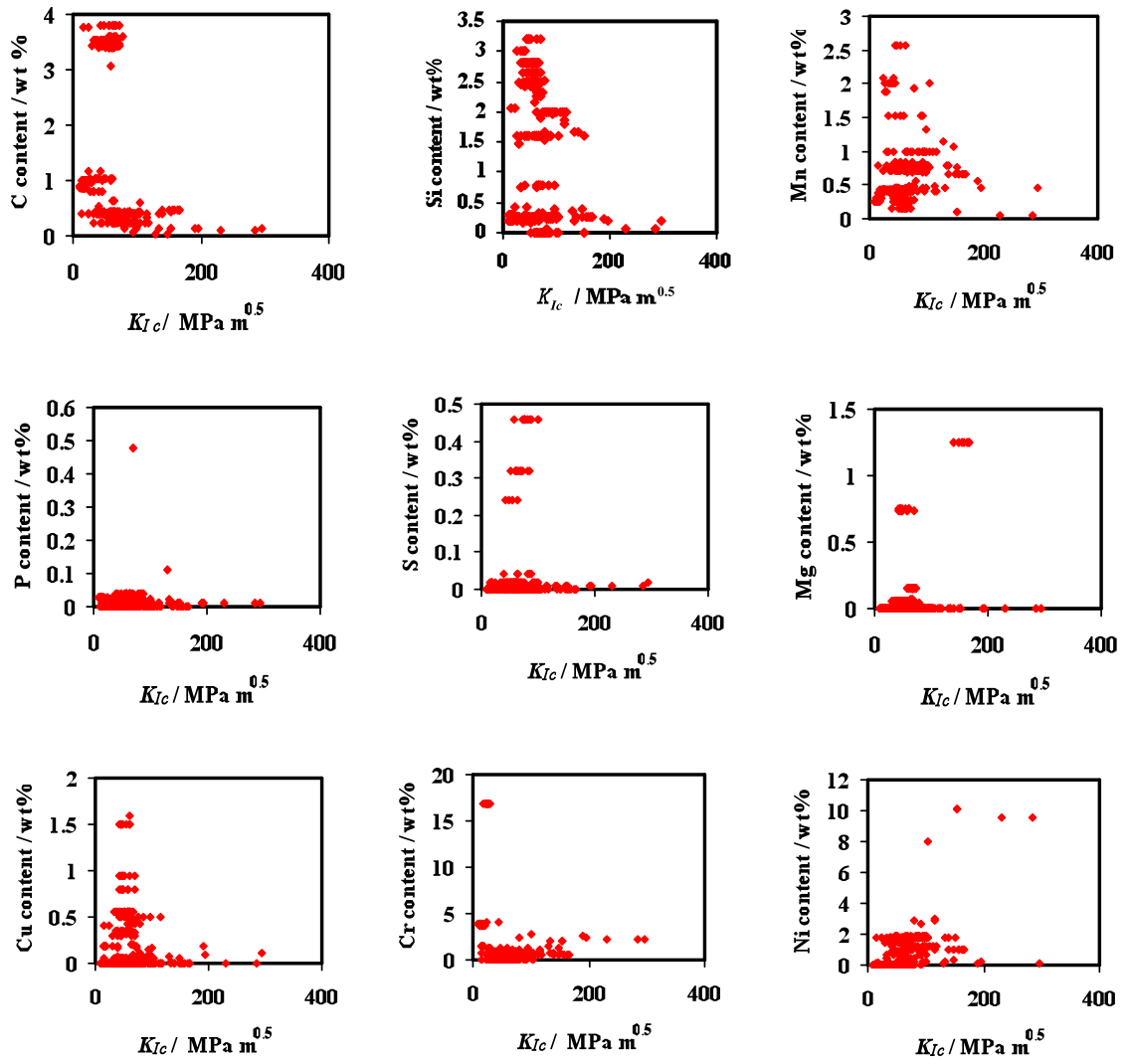
Figure 6.3: Distribution of inputs against the K_{Ic} for the chemical composition, heat treatment and mechanical properties model.
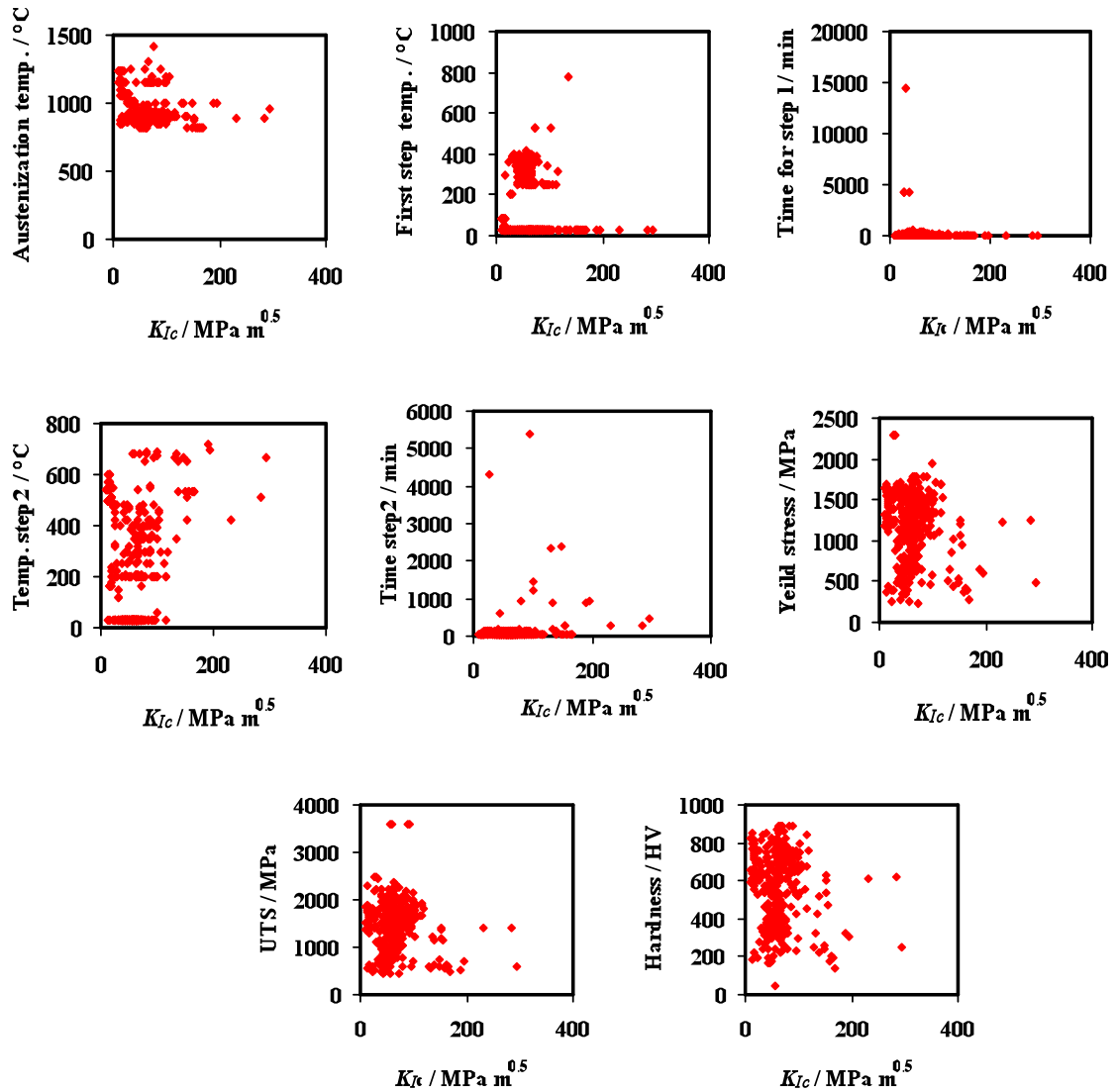
Figure 6.3 (continued): Distribution of inputs against the K_{Ic} for the chemical composition, heat treatment and mechanical properties model.

6.3 Models training

The three different approaches, for the three models were trained by using neural network technique.

6.3.1 Training Mechanical Properties model

The data set of mechanical properties was used to create six committee models using Bayesian neural networks with different conditions. Each model has a different number of hidden units and random seed to initiate the values of weights.

Figure 6.5a-f shows plots of predicted versus actual output using the committee models from one to six on the whole dataset. There are large numbers of outliers in all the models, which represent, bad predicted values even for the data already trained and tested.

The root mean square and perceived errs were calculated manually for these six models to compare the performance of these committees as shown in table 6.4. Model_2 has the least root mean squared error and the least difference between the mean square and perceived error which represents standard deviation, in the ideal case the two values should be equal.

Figure 6.6 shows the significance for the best model (model_2). Percentage elongation has the highest significance, followed by the yield stress and ultimate tensile strength in that order.

Due to the poor predictions in all the mechanical properties models, it is not recommended to use these models unless more data can be collected from the published literature. It is also clear that mechanical property data alone cannot lead to acceptable prediction of K_{Ic} in this work, while one of the published literatures recommended the use of neural network to predict K_{Ic} values from tensile test results and crack plane orientation at room temperature [90].
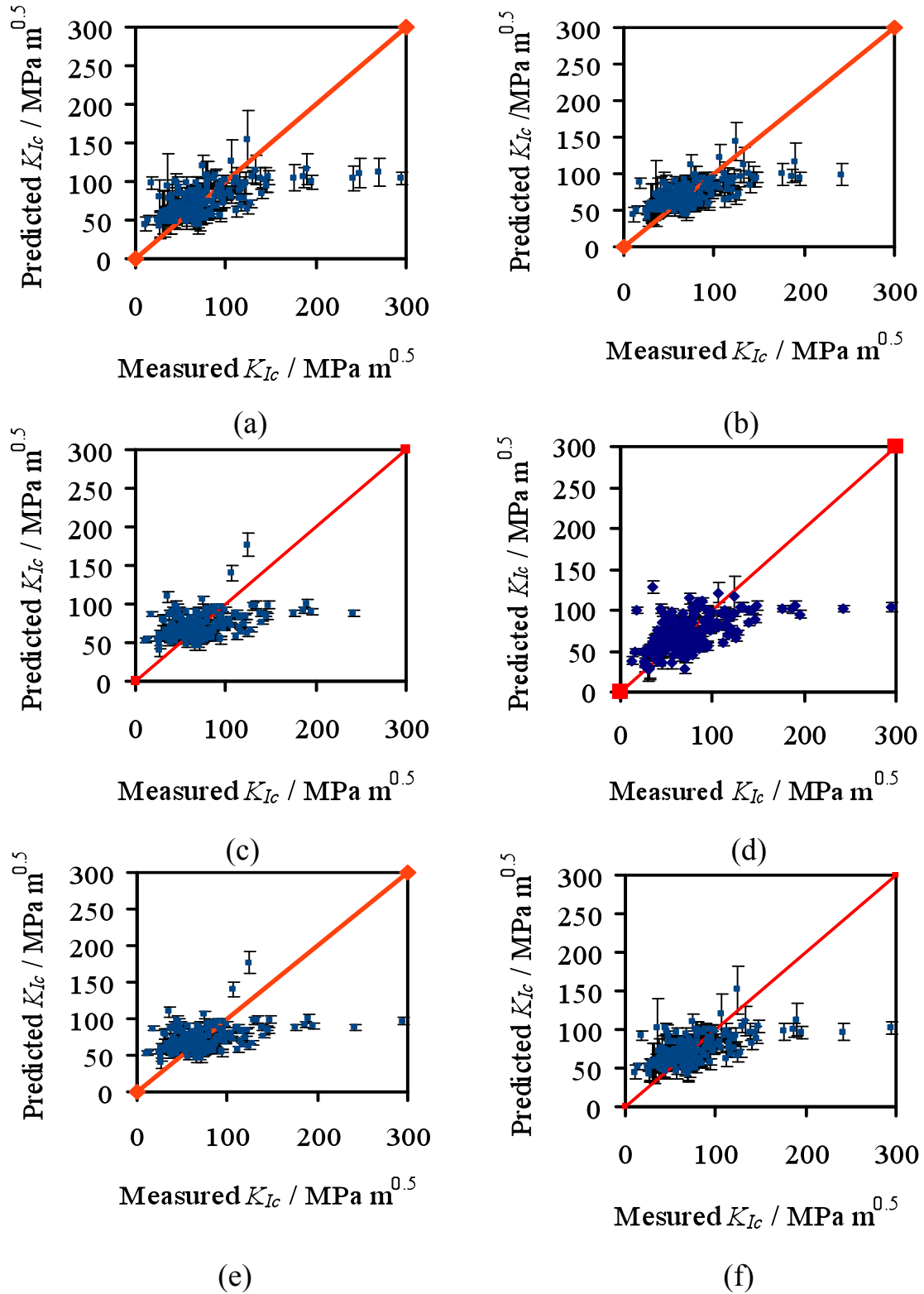
Figure 6.5a-f Plots of predicted versus measured output using the committee models from 1 to 6 on the whole dataset.

Table 6.4: Performance of the models using the root mean square and perceived error for the mechanical properties models.

The name of the model	Root mean squared error	Perceived error
Model _1	30	8.08
Model _2	24	7.6
Model_3	27	3.44
Model_4	28	4.16
Model_5	30	3.45
Model_6	27	6.88
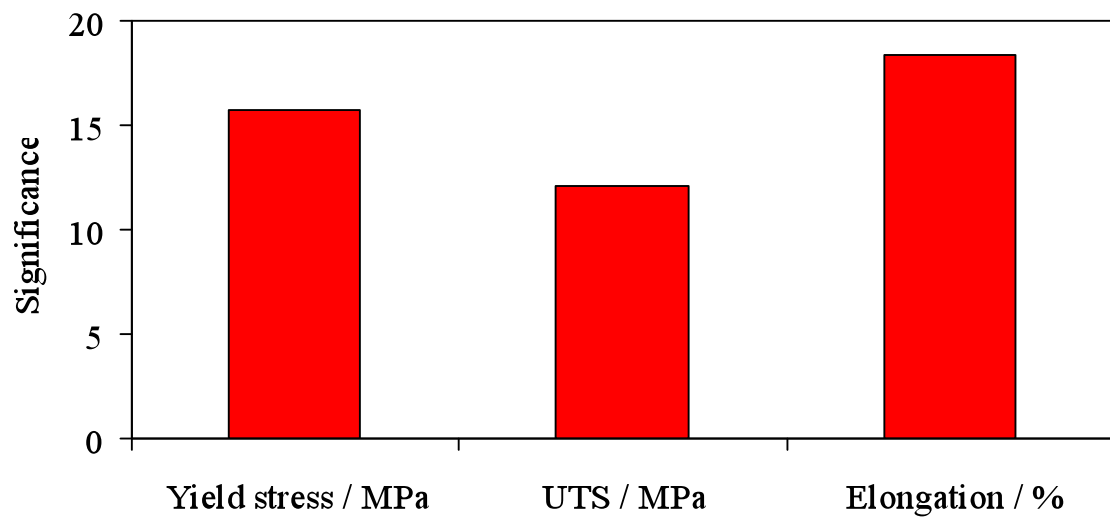
Figure 6.6: Significance for the best model (model_2) of the mechanical properties model, the inputs data listed in table 6.1.

6.3.2 Training chemical composition model

The data in table 6.2 were trained and tested as was explained in chapter two. Predictions made using this committee are illustrated in figure 6.7 for the entire data. Figure 6.8 shows the significance of the input values. It can be seen that the carbon content has the highest significance followed by manganese and nickel content both of them which have much less significance than carbon. The root mean square error has been calculated for this model as listed in table 6.5.

Table 6.5: Performance of the chemical composition model by using root mean square and perceived error.

The name of the model	Root mean squared error	Perceived error
Chemical composition model	31.94	9.74

It is not recommended to use the chemical composition data alone as input since it gives poor prediction. With the same chemical composition, different experimental values for K_{Ic} can be observed depending on heat treatment and other parameters.
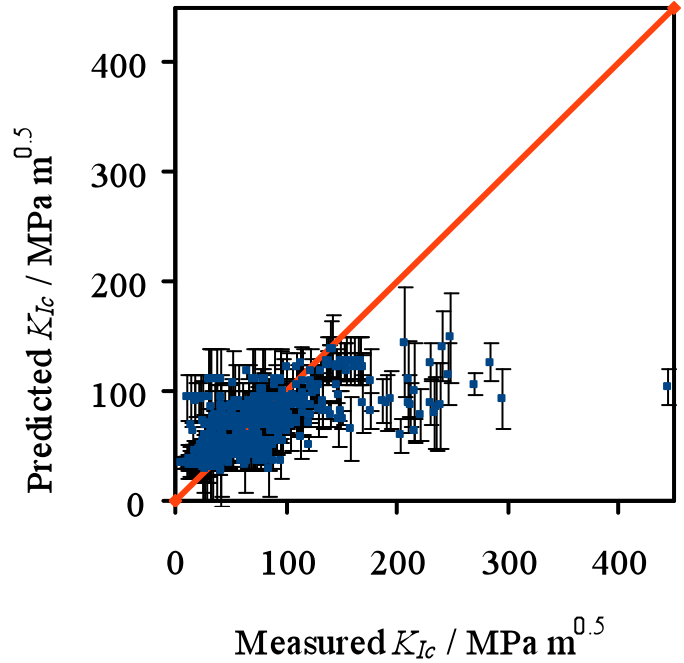
Figure 6.7: Predictions by the best model for the entire data set using the committee for the chemical compositions model, the inputs data listed in table 6.2.
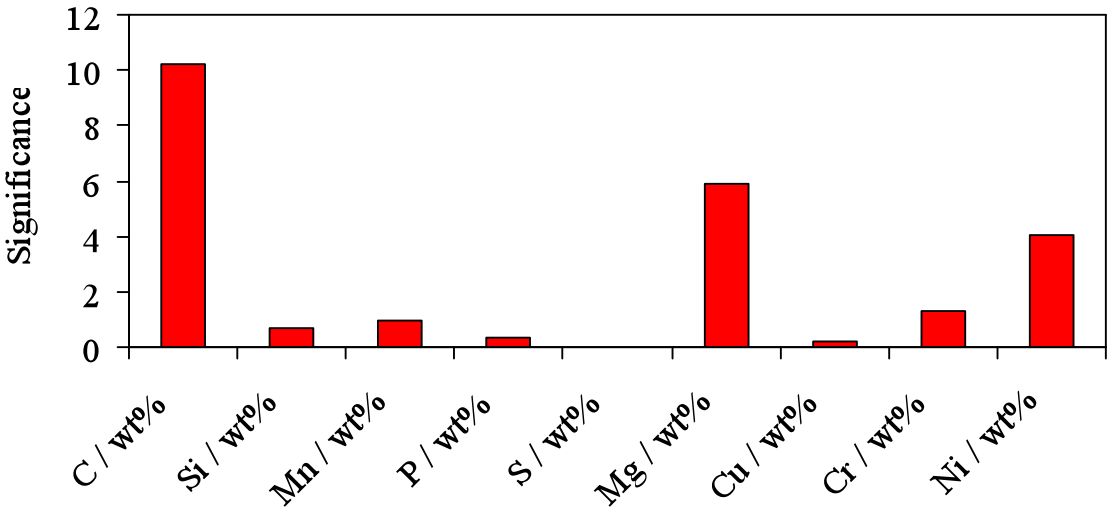
Figure 6.8: Significance for the committee of the chemical compositions model, the inputs listed in table 6.2.

6.3.3 Training the chemical composition, heat treatment and mechanical properties model

Three models were built with different training and testing sets, using the data in table 6.3. Model_2 has the minimum root mean square error and the least difference between the mean square and perceived error as shown in table 6.6. Figure 6.9(a-c) shows prediction of the entire data for all committees model. Figure 6.10 illustrates the significance of each of the input variables in influencing the plane strain fracture toughness K_{Ic}. It has been found that the carbon content has the most significance followed by the lesser influence of the austenitisation temperature.

Table 6.6: Performance of the models using the root mean square and perceived error for the chemical composition, heat treatment and mechanical properties model.

The name of the model	Root mean squared error	Perceived error
Model _1	16.69	3.94
Model _2	10.82	8.06
Model _3	14.22	4.84
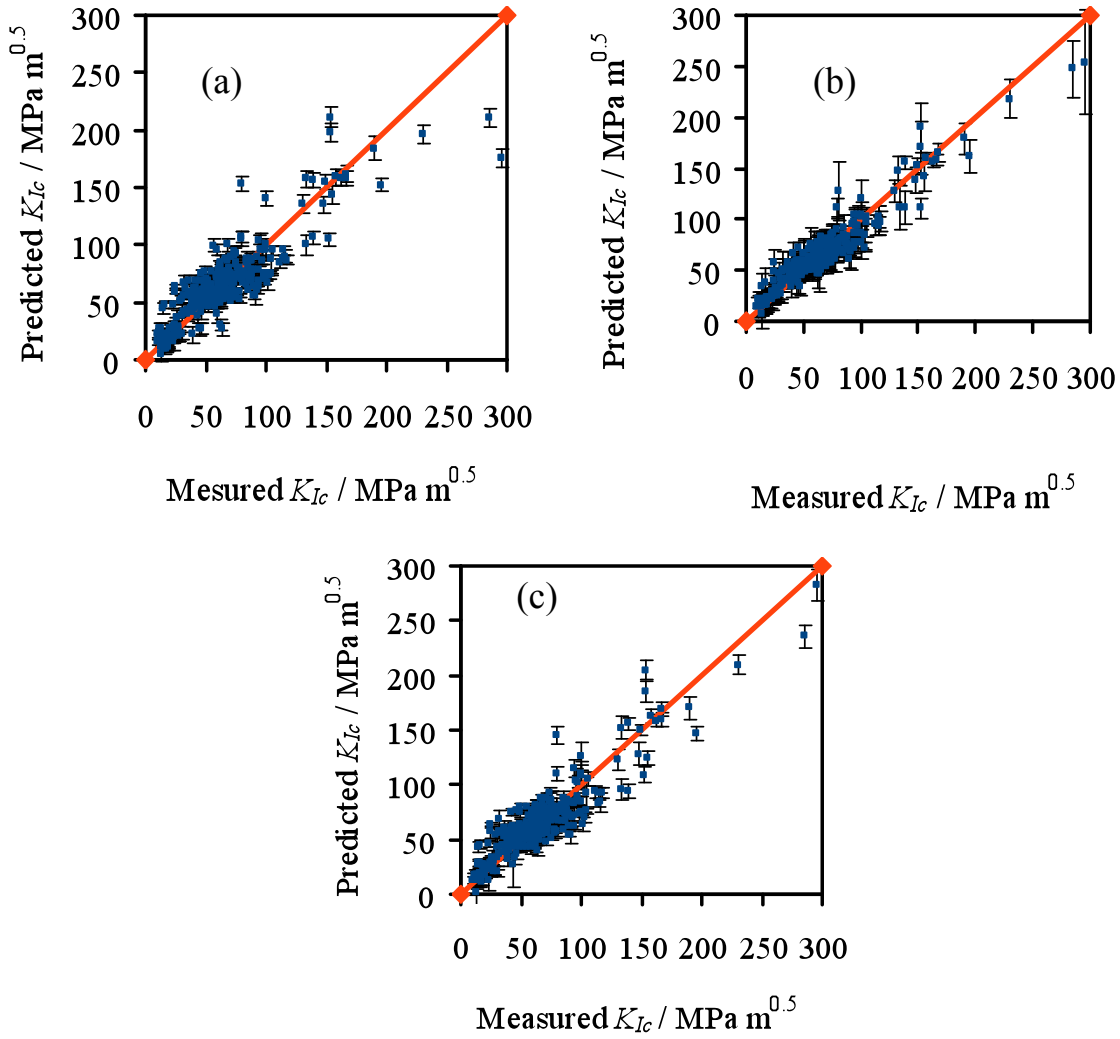
Figure 6.9a-c: Predictions by three committee models, for the entire data set for the chemical composition, heat treatment and mechanical properties model, the inputs listed in table 6.3.
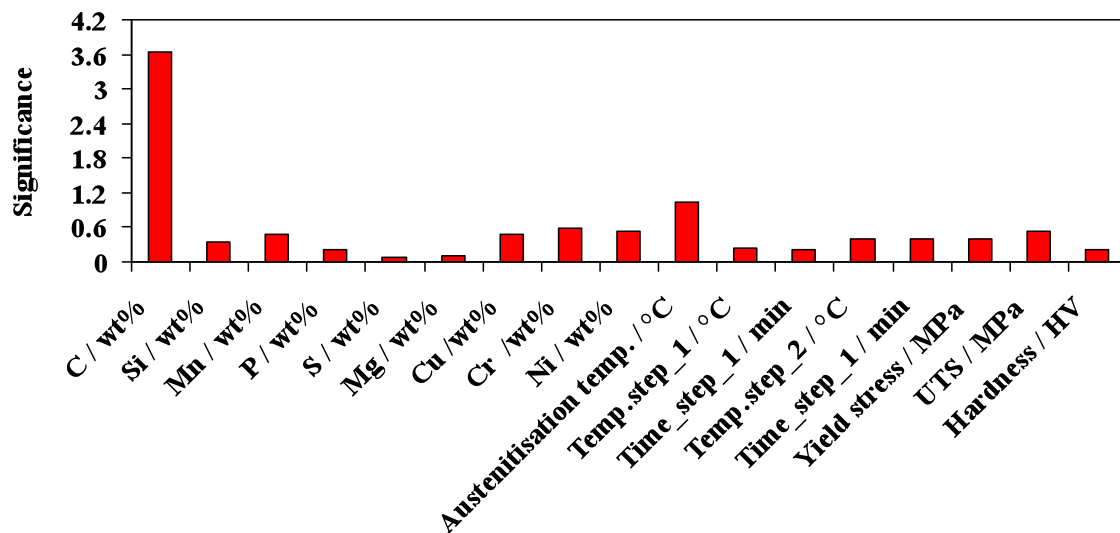
Figure 6.10: Significance for the committee of the chemical composition, heat treatment and mechanical properties model, the inputs listed in table 6.3.

6.4 Predictive ability

The general performance of the model can be tested by predicting on unseen data. Two of the three models were found to generalize badly and the last model was capable of making useful prediction of unseen compositions, figure 6.11, 6.12 and 6.13. These were grouped into those within the range of data used for training and those outside the range.

6.4.1 Predictive ability of the model mechanical properties

Figure 6.11 shows the prediction of the model to compare with the unseen data, the mechanical properties used are shown in table 6.7. Each value is within the ranges shown in table 6.1.

Table 6.7: Mechanical properties for the steels used to test predictive capability model_2 mechanical properties (Appendix A).

Yield stress / MPa	UTS / MPa	EL / %
1130.71	1430.71	0.39
800	1050	15
900	1170	11
1308	1600	2.2
1556	1670	15.5
1470	1900	11.8
507	587	0.93
1103	1144	1.05
1675	1854	13.3
1660	1765	16
900	1041	6.7
1280	1570	3.8
2593	2670	5.8
704.93	1054.71	10.8
737.22	1087	10.67
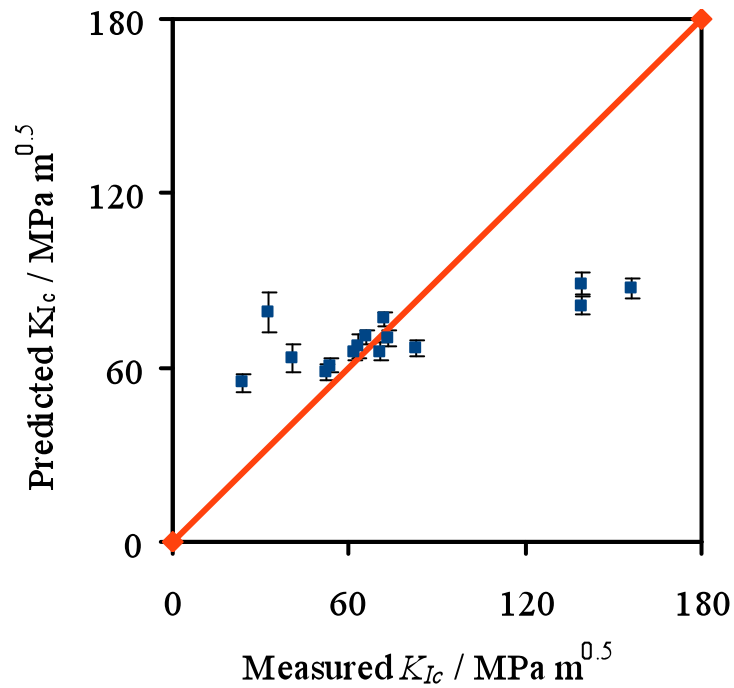
Figure 6.11: Predictions of plane strain fracture toughness in MPa m$^{0.5}$ against the actual plane strain fracture toughness in MPa m$^{0.5}$ for committee model _2 mechanical properties.

6.4.2 Predictive ability of the model chemical composition

Figure 6.12 shows the prediction of the model to compare with the unseen data, the chemical compositions used are shown in table 6.8. Each value is within the ranges shown in table 6.2.

Table 6.8: Chemical composition in wt% for the steels used to test predictive capability (Appendix A).

C	Si	Mn	P	S	Mg	Cu	Cr	Ni
3.59	2.52	0.28	0.04	0.01	0.04	0.43	0	0
3.7	2.5	0.28	0	0	0	0.8	0	2
3.48	2.31	0.15	0.03	0.01	0.04	0.45	0	0.45
3.5	2.47	0.38	0.02	0.01	0.04	0.35	0.5	1.57
3.45	2.48	0.4	0.01	0.01	0.15	0	0	1.5
3.4	2.41	0.15	0.02	0.02	0.06	0	0	0
0.11	0.29	1.39	0.01	0.02	0	0	3.87	0
0.39	1.06	0.32	0.02	0	0	0	4.91	0.11
0.89	0.2	0.26	0.03	0	0	0	3.91	0
1.02	2.45	0.4	0.01	0.01	0	0	0	0.2
0.82	0.18	0.25	0.02	0.01	0	0	4.15	0
0.22	0.15	0.4	0.01	0.01	0	0	0.39	0.88
0.4	0.25	0.7	0.01	0	0	0.06	0.8	1.9
0.14	0.04	0.12	0.01	0	0	0	1.92	10.26
0.16	0.05	0.16	0	0	0	0	1.97	10.05
0.8	0.75	1	0	0	0	0	1	0.5
0.25	0.8	1	0	0	0	0	0.5	1.25

0.53   0.29   0.76   0.01   0   0   0.07   0.8   1.75
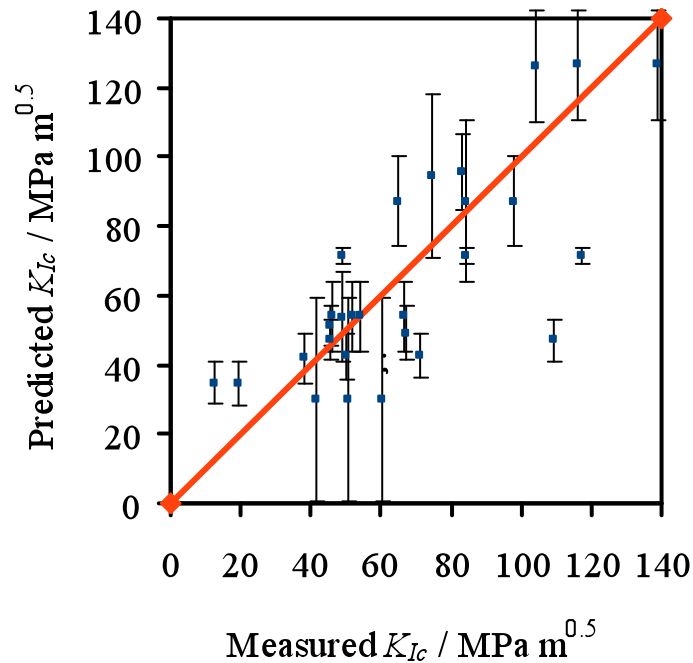
Figure 6.12: Predictions of plane strain fracture toughness in MPa m$^{0.5}$ against the measured plane strain fracture toughness in MPa m$^{0.5}$ for committee model chemical composition.

6.4.3 Predictive ability of the model chemical composition, heat treatment and mechanical properties

Figure 6.13 shows the prediction of plane stain fracture toughness for different types of steels and austempered ductile iron within the range of the data in table 6.3. The input data are in table 6.9.

Table 6.9: The input data for the steels used to test predictive capability in model_2, the chemical composition in wt% (Appendix A).

C	Si	Mn	P	S	Mg	Cu	Cr	Ni
0.4	2	0.7	0.04	0.04	0	0	0.8	1.83
0.78	0.36	0.44	0.01	0	0	0	3.9	0
0.17	0.24	0.5	0.01	0.01	0	0.05	1.93	1.28
0.8	0.75	1	0	0	0	0	1	0.5
0.46	0.27	0.65	0	0	1.25	0	0.6	1
0.8	0.75	1	0	0	0	0	1	0.5
0.29	0.2	0.5	0.02	0.01	0	0	1.1	4
0.29	0	0.01	0.01	0.01	0	0.02	0.01	0.01
0.3	0	0.9	0.01	0.01	0	0.02	0.01	0.01
0.26	0	1.47	0.01	0.01	0	0.02	0.01	0.01
3.59	2.52	0.28	0.04	0.01	0.04	0.43	0	0
0.4	0.19	0.71	0.01	0	0	0	0.76	1.72
1.02	2.45	0.4	0.01	0.01	0	0	0	0.2
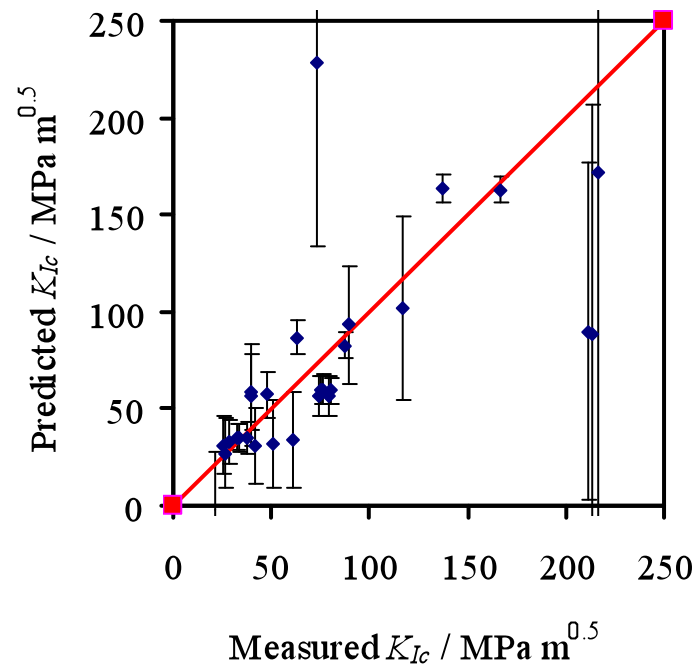
Figure 6.13: Predictions of plane strain fracture toughness in MPa m$^{0.5}$ against the measured plane strain fracture toughness in MPa m$^{0.5}$ for committee model_2 chemical composition, heat treatment and mechanical properties.

6.4.3.1 The predictions for super-bainite alloy PP1

Figure 6.14 shows the predictive ability for model_2. The input data is for super-bainite for alloy PP1 and the same alloy after tempering. The chemical composition and heat treatment was presented in chapter three. Table 6.10 shows the input data.

Table 6.10: the input data for the steel PP1 used to test predictive capability in model_2, the chemical composition in wt%.

C	Si	Mn	P	S	Mg	Cu	Cr	Ni	T_a / °C	T_t / °C	t_t / minutes
0.97	1.43	1.59	0	0	0	0	0.26	0.04	1000	200	14400

Yield stress / MPa	UTS / MPa	Hardness / HV	K_{Ic} / MPa m^0.5 Measured	K_{Ic} / MPa m^0.5 Predicted	Error bar
1383	1622	725	30	53.96864	134.278
1571	1767	725	32.3	58.26289	121.521
1519	1819	700	27.32	-335.6149	3555.12
1515	1815	689	22.9	62.66182	250.71
1326	1626	663	22.99	48.22984	294.381
1252.6	1552.6	626	20	40.96894	322.317
1306.8	1606.8	594	22.14	31.48918	353.426
921.8	1221.8	419	13.81	-1.294846	461.105
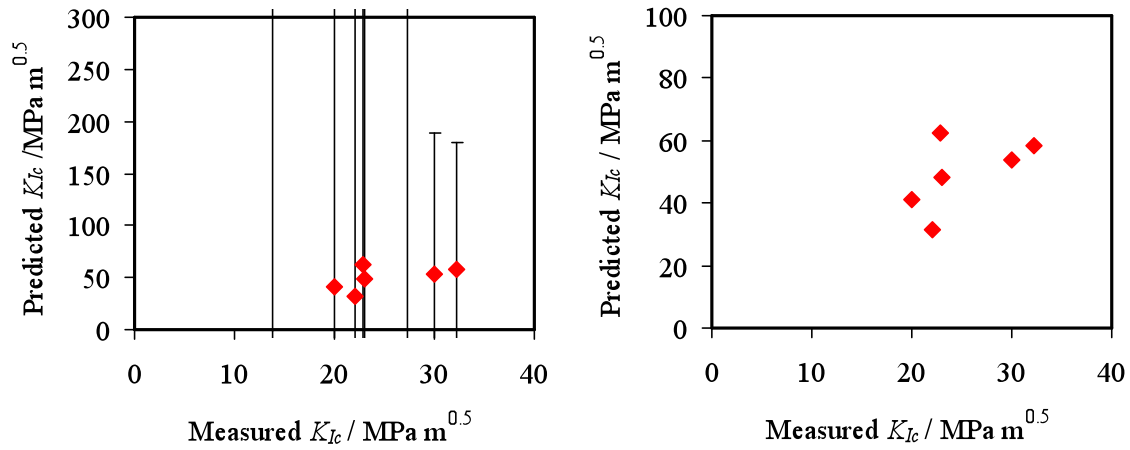
Figure 6.14: Predictions of plane strain fracture toughness in MPa m^{0.5} against the measured plane strain fracture toughness in MPa m^{0.5} for committee model_2 to the data out of the range (experiments carried out in this work) (a) with error bar (b) without error bar.

It can be seen that the model is weak in the prediction of K_{Ic} values for the alloy PP1. In the best chemical composition, heat treatment and mechanical properties model, the value of the root mean squared error is equal to 26.4 and the perceived error is 276.22. There is a huge difference between these two values. This difference is due to noise and uncertainty because the actual data do not contain data for tempered super-bainite.

6.5 Comparing the performance of the main three models

Predictions with the best three neural network models were made and the corresponding R_{test} and E_{bar} for these three models are given in Table 6.11. For the ideal case the two values R_{test} and E_{bar} should be equal as it was explained in chapter two. There is a high difference between the value of R_{test} and E_{bar} for the mechanical properties model for both seen and unseen data. The chemical composition model has also a high

difference between R_{test} and E_{bar} for both seen and unseen data. The weakness of this model is that a single fracture toughness value is predicted for steel with a certain chemical composition. In actual applications, fracture toughness varies with heat treatment for the same steel.

There is a low difference between R_{test} and E_{bar} for seen data to the last model (chemical, heat treatment and mechanical properties) but still has a high difference between R_{test} and E_{bar} for unseen data. The weakness of this model comes from the assumptions which were taken previously in section 6.3.1.3 to complete the missing data concerning yield stress, ultimate tensile stress and austenitisation temperature. The usefulness of the uncertainty E_{bar} is the warning it might give to the model.

From this comparison, the last model can be used to predict plane strain fracture toughness better than the other two models. However, the last model needs more modifications, especially with the predictions of the alloy PP1, due to the poor predictive ability for tempered super bainite as explained previously.

Table 6.11: comprising of the performance of three basic models.

Model		R_{test}	E_{bar}
Mechanical properties	Seen data	24.11	7.6
	Unseen data	25.655	8.111
Chemical composition	Seen data	31.94	9.74
	Unseen data	21.2	12.21
Chemical +heat +mechanical	Seen data	10.82	8.06
	Unseen data	47.09	32.37

6.6 Modified model chemical composition, heat treatment and mechanical properties

A modified new model was built with the chemical composition, heat treatment and mechanical properties in an effort to make the model more able to predict K_{Ic} accurately. The ultimate tensile stress was removed from the input data and some of the experimental results explained in chapter four were added as new data points. These new data points included four K_{Ic} values for tempered nanostructure bainite in alloy PP1. In total, there were 443 data points for the modified model while the previous model has a total of 394.

A total of 100 networks were trained by the half of the data and tested with another half, the complexity shown in figure 6.15a, as was explained in chapter two. The test error has a minimum value with range nine hidden units figure 6.15b. The LPE displays a high degree of scatter; with a rough peak in eight hidden units, figure 6.15c. More reliable results were obtained by combining models into a committee. In this case, the optimum committee was found to have fifteen sub models, figure 6.15d with the minimum test error.

The modified model has the root mean square error and perceived error as shown in table 6.12. Figure 6.16 shows prediction of the modified model for the entire data.

Figure 6.17 shows the neural network perceived significance, σ_w, for each input variable. In particular, note the committee opinions on the significance of carbon, copper, silicon, manganese and nickel. For heat treatment, temperature and time of tempering and austenitizing temperature have high significance and the hardness has higher significance than the yield stress. These are discussed in more details later.

Table 6.12: The performance of the model using the root mean square and perceived error for the chemical composition, heat treatment and mechanical properties modified model.

The modified model	Root mean squared error	Perceived error
Seen data	8.18	6.4

Comparison between the performance of the chemical, heat treatment and mechanical properties of the original and the modified models shows that the difference between the root mean squared error and perceived error for the modified model is less than the same difference for the original model for the seen data.
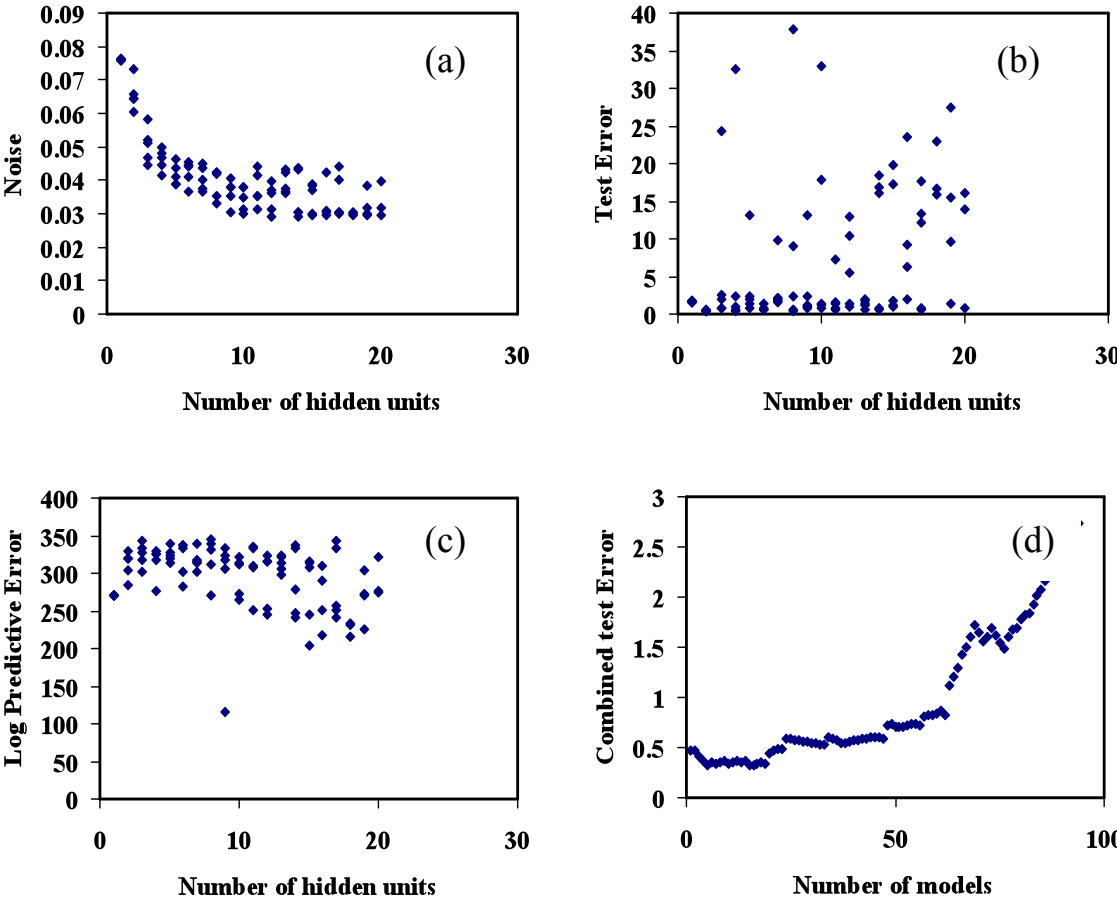
Figure 6.15: Optimum model training reports: (a) Perceived level of noise for training, (b) the error between the models and the test data, (c) log predictive error for increasing model complexity, (d) combined test error for different sizes of committee.
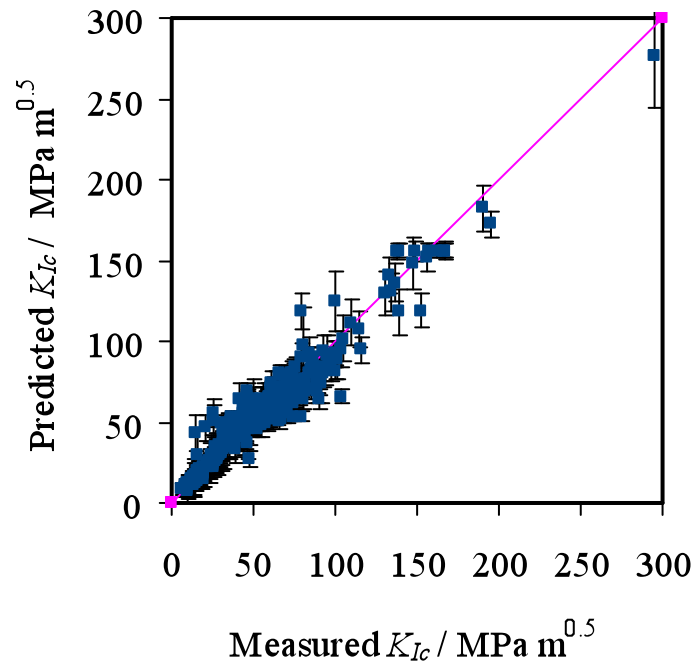
Figure 6.16: Predictions by the committee model, for the entire data set for the chemical composition, heat treatment and mechanical properties optimized model.
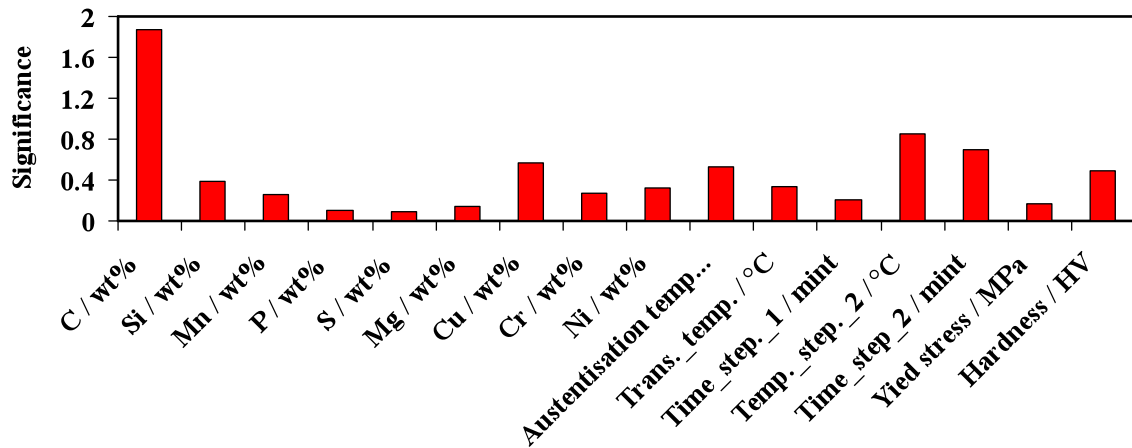
Figure 6.17: **Perceived significance for the committee of the optimized model.**

6.7 Model predictions

The toughness of steels depends on many variables as stated before. Therefore, it is not possible to predict the plane strain fracture toughness with any reliability. It is well known that all materials have defects which appear as small cracks and grow during service leading to catastrophic fractures.

The plane strain fracture toughness tests give critical values which can be used directly in engineering design. The test involves the initiation and propagation of a crack by fatigue cycling at the tip of crack length for a certain length. These tests are time consuming and costly.

Attempts were carried out for improving the mechanical properties of super bainite and investigating these types of steels. A neural network model was therefore created to cover a very large range of steels; its purpose was to estimate the plane strain fracture toughness as a function of many variables as indicated above. Calculations using this model are shown in figures 6.18- 6.25.

The input compositions for all the predictions made are shown in Table 6.12, estimates were not made for all alloys in the database. This is the same steel which was used in chapter four for predictions of the hardness model.

Table 6.12: The inputs for the alloy, the chemical composition in wt% [71].

C	Si	Mn	P	S	Mg	Cu	Cr	Ni
0.98	1.46	1.89	0	0	0	0	1.26	0

Austenitisation temperature / °C	Temp. step1 / °C	Time step1 / mint	Temp. step2 / °C	Time step2 / mint	Yield Stress / MPa	Hardness / HV
1000	200	14400	30	30	1500	619

6.7.1 Effect of chemical composition on plane strain fracture toughness

The effect of carbon content on K_{Ic} was explained previously and is as shown in figure 6.18. The trend is an increase in K_{Ic} with increasing carbon content. There is a change in error bars, starting with a relatively high error bar at about 0.5 wt% carbon content and then decreasing to a minimum at about 0.9 wt% carbon content and then increasing again up to 1.2 wt% carbon content. From iron carbon equilibrium phase diagram, carbon dissolve completely in the austenite phase between 0.6-1.5 wt% carbon content at 1000 °C and the increase of carbon content in the austenite phase increases the stability of that phase [28]. The volume

fraction of bainite, as calculated according to eq. 2.1, will decrease with increasing carbon content and the volume fraction of the austenite stable phase will increase. This austenite is supposed to be a tough phase as explained before. After 1.2 carbon content, the toughness might decrease because the brittle cementite phase will appear with austenite. In the region between 1-1.2 C wt%, the prediction shows high error bars and sparse and noisy data that give an indication of a probable drop in toughness.
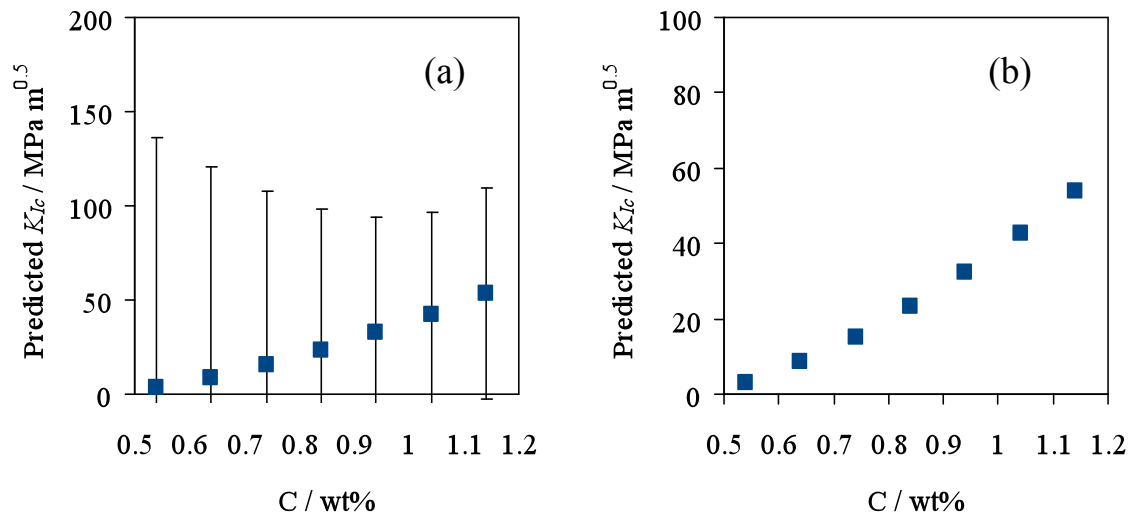
Figure 6.18: Predictions of plane strain fracture toughness in MPa m$^{0.5}$ against carbon content in wt%, (a) with error bars, (b) general trend.

Figure 6.19 shows the effect of silicon on the KIc. The KIc increases with an increase in the silicon content from approximately 0.6 to 2.6 wt%. Silicon hinders the formation of the cementite phase, leading to an increase in K_{Ic} [96]. Silicon is a ferrite stabilizer; it slows the kinetics of transformation to bainite [28, 97] which means more tough austenite will form.
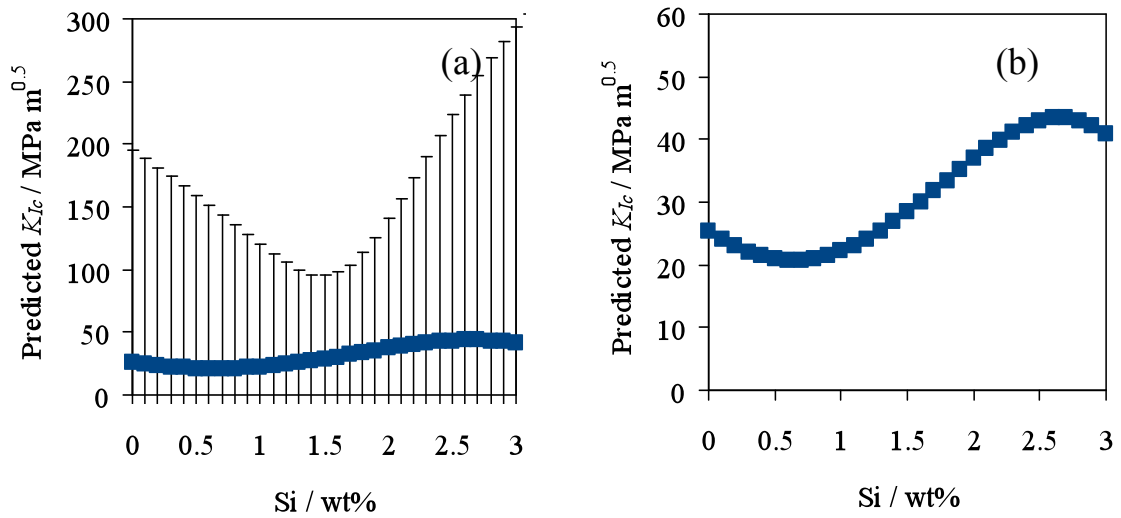
Figure 6.19: Predictions of plane strain fracture toughness in MPa m$^{0.5}$ against silicon content in wt%, (a) with error bars, (b) general trend.

Figure 6.20 shows that K_{Ic} decreases as the chromium content increases. Chromium leads to solid solution hardening which may make the ferrite more stable than the austenite. The error bars look almost constant, i.e. they come from an uncontrolled variables noise [28].
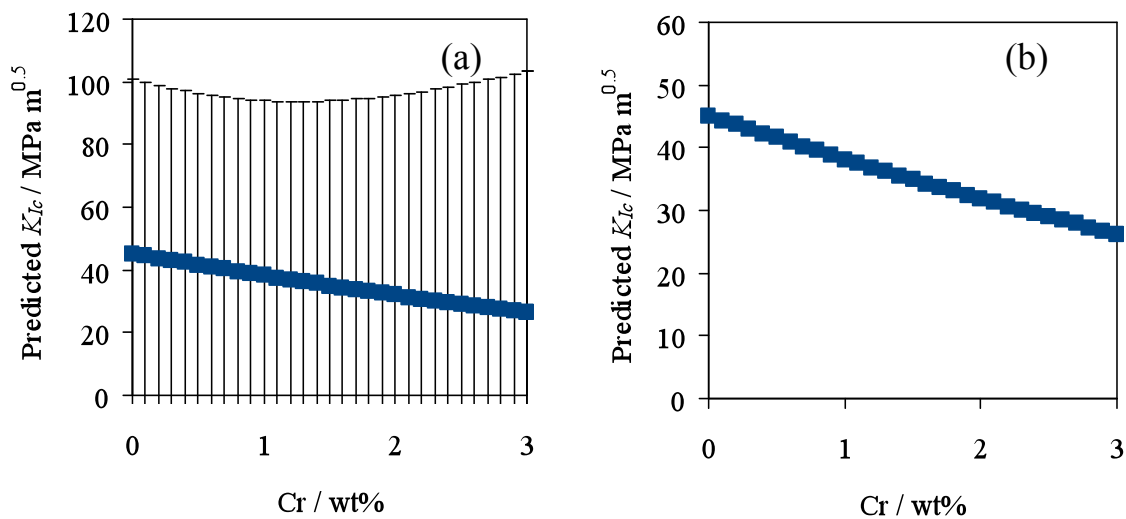
Figure 6.20: Predictions of plane strain fracture toughness in MPa m^0.5 against chromium content in wt%, (a) with error bars, (b) general trend.

Figure 6.21 shows that K_{Ic} has a minimum value at a copper content of 1 wt%. Figure 6.22 shows that the minimum value of K_{Ic} is at a nickel content of about 2 wt%. These two elements may not influence much the microstructure and the toughness of super bainite.

In general, alloying elements (except carbon) do not affect the plane strain fracture toughness that much and only the carbon content has a significant effect.
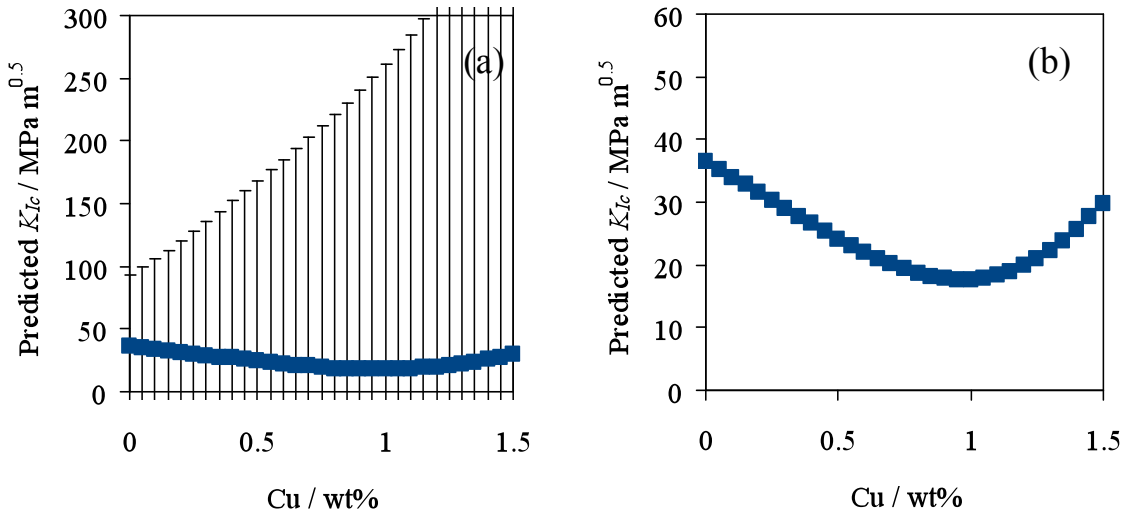
Figure 6.21: Predictions of plane strain fracture toughness in MPa m$^{0.5}$ against copper content in wt%, (a) with error bars, (b) general trend.
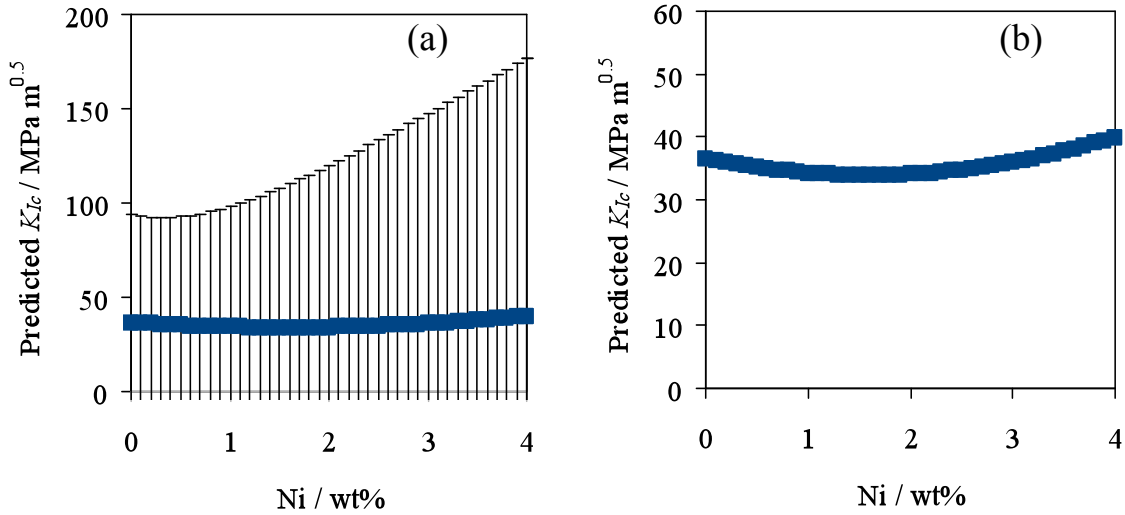
Figure 6.22: Predictions of plane strain fracture toughness in MPa m$^{0.5}$ against nickel content in wt%, (a) with error bars, (b) general trend.

6.7.2 Effect of austenitisation temperature on plane strain fracture toughness

Figure 6.23 shows that K_{Ic} increases as the austenitisation temperature increases. The error bars show increasing heights because of noise in the data since some austenitisation temperatures were approximated as it was explained in the input data.
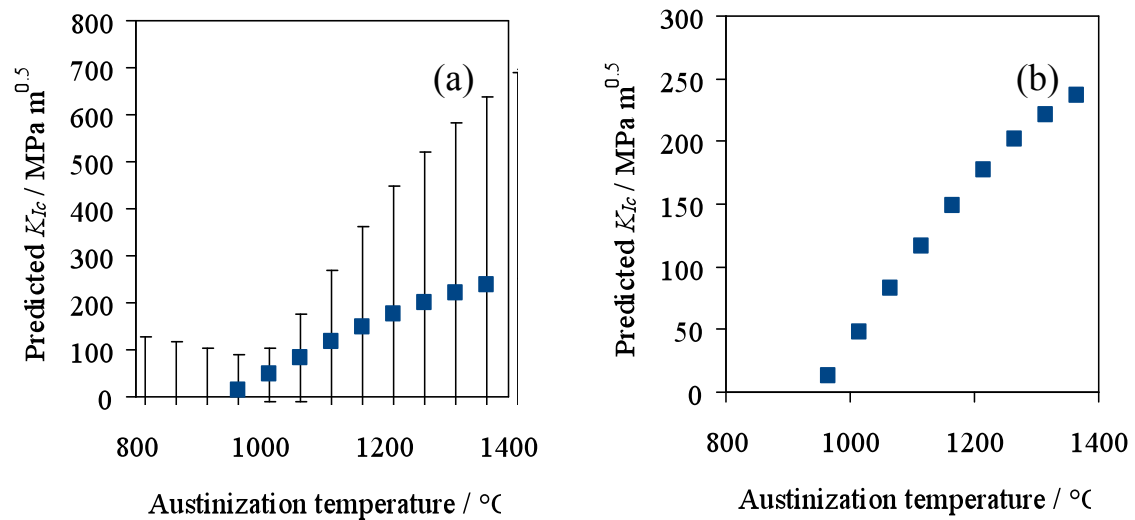
Figure 6.23: Predictions of plane strain fracture toughness in MPa m^0.5 against austenitisation temperature / °C, (a) with error bars, (b) general trend.

6.7.3 Effect of mechanical properties on plane strain fracture toughness

Figure 6.24 shows a slight decrease in plane strain fracture toughness as the yield stress increases. Figure 6.25 shows a decrease in K_{Ic} with an increase in hardness.
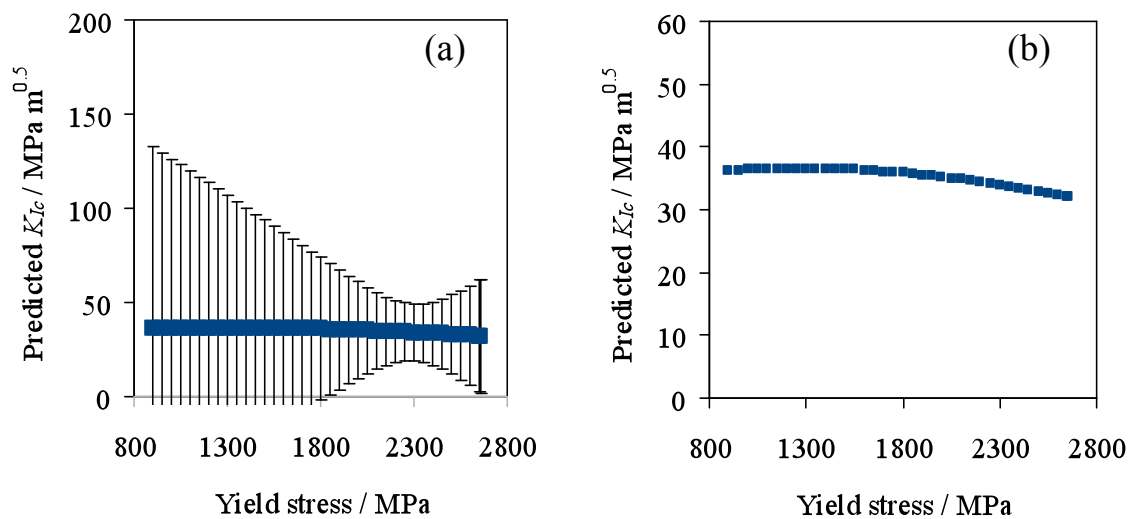
Figure 6.24: Predictions of plane strain fracture toughness in MPa m$^{0.5}$ against yield stress in MPa for committee, (a) with error bars, (b) general trend.
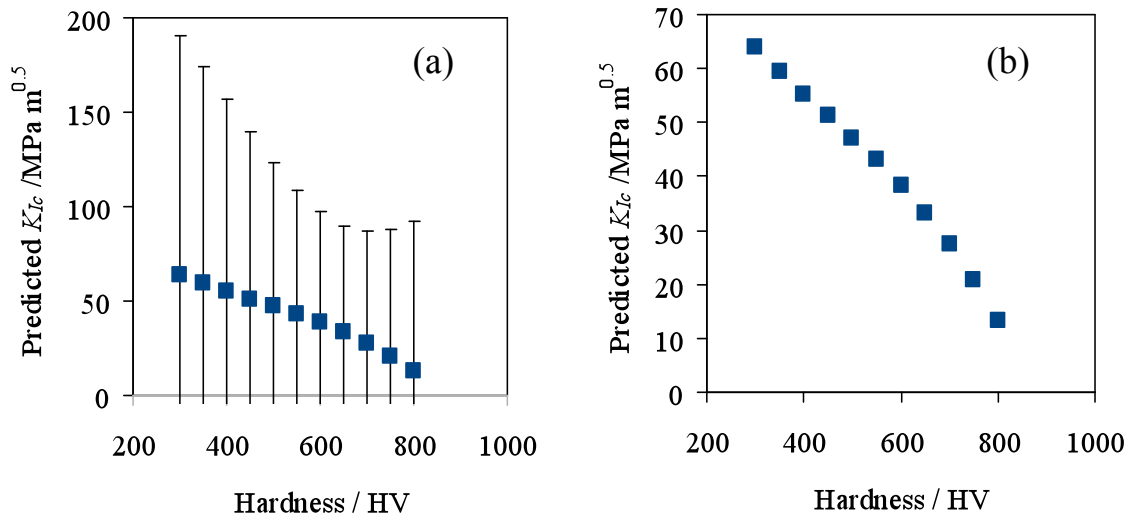
Figure 6.25: Predictions of plane strain fracture toughness in MPa m$^{0.5}$ against Vicker hardness in committee, (a) with error bars, (b) general trend.

6.7.4 The combined effects

The combined effect of carbon and silicon on the plane strain fracture toughness for the alloy the details of this alloy was listed in table 6.12, is shown in figure 6.26a. The figure shows that the carbon content has a significant effect with an increase in the K_{Ic} with increasing C content, while the effect of Si content is minimal. Figure 6.26b shows that the height of error bars decreases with the increase in silicon content and the minimum value of error bars is between approximately 0.9-1.2 wt% carbon content and 1.4-1.6 wt% silicon content.

Figure 6.27a shows the combined effect of carbon and manganese content. Increasing the carbon content and decreasing the manganese content increase the K_{Ic}. Figure 6.27b shows that the height of error bars

is a minimum in the area between 1-1.2 wt% carbon content and 1.3-2 wt% manganese.

Figure 6.28a shows the combined effect of carbon and copper on the plane strain fracture toughness. It can be noticed that the effect of carbon content is more significant than the effect of copper. K_{Ic} increases with increasing carbon content and the height of error bars increases with increasing copper content as shown in figure 6.28b.

The increase of transformation temperature has more effect on the plane strain fracture toughness than the hardness. K_{Ic} increases as the transformation temperature increases as shown in figure 6.29a. When the transformation temperature increases, the bainite volume fraction will decrease and the tough austenite phase will increase [28]. Figure 6.29b shows the error bars for the combined effect of the transformation temperature and hardness. The least height of error bars lays in the area of high hardness 560-650 HV and relatively low transformation temperature 150-275 °C.
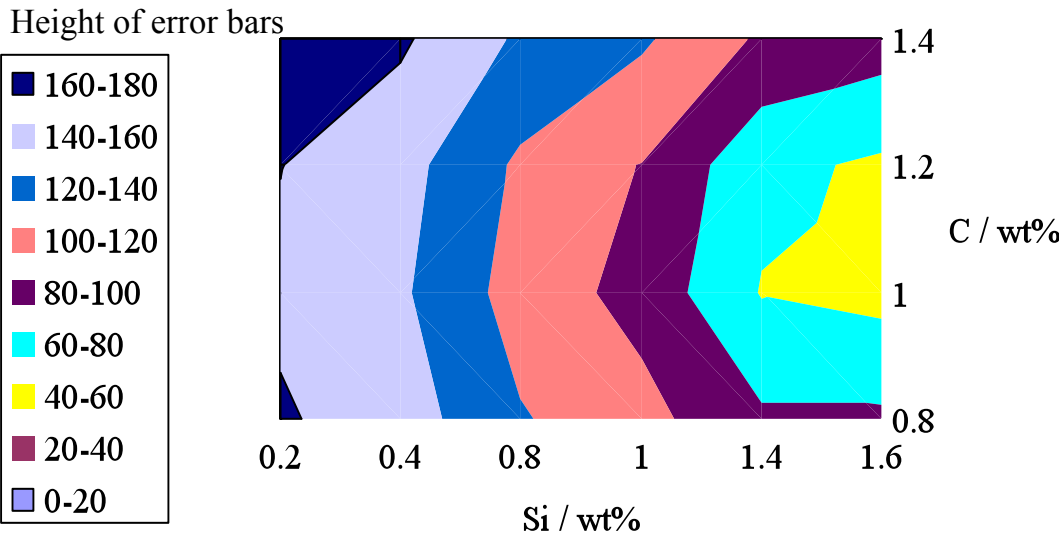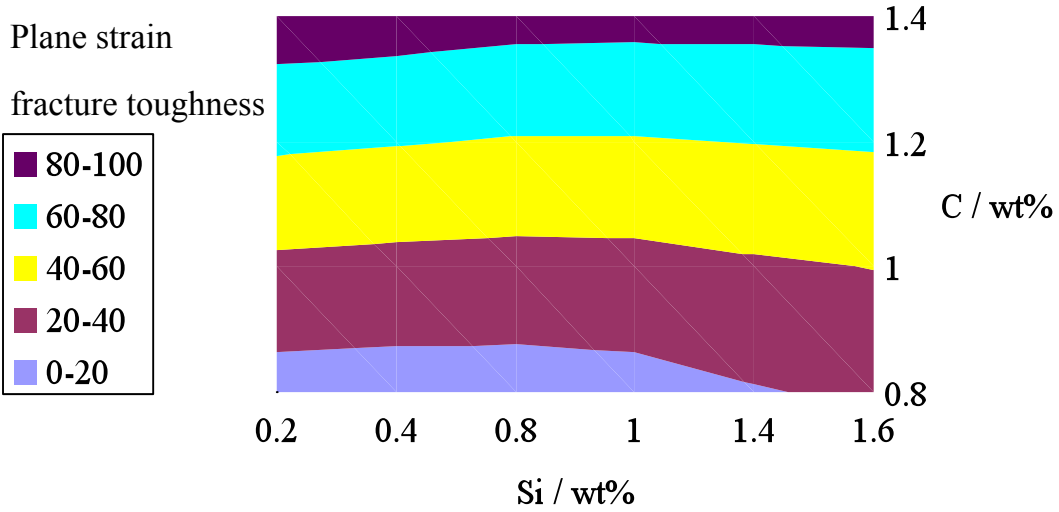
Figure 6.26: (a) Predictions of plane strain fracture toughness in MPa m$^{0.5}$ against carbon and silicon content. (b) The distribution of the error bars in the committee.
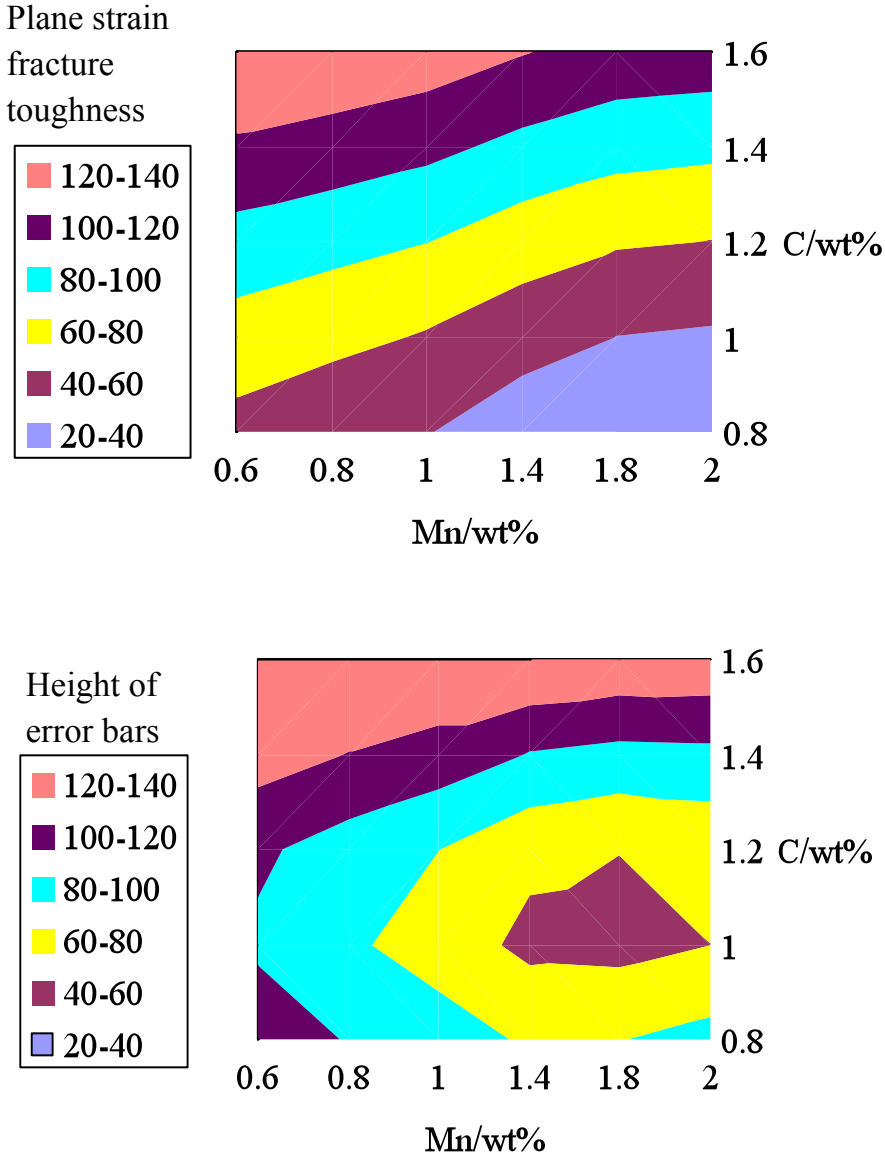
Figure 6.27: (a) Predictions of plane strain fracture toughness in MPa m$^{0.5}$ against carbon and manganese content. (b) The distribution of the error bars in the committee.
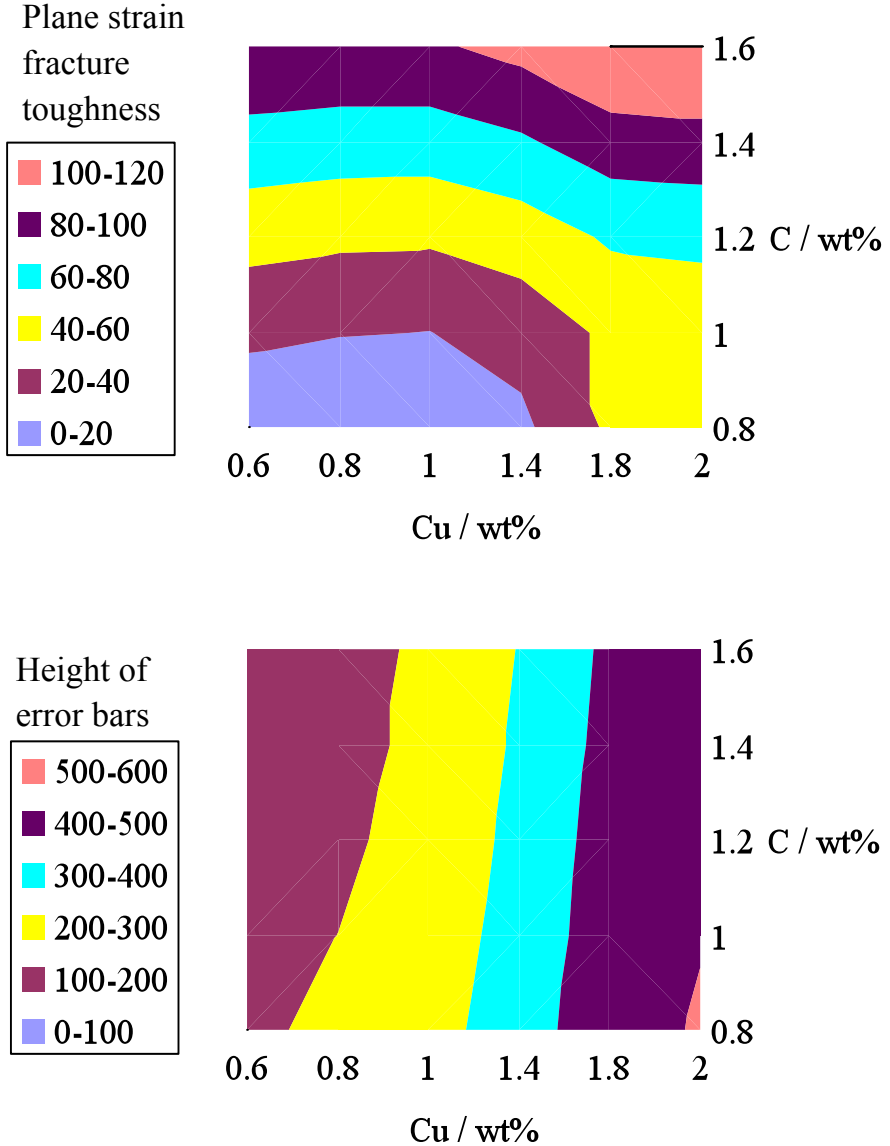
Figure 6.28: (a) Predictions of plane strain fracture toughness in MPa m$^{0.5}$ against carbon and copper content. (b) The distribution of the error bars in the committee.
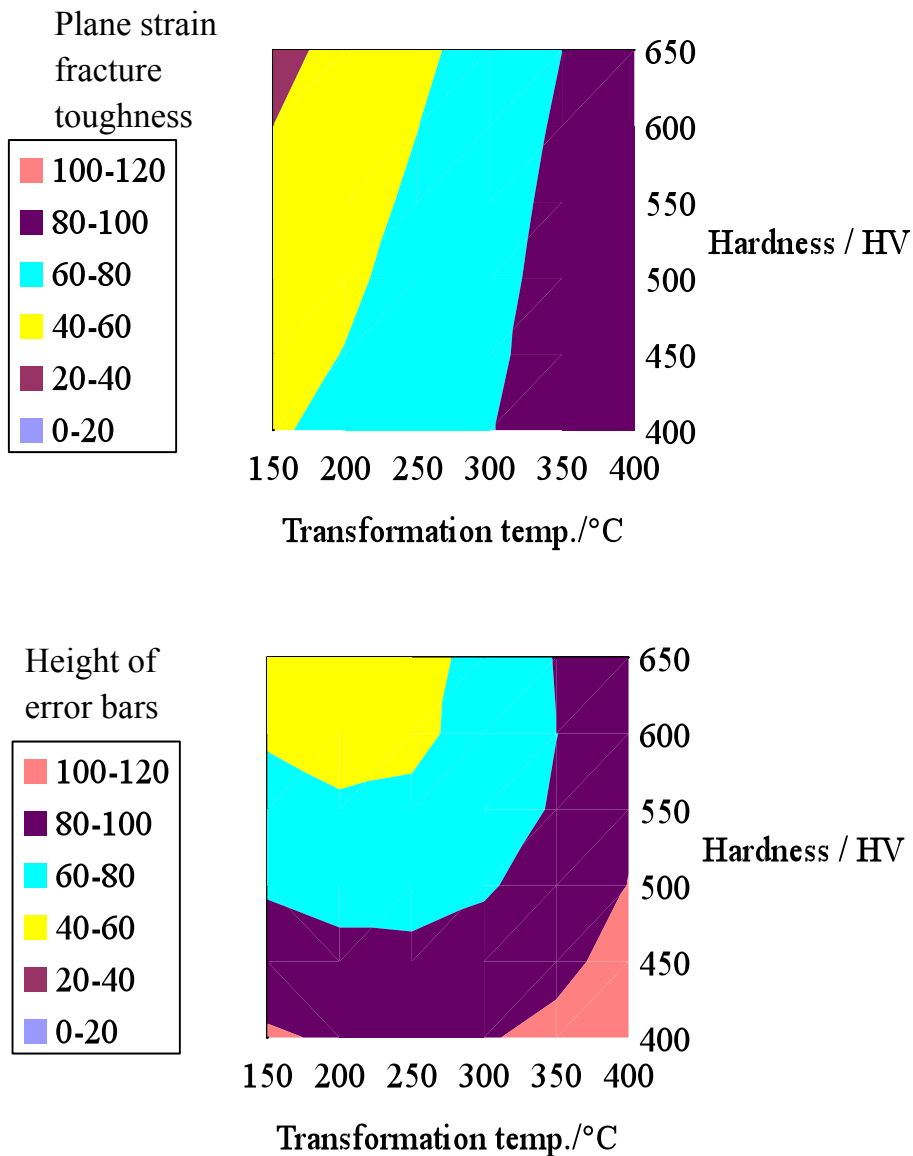
Figure 6.29: **(a) Predictions of plane strain fracture toughness in MPa m$^{0.5}$ against hardness in HV and transformation temperature in °C (b) The distribution of the error bars in the committee.**

6.8 Predictive ability

The general performance of the model can be tested by predicting on unseen data. Table 6.13 has the values of the unseen data within the range of the modified model. Figure 6.30 shows the predicted plane strain fracture toughness against the actual values [98-101].

Table 6.13: The unseen data used for testing the predictive ability of the model, the chemical composition in wt%.

Ref	C	Si	Mn	P	S	Mg	Cu	Cr	Ni
[98]	0.3	0	0.6	0.01	0.01	0	0	0	0
[98]	0.41	0	0.6	0.01	0.01	0	0	0	0
[98]	0.41	0	0.6	0.01	0.01	0	0	0	0
[98]	0.25	0.8	1	0	0	0	0	0.5	1.25
[98]	0.25	2	1	0	0	0	0	0.5	1.25
[98]	0.25	0.8	1	0	0	0	0	0.5	1.25
[98]	0.4	0.23	0.7	0.04	0.04	0	0	0.8	1.83
[98]	0.4	2	0.7	0.04	0.04	0	0	0.8	1.83
[98]	0.42	1.59	0.76	0.01	0	0	0	0.76	1.76
[99]	0.78	0.36	0.44	0.01	0	0	0	3.9	0
[100]	0.8	0.75	1	0	0	0	0	1	0.5
[101]	0.29	0.2	0.5	0.02	0.01	0	0	1.1	4
[102]	0.17	0.24	0.5	0.01	0.01	0	0.05	1.93	1.28
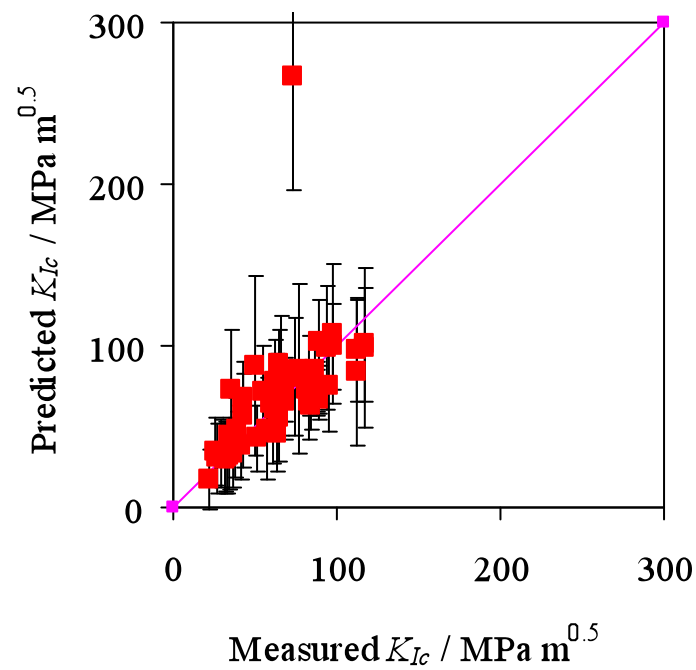
Figure 6.30: Predictions of plane strain fracture toughness in MPa m$^{0.5}$ against the measured plane strain fracture toughness in MPa m$^{0.5}$ for the modified model of chemical composition, heat treatment and mechanical properties.

Other data concerning alloys with super bainite were collected and tested by the modified model. Table 6.14 shows the values of the input variables, the output and the measured values for the plane strain fracture toughness. Figure 6.31 shows the relation between the predicted and measured values.

Table 6.14: The performance of the model is in terms of the root mean square and perceived error for the chemical composition, heat treatment and mechanical properties modified model.

The modified model	Root mean squared error	Perceived error
For unseen data	29	25

Table 6.14: The input, output and predicted values with error bars of super bainite steels, the chemical composition in wt%.

C	Si	Mn	P	S	Mg	Cu	Cr	Ni	Austenitisation temp. / °C	Temp. step1 / °C	Time step1 / minutes
0.97	1.43	1.59	0	0	0	0	0.26	0.04	1000	200	14400
0.97	1.43	1.59	0	0	0	0	0.26	0.04	1000	200	14400
0.97	1.43	1.59	0	0	0	0	0.26	0.04	1000	200	14400
0.97	1.43	1.59	0	0	0	0	0.26	0.04	1000	200	14400
0.97	1.43	1.59	0	0	0	0	0.26	0.04	1000	200	14400
0.97	1.43	1.59	0	0	0	0	0.26	0.04	1000	200	14400
0.97	1.43	1.59	0	0	0	0	0.26	0.04	1000	200	14400
0.97	1.43	1.59	0	0	0	0	0.26	0.04	1000	200	14400
0.98	1.46	1.89	0	0	0	0	1.26	0	1000	200	14400
0.8	1.59	2	0	0	0	0	1	0	900	200	5760
0.8	1.59	2	0	0	0	0	1	0	900	250	960
0.8	1.59	2	0	0	0	0	1	0	900	300	360

0.78	1.49	1.95	0	0	0	0	0.97	0	1000	200	14400
0.78	1.49	1.95	0	0	0	0	0.97	0	1000	250	14400
0.78	1.49	1.95	0	0	0	0	0.97	0	1000	300	14400
0.79	1.56	1.98	0	0	0	0	1.01	0	900	200	5760
0.79	1.56	1.98	0	0	0	0	1.01	0	900	250	960
0.79	1.56	1.98	0	0	0	0	1.01	0	900	300	360

Table 6.14 (continued): The input, output and predicted values with error bars of super bainite steels, the chemical composition in wt%.

Temp. step2 / °C	Time step2 / minutes	Yield Stress / MPa	Hardness / HV	Predicted K_{Ic} / MPa m$^{0.5}$	Error bars	Measured K_{Ic} / MPa m$^{0.5}$
30	30	1383	725	36	61	30
30	30	1571	725	36	51	32.3
300	360	1519	700	27	9	27.32
300	43200	1515.8	689	22	11	22.9
400	480	1326	663	19	8.5	22.99
450	360	1252.6	626	18.7	8.5	20
500	360	1306.8	594	18.5	15	22.14
606	360	921.8	419	15	10	13.81
30	30	1500	620	36.4	57	30
30	30	1400	500	14	46	32
30	30	1500	589	31.5	39	38

30	30	1300	660	36.6	50	45
30	30	1400	500	26	100	32
30	30	1350	565	31.9	104	35
30	30	1300	650	38	119	50
30	30	1400	466.67	15.9	47.6	32
30	30	1350	450	37.6	36.4	35
30	30	1300	433.33	41.77	40.9	50
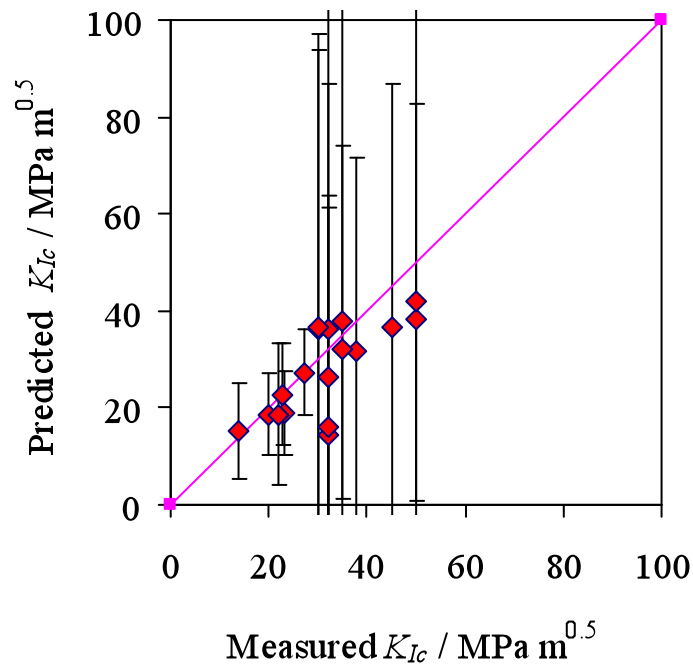
Figure 6.31: Predictions of plane strain fracture toughness in MPa m$^{0.5}$ against the measured plane strain fracture toughness in MPa m$^{0.5}$ for the modified model, alloy PP1 and the alloys (B, C and D) [34, 103, 104].

6.9 The need for more data

The data are sparse and certain noise as stated before and a solution is needed for this point. It is important that experimental data are reported as fully as possible. In particular, the conclusion is unavoidable that the extent of K_{Ic} cannot be characterised by a single parameter.

It was found that the mechanical properties (yield stress, ultimate tensile stress and elongation) alone do not estimate plane strain fracture toughness correctly and more experiments should be added to the data.

The estimation of plane strain fracture toughness through the chemical composition model was found to be unpractical, because for the same chemical composition, different values of K_{Ic} can be obtained dependent on heat treatment and hence mechanical properties.

Few data for tempered super-bainite was added from experiments conducted in this work to the modified model to refine the estimation of the K_{Ic} values.

Further work includes the incorporation of new data into the training database and the incorporation of further physically significant inputs to test their significance. As the models become more refined, their ability to identify optimised alloys, such as bainitic steels, widens and hence their useful application in engineering improves.

Chapter 7

Experimental Results and Discussion

7.1   Introduction

This chapter describes the results of experimental work, detailed in chapter 3. The results are used to validate the models for hardness and fracture toughness.

7.2 The results of experiments related to the model of hardness

Different types of high carbon low alloy steels have been used in the experiments to select which of these alloys can be used in automobile parts. A quenching dilatometer was used to perform a variety of heat treatments. Vickers hardness tests were performed on the alloys shown in table 7.1.

Optical microscopy was used to examine the results of the heat treatments. Many of the heat treatments resulted in cracking, especially when the hardness was high.

7.2.2 MT-DATA

Thermodynamic calculations were carried out with MTDATA (Metallurgical and Thermochemical Databank) created by the National Physical Laboratory; this is a program that calculates chemical equilibrium and phases for a large number of elements in the system [105]. It was used to set the austenitisation temperatures; figures 7.1, 7.2, 7.3 and 7.4. Equilibrium was calculated between ferrite, austenite and cementite using STGE plus and SGTE_SUB databases, table 7.1.

Table 7.1: Critical temperatures for the four alloys

Alloy	Ferrite α	Cementite θ	Austenite γ
EE22	700	740	74 0
EE23	700	803	803
EE24	687	730	747
EE25	720	763	763
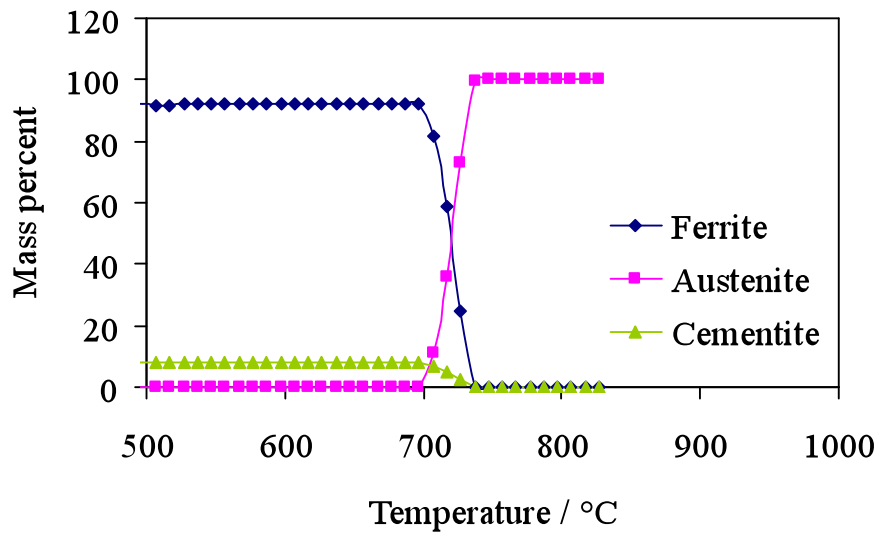
Figure 7.1: Equilibrium calculations for steel EE22.
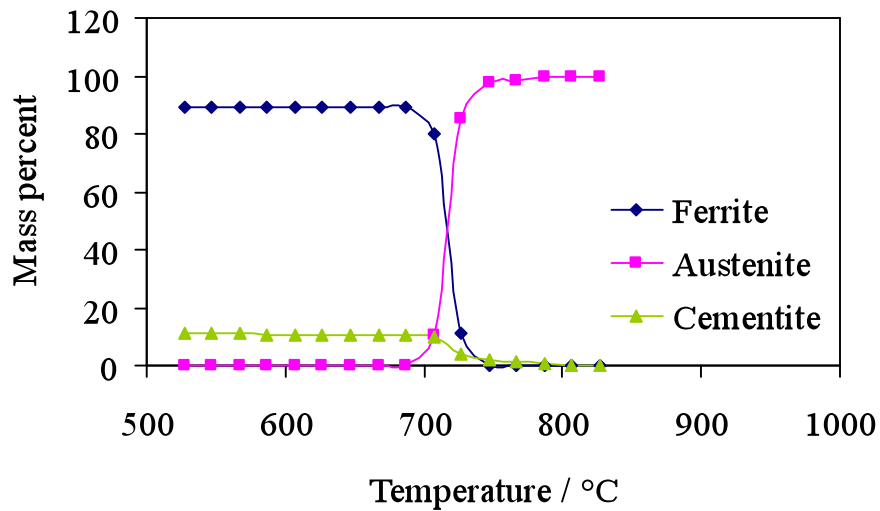
Figure 7.2: Equilibrium calculations for steel EE23.
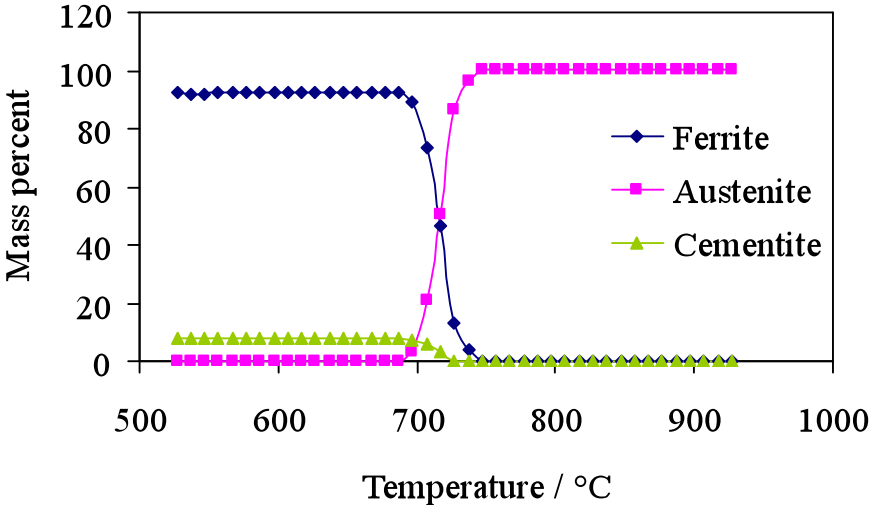
Figure 7.3: Equilibrium calculations for steel EE24.
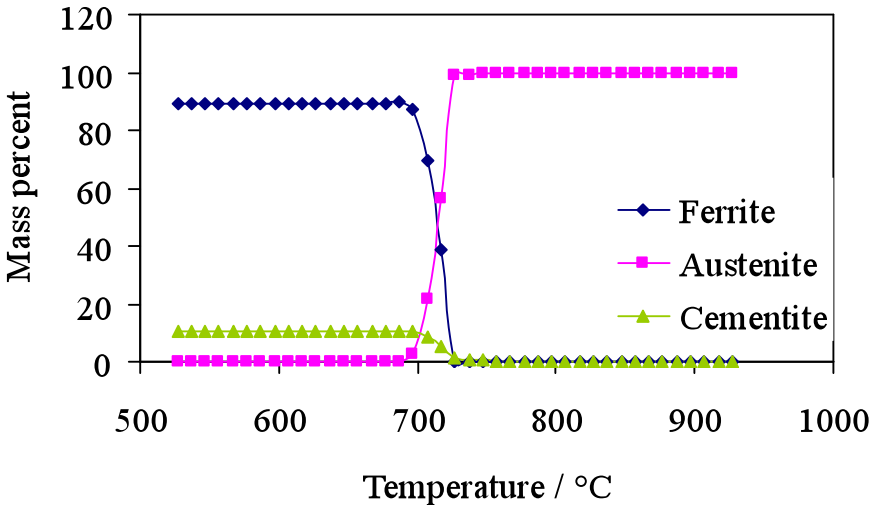
Figure 7.4: Equilibrium calculations for steel EE25.

7.2.3 Martensite-start temperature

The calculated and measured martensite start temperatures, M_s, for the alloys are shown in table 7.2. The measured readings were obtained by using the offset method on the results from the dilatometric graphs [106, 107]. The calculated M_s was obtained by using mucg-46 program [107, 108]. The measured and the calculated M_s have convergent values.

Table 7.2: The measured and calculated *Ms* for the four alloys.

Alloy	M_s measured / °C	M_s calculated / °C
EE22	221	221
EE23	162	130
EE24	263	276
EE25	175	194

7.2.4 Hardness results

The hardness for the alloys of the as-quenched microstructure is illustrated as a horizontal band on each diagram. These microstructures are mixtures of retained austenite and martensite that vary in their fractions. Hardness values and standard deviations of the four alloys are shown in table 7.3 for the samples directly quenched after austenitisation at 930 °C for 30 min. Table 7.4 shows the hardness for the samples austenitised at 930 °C and isothermally hardened at 160 °C for 10 min. and quenched to room temperature. Alloy EE25 is the hardest.

Table 7.3: Hardness and standard deviation with load 50kg for the four alloys.

Alloy	Hardness / HV	standard deviation
EE22	775	±32
EE23	784	±8
EE24	730	±8
EE25	828	±7

Table 7.4: The hardness for the austenitised at 930 °C and isothermally hardened at 160 °C for 10 min then quenched to room temperature with load 50 kg.

Alloy	Hardness / HV	standard deviation
EE22	754	±8
EE23	762	±6
EE24	704	±0
EE25	803	±12

7.2.5 Kinetics

The dilatometric results are shown in figure 7.5 (a, b and c), for three transformation temperatures in each of the three alloys EE22, EE24 and EE25 and in the range of bainite transformation. As the temperature decreases, the extent of transformation increases. The bainitic reaction takes place isothermally, starting with a period during which no transformation is detected, followed by an increasing rate of transformation to a maximum and then a gradual slowing down [17]. This is due to the incomplete reaction phenomenon [16].

The calculated transformation temperature and TTT diagrams for alloys are shown in figure 7.6 (a, b and c) which also contains experimental data for the time taken to initiate and cease transformation. The measured values for the achievement of dilatometric graph by using the offset method [106, 107] for transformation are in reasonable agreement with those calculated. Only alloy EE24 is not in full agreement with those calculated.
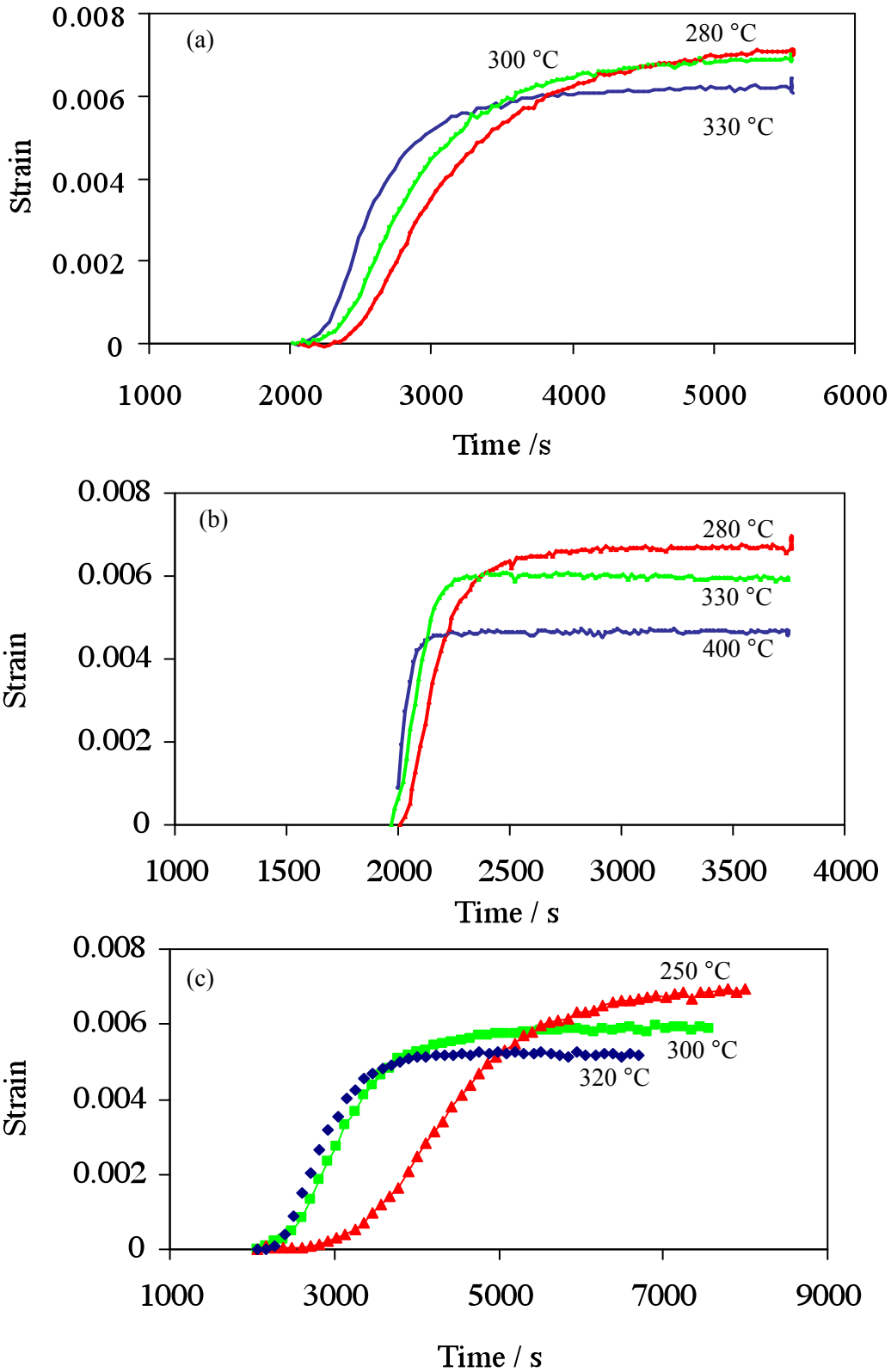
Figure 7.5: Isothermal reaction curve for the formation of bainite in alloy (a) EE22 (b) EE24 (c) EE25.
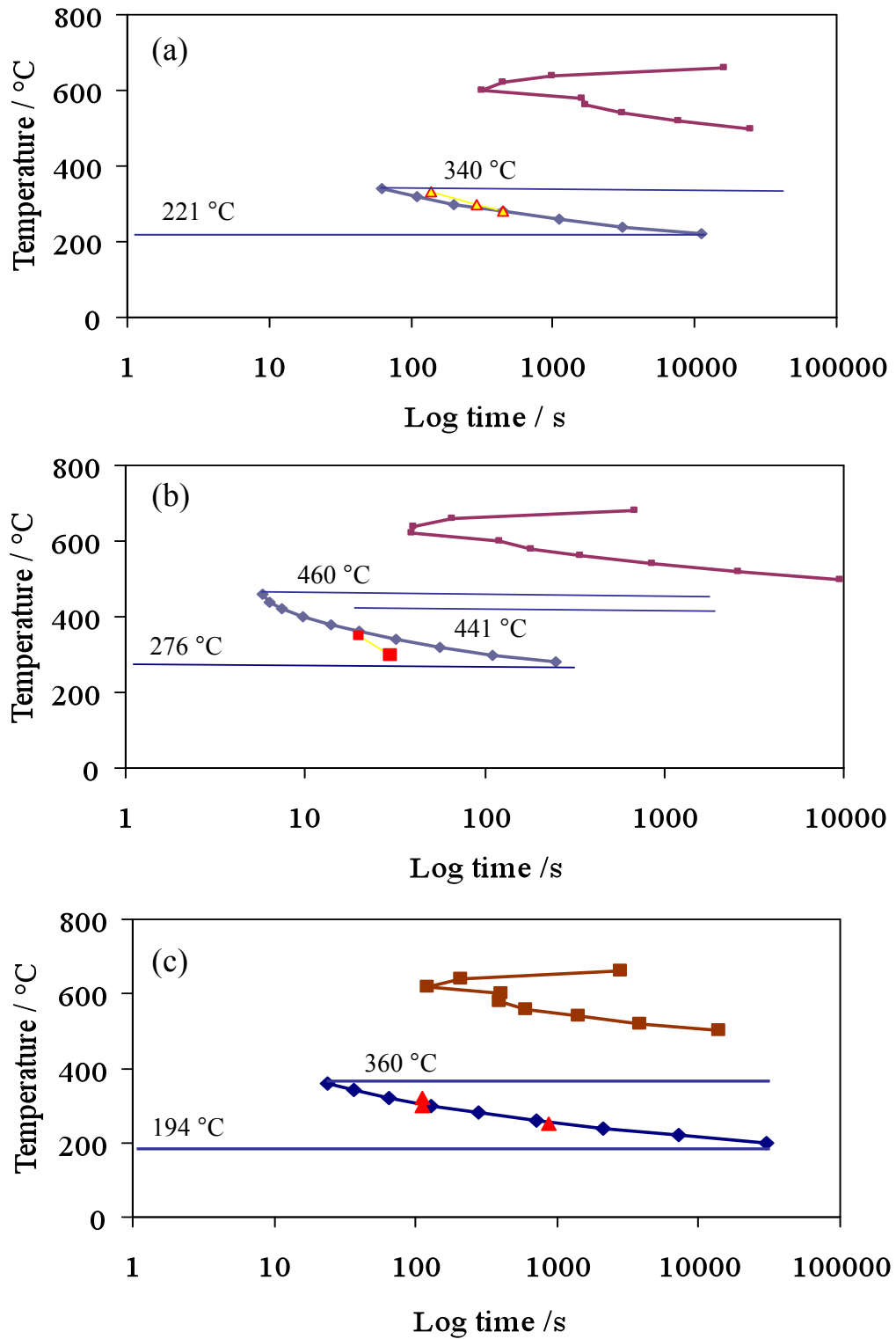
Figure 7.6: TTT diagrams for the initiation of isothermal reaction. (a) Alloy EE22. (b) Alloy EE24. (c) Alloy EE25.

7.2.6 Optical Microstructures

Microcracks were clearly visible in alloys EE22, EE23 and EE25 specimens austenitised at 930 °C and quenched which contained untempered high-carbon martensite plates which are known to be brittle, figure 7.7 (a, b, c and d). The cracks propagate across the plates and the largest of plates appeared to be periodically cracked as has been previously observed [109]. Small amounts of bainite were also be observed in alloys EE24 and EE25 upon cooling.

Figure 7.8 shows the effect of austenitisation temperature on the extent of micro-cracking in alloy EE25. After austenitisation at 930 °C, the cracks are more severe, crossing through the martensite plates and the grain boundaries. By lowering the austenitisation temperature to 800 °C, microcracking is only seen across the martensite plates. It is possible that quenching the specimens after low austenitisation temperature makes the fine martensite shape and avoid the cracks propagating along the untempered martensite brittle phase [109, 110]. Small amounts of bainite can also be observed in alloy EE25 upon cooling. The plates of martensite naturally become finer as austenite grain size, $L\gamma$, decreases, table 7.5.
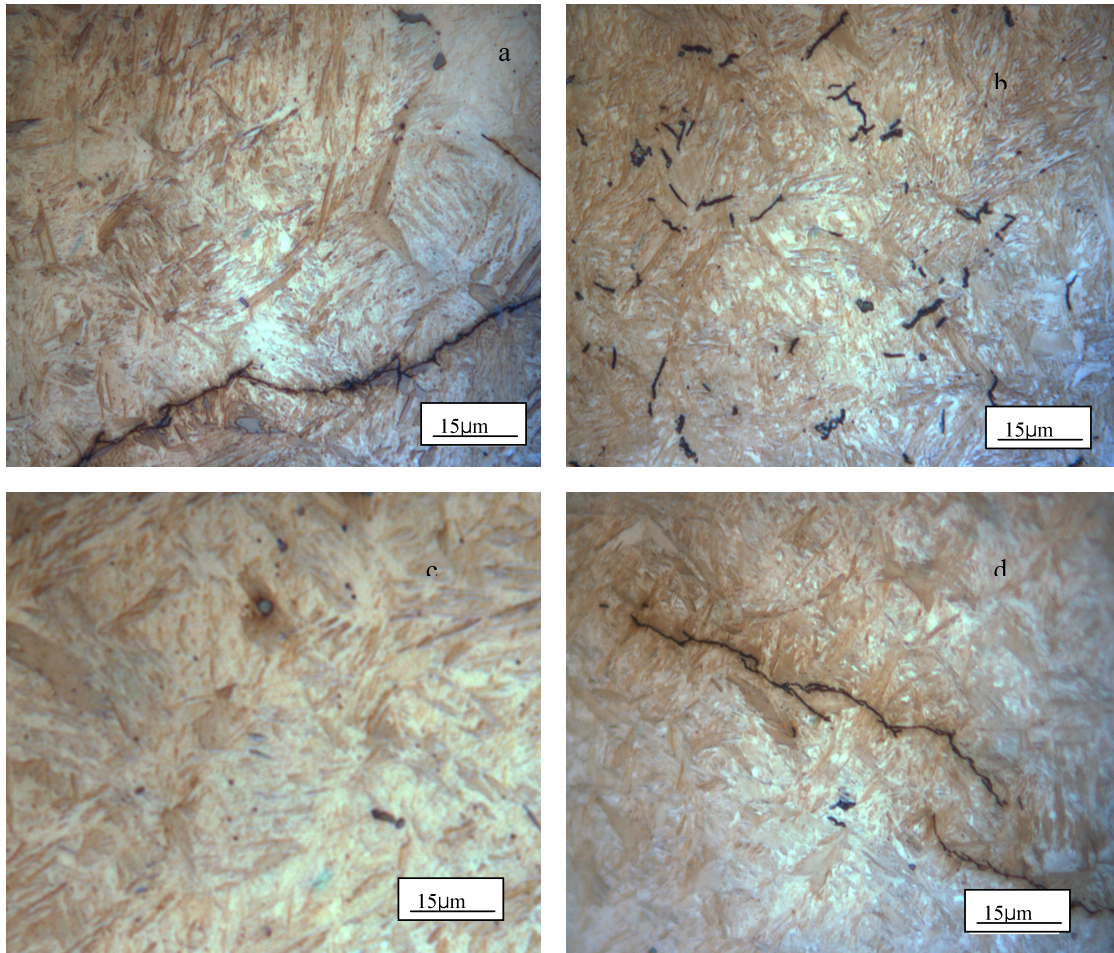
Figure 7.7: Optical micrographs showing micro-cracking of as quenched martensite for (a) Alloy EE22. (b) Alloy EE23. (c) Alloy EE24 free from cracking in microstructure. (d) Alloy EE25.

Figure 7.8: Extent of micro-cracking in alloy EE25 after direct quenching from the austenitisation temperature of (a) 930 °C, (b) 800 °C.

Table 7.5: The austenite grain size and the error after austenitisation at two different temperatures.

T_γ / °C	L_γ / μm	Error
930	23.8	2
800	11.0	0.5

7.2.7 Bainite in the alloy

Once the kinetic data for the formation of bainitic ferrite are obtained, the bainitic microstructure can be predicted and controlled. Figure 7.9 shows a micrograph of bainite in alloy EE24 after the specimen is austenitised at 930 ºC and then isothermally hardened at 300 ºC. Figure 7.10 shows a microstructural comparison between alloy EE24 and EE25.
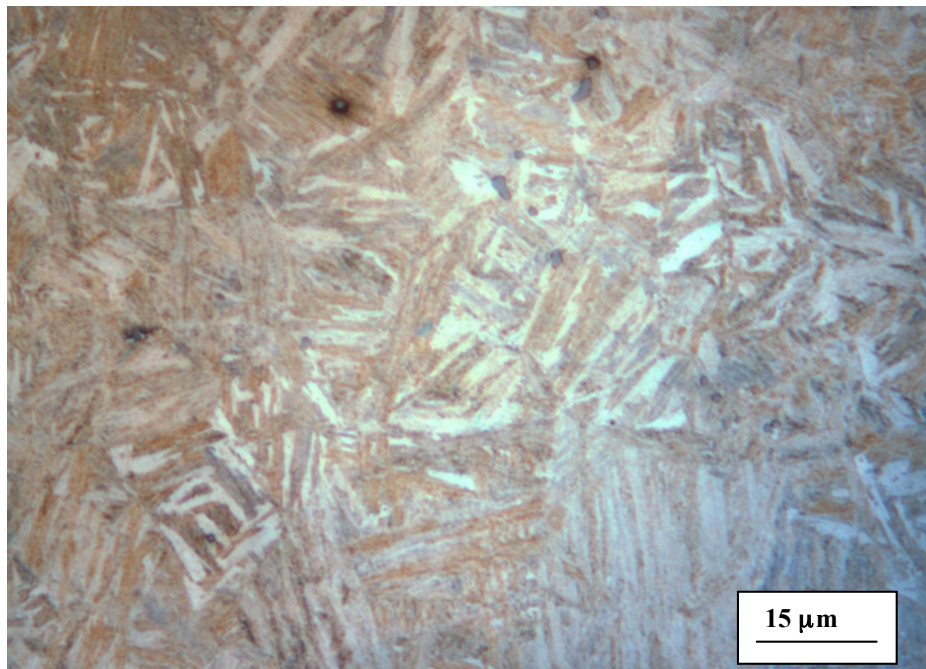
Figure 7.9: Optical micrograph showing bainite in alloy EE24 after isothermal hardening at 300 ºC, hardness 546 ± 1 HV with a load of 50 kg.
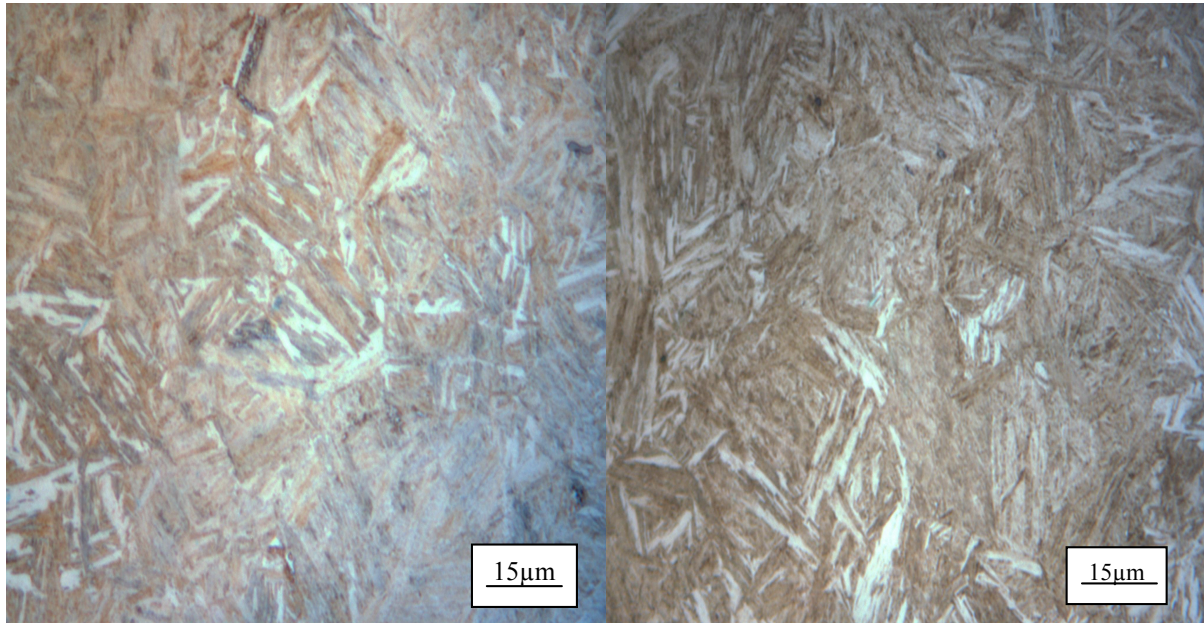
(a) EE24: Transformation to bainite at 300 °C. Hardness 546 / ±1 HV with a load of 50 kg.

(b) EE25: Transformation to bainite at 250 ºC. Hardness 666 / ±19 HV with a load of 30 kg.

Figure 7.10: Optical micrograph showing (a) bainite in alloy EE24. (b) bainite in alloy EE25.

A steel with a high hardenability is one which has a low critical cooling rate, so that even slow cooling will lead to a martensitic structure. This has the advantage that a hard material can be generated without the risk of "quench cracking" due to low thermal gradients associated with slow cooling. Alloy EE24 has been selected after thermodynamic and kinetic calculations and microstructural analysis which showed that this alloy does not have any cracks.

When the grain size of the austenite has been reduced by lowering the austenisation temperature, the martensite plates become finer and thermal cracks disappear after quenching. The grain size of austenite

decreased to about 50% after lowering the austenisation temperature from 930 ℃ to 800 ℃ for the alloy EE25.

7.3 The results of experiments related to the model of fracture toughness

This section is concerned with the results related to the experiments on alloy PP1; the chemical composition and heat treatment of the alloy were explained previously in chapter three. This work studied the effect of tempering for different times and temperatures on the stability of the microstructure and mechanical properties in this alloy.

7.3.1 Hardness

Tempered bainite for the alloy PP1 at 400 °C with different tempering times showed a small variation in the hardness as illustrated in table 7.6. The general trend is a slight decrease in hardness as the tempering time increases. This is in agreement with the work of Peet *et al.* on the tempering of an alloy of super-bainitic steel [103]. Figure 7.11 shows the measured hardness against different tempering times. In the present work, and consistent with Peet's work, no strong influence of tempering time on hardness has been found. The bainitic microstructure resists the tempering treatment, which is different from the response of the martensite microstructure [111].

Table 7.6: **The hardness for tempered bainite at 400 °C with different times.**

Tempering Time / min	Hardness / HV	Error / %
0	645	± 8
50	632	± 10
100	637	± 6
120	625	± 10
150	628	± 8
200	626	± 12
240	625	± 9
250	625	± 11
360	611	± 8
480	612	± 9
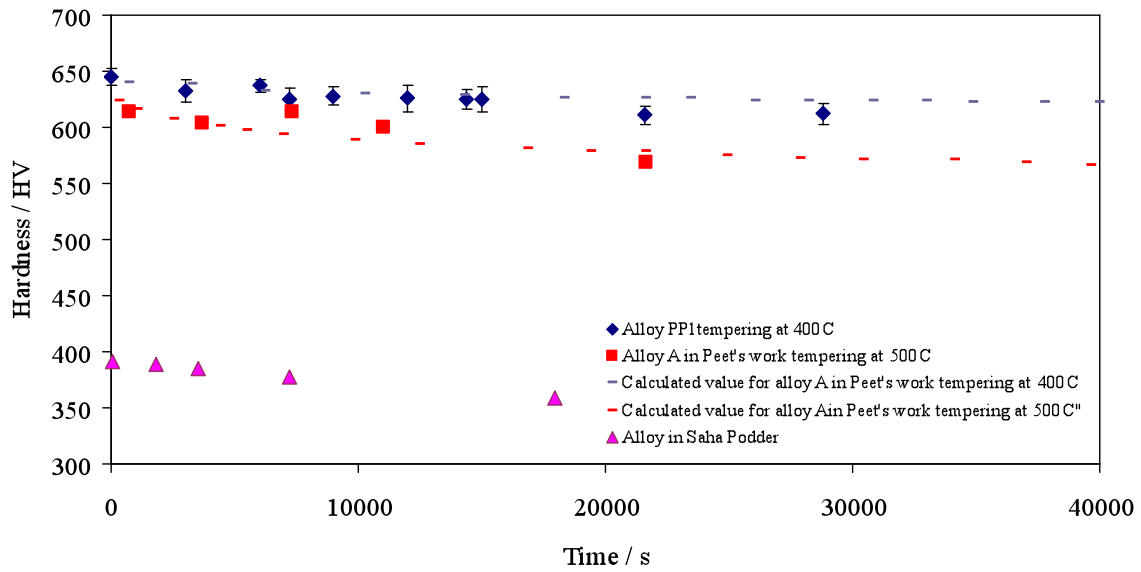
Figure 7.11: The variation of hardness of bainite with tempering time for alloy PP1, at a temperature of 400 °C and some experimental and calculated values from Peet's work for alloy A[1] [103], and from Podder and Bhadeshia's work for alloy B[2] [112].

Table 7.7 and Figure 7.12 show the variation of hardness of bainite with tempering temperature. The results show that the hardness falls sharply as tempering temperature increases above 450 °C. These results are consistent with those reported for low temperature bainite [30, 103].

---

[1] 0.79C-1.59Si-1.94Mn-0.02Ni-1.33Cr-0.3Mo wt%.
[2] 0.22C-2.03Si-3Mn wt%.

Table 7.7: The hardness of tempered bainite after tempering for 6 hours at different temperatures.

Tempering Temp. / °C	Hardness / HV	Error / %
0	645	± 8
300	642	± 5
350	619	± 6
400	611	± 8
450	626	± 6
500	556	± 10
550	467	± 5
600	377	±4
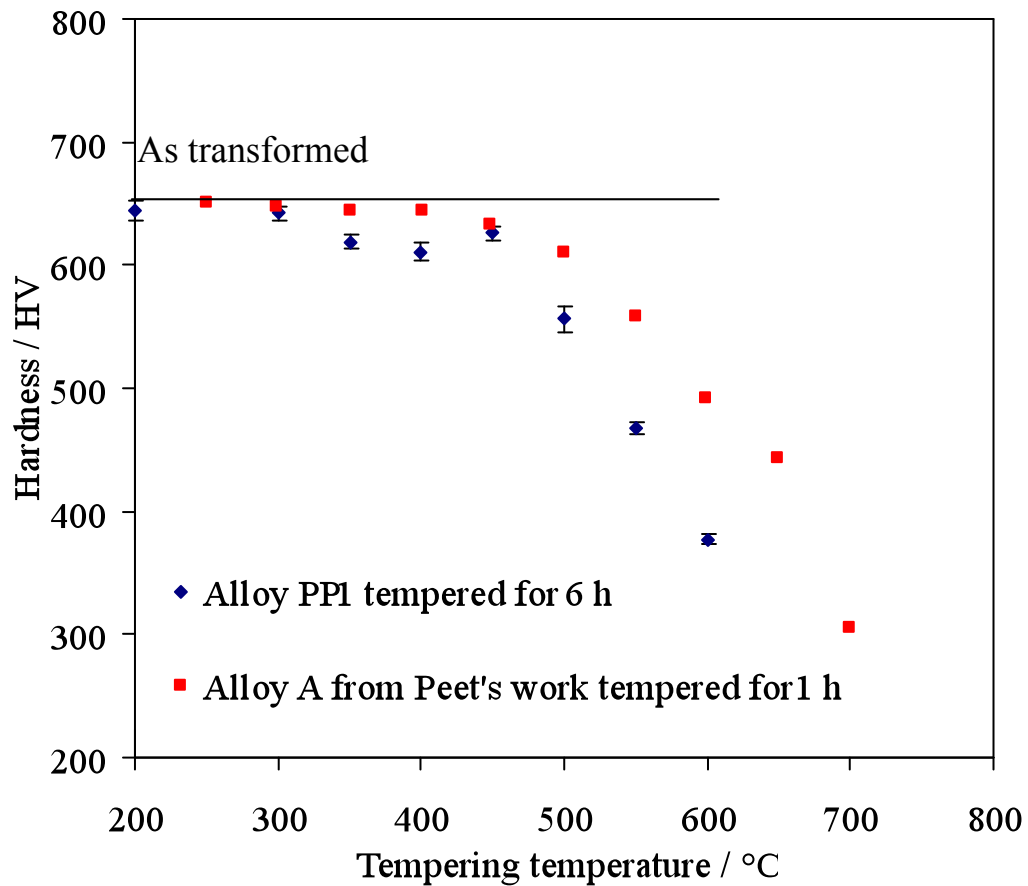
Figure 7.12: The variation of hardness of bainite with tempering temperature; tempering time for alloy PP1 is 6 hours and for alloy A is 1 hour [30, 103].

7.3.2. XRD test results

The volume fractions of the phases in the alloy PP1 were measured in the as-transformed condition and after tempering using X–ray diffraction as shown in figure 7.13. Table 7.8 shows the volume fraction of retained austenite, bainitic ferrite and the lattice parameter of austenite. It can be stated that the volume fraction of retained austenite decreases with the increase of the tempering temperature as shown in figure 7.13b and figure 7.13c, the austenite peaks decrease in intensity while those of

ferrite become more in tense. It is clear that there is still austenite in the microstructure even after tempering at 450 °C. It is speculated that a small amount of austenite will still be present in the structure until the tempering temperature reaches 500 °C, but will completely decompose just below 550 °C which leads to a change in thickness of the bainite plates as was explained in [103].

Table 7.8: Result of X-ray diffraction analysis.

Condition	Austenite / %	Lattice Parameter for austenite/ Å	Ferrite / %
As transformed	32±0.000113	3.6265±0.000198	67.9±0.00073
Tempered at 400 °C for 6h	15.5 ± 0.4	3.60743 ± 0.0004	84.52 ± 0.4
Tempered at 450 °C for 6h	4.5 ± 0.55	3.5988 ± 0.0056	95.48 ± 0.55
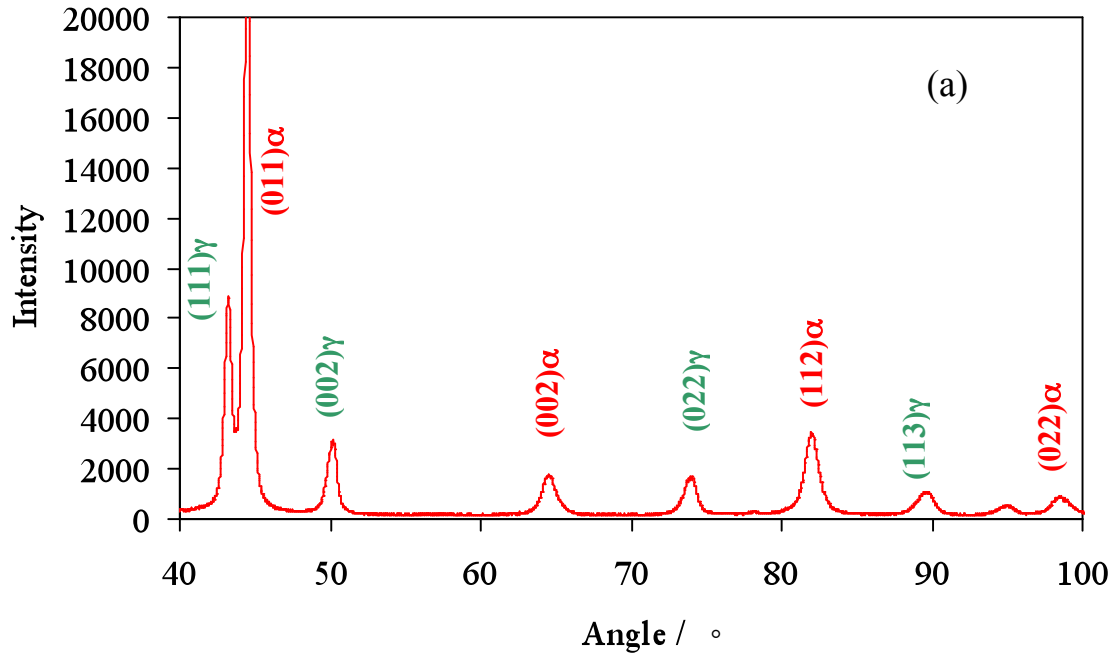
Figure 7.13: The XRD of material PP1, (a) as transformed, (b) after tempering at 400 °C for 6 h (c) after tempering at 450 °C for 6 h.
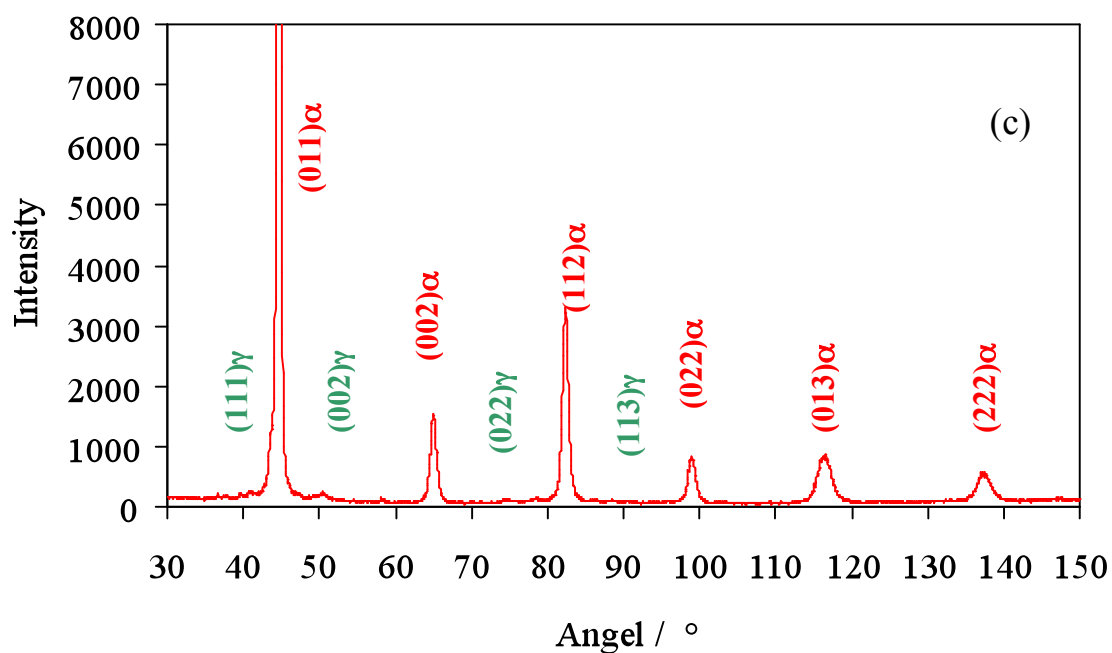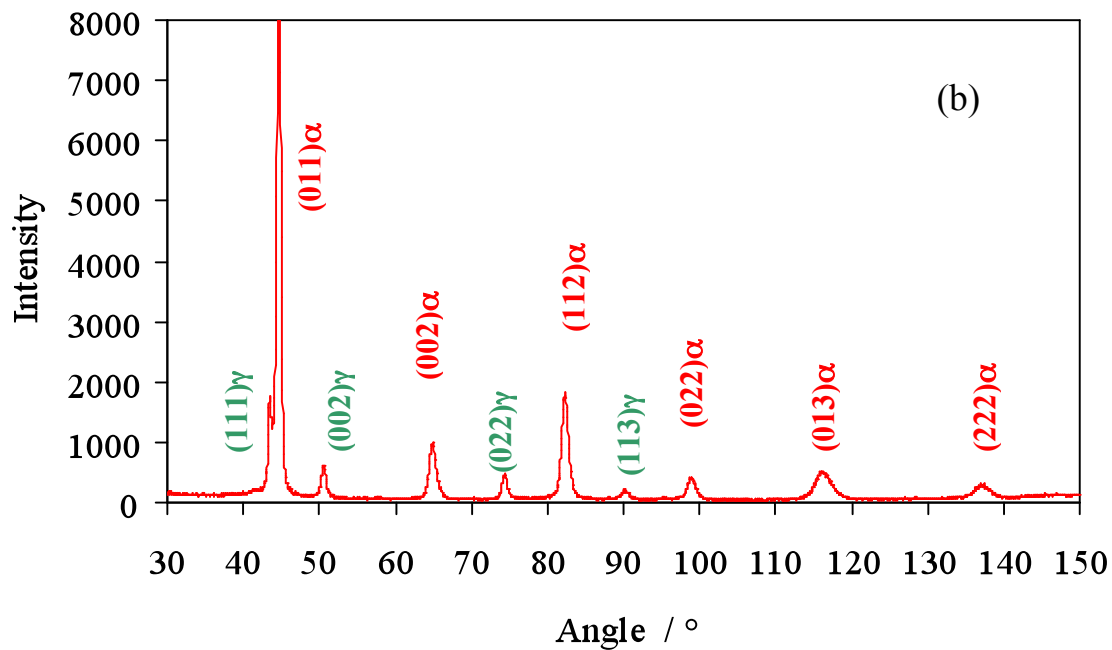
Figure 7.13 (continued): The XRD of material PP1, (a) as transformed, (b) after tempering at 400 °C for 6 h (c) after tempering at 450 °C for 6 h.

7.3.3 Tensile properties

The yield and ultimate tensile strength of alloy PP1 in the isothermally hardened condition were 1383 MPa and 1622 MPa respectevly. Figure 7.14 shows the stress-strain diagram of the alloy after tempering at 450 °C for 6 h and the yield stress for the alloy in this condition was found to be 1253 MPa. The results of tensile tests for the alloy after tempering at different temperatures are shown in Table 7.9. The mechanical properties did not greatly change with different tempering temperatures. The sample tempered at 400 °C gave an unreliable value possibly due to presence of defects or inclusions in the samples.
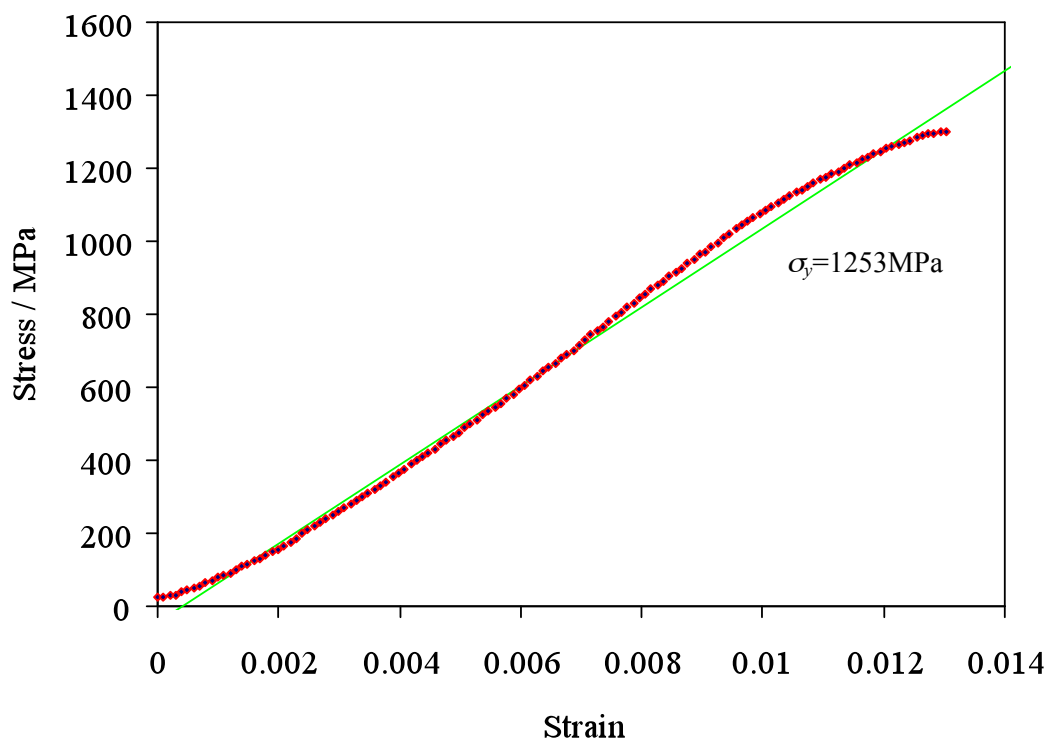
Figure 7.14: The tensile test for sample tempered at 450 °C for 6 h.

Table 7.9: The values of yield strength (σ_y) and ultimate tensile strength (σ_u) for the samples tempered at different tempering conditions.

Sample Condition	σ_y / MPa	σ_u / MPa
Isothermally hardened	1383	1622
Tempered at 300 °C for 6 hours	1285	1285
Tempered at 400 °C for 8 hours	950	968
Tempered at 450 °C for 6 hours	1253	1289
Tempered at 606 °C for 6 hours	1267	1514

7.3.4 Fracture toughness

Figure 7.15 shows the load-displacement trace of the fracture toughness test for the alloy PP1 in the isothermally hardened condition. Reported plane strain fracture toughness value is 30 MPa m$^{0.5}$ for the isothermally transformed material. In this work, K_Q was found to be 31.18 MPa m$^{0.5}$ as shown in table 7.10 which is close to the standard value.
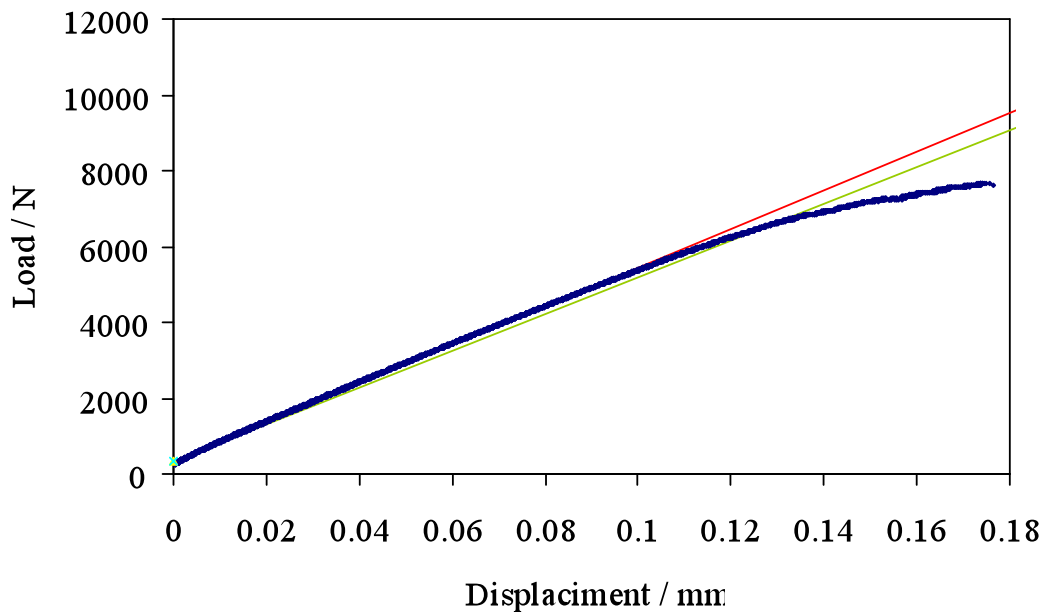
Figure 7.15: Load-displacement trace of the fracture toughness test for alloy PP1 in the isothermally hardened condition.

Table 7.10 lists the K_Q values for these tempering conditions and the validity of the plane strain fracture toughness tests. The general trend is a decrease in fracture toughness as the tempering temperature increases. This is related to the microstructure of this alloy. As it was explained in [30, 103], this is consistent with grain growth when it starts to occur and is not chiefly dependent upon carbon in solid solution.

Table 7.10: The values of K_Q for the samples tempered at different tempering conditions on the alloy PP1.

Sample Condition	K_Q / MPa m$^{0.5}$	Status	Reason
Isothermally hardened	31	Not valid	$a_c{}^3$ out of the range
Tempered at 300 °C for 6 hours	27	Not valid	$P_{max}{}^4 / P_Q{}^5 > 1.1$
Tempered at 300 °C for 1 month	23	Not valid	a_c less than the range
Tempered at 400 °C for 8 hours	23	Valid	-
Tempered at 450 °C for 6 hours	20	Not valid	a_c less than the range
Tempered at 500 °C for 6 hours	22	Valid	-
Tempered at 606 °C for 6 hours	13.8	Not valid	$P_f{}^6 / P_Q > 0.6$

7.3.4.1 The fracture surface

Figure 7.16 shows an optical macrograph of the fracture surface of compact tension sample of PP1 alloy transformed at 200 °C for ten days and tempered at 606 °C for 6 h, after fracture toughness testing. There

---

[3] the average crack length does not satisfy the standard requirements
[4] maximum applied load
[5] the peak fracture toughness load
[6] the maximum fatigue load

are two distinct fracture areas, one represents the fatigue pre-cracking and the other represents the static tensile fracture.

Figure 7.17 shows SEM for the fatigue pre-cracking area after tempering at 450 °C for 6 h. Multiple micro-cracks can be seen during fatigue cracking with crack growth along the prior austenite grain boundaries
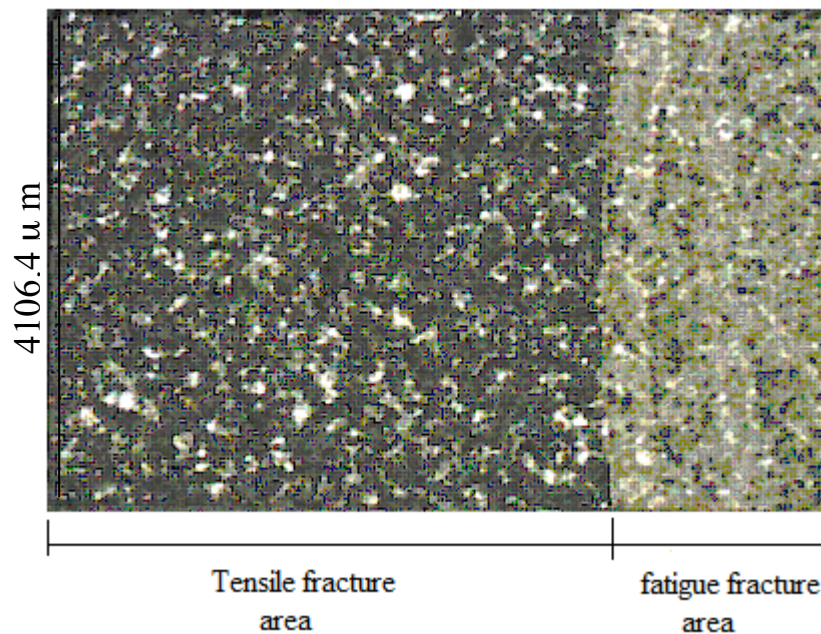
Figure 7.16: Optical macrograph (magnification 3.16×10 ^{3}) with of the fracture surface after a fracture toughness test, sample from alloy PP1 tempered at 606 °C for 6 h.
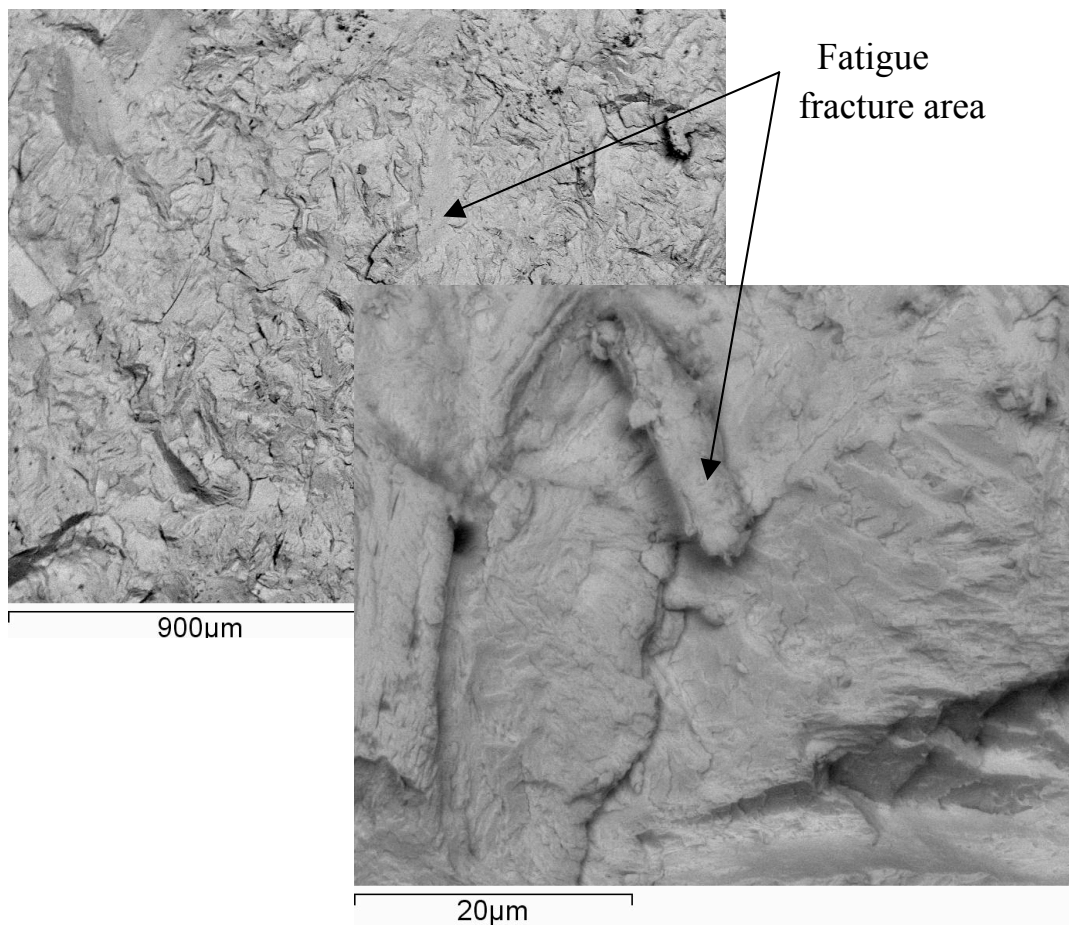
Figure 7.17: SEM of the fatigue pre-cracking area showing multiple micro-cracks, sample from alloy PP1 tempered at 450 °C for 6.

7.4 Conclusions

Alloys EE22, EE23, EE24 and EE25 have been directly quenched to martensite and also isothermally transformed to bainite. The hardness was measured for both heat treatments and metallographic analysis was carried out to identify the best alloy from these four alloy steels. Large cracks have been found inside the microstructure of the alloys EE22, EE23 and EE25. Reduction of the austenitisation temperature to a value just higher than A_{e3} temperature in alloy EE25 has led to complete disappearance of the cracks due to smaller austenite parent grain size. The

results of the hardness of these alloys will be used in chapter five to verify the accuracy of the hardness model.

More experiments were carried out on another alloy PP1. This alloy has been transformed isothermally to a baintic structure and tempered at different temperatures. Experimental results of plane strain fracture toughness tests show that the candidate values of plane strain fracture toughness decrease as the tempering temperature increases. Some of the results of plane strain fracture toughness will be used as input data to build a plane strain fracture toughness model and the rest will be used to verify this model.

Chapter 8

General Conclusions and Proposed Further Research

8.1 Conclusions

From the work of the present study, the following conclusions may be drawn:

1- It was possible, through the application of thermodynamics and kinetics principles, to control the microstructure of four high-strength alloy steels. One of the alloys studied was free from thermal cracks and was recommended for use in the automobile industry.

2- Keeping of the austenitisation temperature to a level just above the upper critical temperature A_{e3} reduced the probability of the appearance of thermal cracks after direct quenching.

3- The super-bainitic microstructure of a high-carbon, high-silicon low-alloy steel was found to be resistant to tempering, and the hardness and tensile properties of the alloy were not greatly affected by tempering. Fracture toughness however, showed a general decrease as the tempering temperature was increased.

4- Neural-network models have been developed for the estimation of Vickors hardness, volume percent of bainite and plane-strain fracture toughness respectively. The work has been applied to super-bainite steels.

5- The model of hardness is validated through new experiments carried out in this work for certain types of steels. The model gave satisfactory predictions.

6- A neural network model has successfully been used to predict the volume percent of bainite for a wide range of steels including the super-bainite steels.

7- A neural network model based on either mechanical properties alone or chemical composition alone did not give a satisfactory prediction for plane strain fracture toughness.

8- A neural network model based on chemical composition, heat treatment and mechanical properties has been proposed to predict the plane-strain fracture toughness of steels. In general, the predictions are acceptable but the modelling uncertainty tends to be large. More input data need to be collected for bainitic steels as more research is published in the future to improve the predictions of the model.

8.2 Proposed further research

1. Introducing the time of isothermal transformation as an input variable in an effort to improve the models of hardness and bainite volume percent.

2. Study of the effect of tempering bainite at high temperatures on the plane strain fracture toughness.

3. Study of the effect of other alloying elements, such as copper, on the super-bainite steels to enhance the plane strain fracture toughness.

4. Use Gaussian processes modelling to estimate the hardness, volume percent of bainite and plane strain fracture toughness instead of neural-network modelling and compare the prediction of the two modelling methods.

References:

[1]   H. K. D. H. Bhadeshia, "Phase transformations contributing to the properties of modern steels," *Bulletin of the Polish Academy of Sciences-Technical Sciences*, vol. 58, pp. 255-265, 2010.

[2]   H. K. D. H. Bhadeshia, "Hard bainite," *The Minerals Metals & Materials Society*, vol. 1, pp. 469-484, 2005.

[3]   H. K. D. H. Bhadeshia, "Bainitic bulk-nanocrystalline steel," *The 3rd International Conference on Advanced Structural Steels Gyeongju*, Korea, pp. 33-40, August 22-24, 2006.

[4]   M. A. Yescas-González, "Prediction of Vickers hardness in austempered ductile iron using neural networks," *International Journal of Cast Metals Research*, vol. 15, pp. 1513-1521, 2003.

[5]   R. C. Dimitriu, *Complex Mechanical Properties Of Steel*, Ph. D. thesis, University of Cambridge, UK., 2009.

[6]   T. Sourmail, H. K. D. H. Bhadeshia, and M. D. J. C. MacKay., "Neural network model of creep strength of austenitic stainless steel.," *Materials Science and Technology*, vol. 18, pp. 655-663, 2002.

[7]   J. D. Robson and H. K. D. H. Bhadeshia, "Modelling precipitation sequences in power plant steels: Part I, kinetic theory.," *Materials Science and Technology*, vol. 13, pp. 631-639, 1997.

[8]   J. D. Robson and H. K. D. H. Bhadeshia., "Modelling precipitation sequences in power plant steels, Part II: Application of kinetic," *Materials Science and Technology*, vol. 28, pp. 640-644, 1997.

[9]   R. Kemp, G. A. Cottrell, H. K. D. H. Bhadeshia, G. R. Odette, T. Yamamoto, and H. Kishimoto, "Neural-network analysis of irradiation hardening in low-activation steels," *Journal of Nuclear Materials*, vol. 348, pp. 311-328, 2006.

[10]   T. Sourmail and C. Garcia-Mateo, "A model for predicting the martensite-start temperature of steels," *Computational Materials Science*, vol. 34, pp. 213-218, 2005.

[11] J. Pak, J. Jang, H. K. D. H. Bhadeshia, and L. Karlsson, "Optimization of Neural Network for Charpy Toughness of Steel Welds," *Materials and Manufacturing Processes*, vol. 24, pp. 16-21, 2009.

[12] H. K. D. H. Bhadeshia, "Modelling of recrystallization in mechanically alloyed materials," *Materials Science and Engineering A*, vol. A223:, pp. 91-98, 1997.

[13] J. H. Ryu, *Model for Mechanical Properties of Hot-Rolled Steels*, Ms.C. thesis, Pohang University of Science and Technology, Korea, 2008.

[14] C. G. Windsor, G. Cottrell, and R. Kemp, "Prediction of yield stress in highly irradiated ferritic steels," *Modelling and Simulation in Materials Science and Engineering*, vol. 16, p 14, 2008.

[15] H. K. D. H. Bhadeshia, "A Personal commentary on "Transformation of Austenite at Constant Subcritical Temperatures"," *Metallurgical and Materials Transactions A*, vol. 41A, pp. 1351-1390, 2010.

[16] H. K. D. H. Bhadeshia, *Bainite in Steels*, IOM Communications Ltd, London, 2001.

[17] H. K. D. H. Bhadeshia and R. W. K. Honecombe, *Steels Microstructure and Properties*, Elsevier Ltd., London, 2006.

[18] M. Takahashi, *Reaustenitisation From Bainite In Steels*, Ph. D. thesis, University of Cambridge U.K., 1992.

[19] H. K. D. H. Bhadeshia, "Diffusional and displacive transformations," *Scripta Metallurgica*, vol. 21, pp. 1605-1609, 1987.

[20] E. Swallow and H. K. D. H. Bhadeshia, "High resolution observation of displacements caused by bainitic transformation," *Materials Science and Technology*, vol. 2, pp. 121-125, 1996.

[21] C. Garcia-Mateo, F. G. Caballero, and H. K. D. H. Bhadeshia, "Development of hard bainite," *ISIJ International*, vol. 43, pp. 1238-1243, 2003.

[22] J. G. Speer, D. K. Matlock, B. C. D. Cooman, and J. G. Schroth, "Carbon partitioning into austenite after martensite transformation," *Acta Materialia*, vol. 51, pp. 2611-2622, 2003.

[23] J. G. Speer, D. V. Edmonds, F. C. Rizzo, and D. K. Matlock, "Partitioning of carbon from supersaturated plates of ferrite, with application to steel processing and fundamentals of the bainite transformation," *Current Opinion in Solid State & Materials Science*, vol. 8, pp. 219-237, 2004.

[24] B. C. Muddle and J. F. Nie, "Formation of bainite as a diffusional displacive phase transformation," *Scripta Materialia*, vol. 47, pp. 187-192, 2002.

[25] A. Saha, G. Ghosh, and G. B. Olson, "An assessment of interfacial dissipation effects at reconstructive ferrite-austenite interfaces," *Acta Materialia*, vol. 53, pp. 141-149, 2005.

[26] H. S. Yang and H. K. D. H. Bhadeshia, "Designing low carbon, low temperature bainite," *Materials Science and Technology*, vol. 24, pp. 335-342, 2008.

[27] J. Mahieu, *Contribution to the physical metallurgy of crash-resistant galvanized TRIP-assisted steel for automotive structures.*, Ph.D. thesis, Ghent University, 2003.

[28] M. Sherif, *Characterisation And Development Of Nanostructured Ultra High Strength And Ductile Bainitic Steel*, Ph. D thesis, University of Cambridge UK., 2006.

[29] H. K. D. H. Bhadeshia and A. R. Waugh, "Bainite: an atom-probe study of the incomplete reaction phenomenon," *Acta Materialia*, vol. 30, pp. 775-784, 1982.

[30] F. G. Caballero, H. K. D. H. Bhadeshia, K. J. A. Mawella, D. G. Jones, and P. Brown, "Very strong low temperature bainite," *Materials Science and Technology*, vol. 18, pp. 279-284, 2002.

[31] C. Garcia-Mateo, F. G. Caballero, and H. K. D. H. Bhadeshia, "Acceleration of low-temperature bainite," *Iron and Steel Society of Japan*, vol. 43, pp. 1821-1825, 2003.

[32] S. B. Singh and H. K. D. H. Bhadeshia, "Estimation of bainite plate thickness in low alloy steels " *Materials Science and Engineering A*, vol. 245, pp. 72-79, 1998.

[33] G. Langford and M.Cohen, "Calculation of cell-size strengthening of wire drawn iron," *Metall.Transformation.1 No*, vol. 1, pp. 1478-1480, 1970.

[34] F. G. Caballero and H. K. D. H. Bhadeshia, "Very strong bainite," *Current Opinion Solid State and Material Science*, vol. 8, pp. 251-257, 2004.

[35] C. Garcia-Mateo, F. G. Caballero, and H. K. D. H. Bhadeshia, "Low temperature bainite," *Journal de physique IV*, vol. 112, pp. 285-288, 2003.

[36] H. K. D. H. Bhadeshia, "Large chunks of very strong steel," *Millenium Steel*, vol. 5, pp. 25-28, 2004.

[37] T. Yokota, C. G. Mateo, and H. Bhadeshia, "Formation of nanostructured steels by phase transformation," *Scripta Materialia*, vol. 51, pp. 767-770, 2004.

[38] H. K. D. H. Bhadeshia, "High performance bainitic steels," *Materials Science Forum*, vol. 500-501, pp. 63-74, 2005.

[39] H. K. D. H. Bhadeshia, *The nature mechanism and properties of strong bainite*, Institute of Japan, Proceedings of the 1st International Symposium on Steel Science IS3–2007.

[40] C. H. Young and H. K. D. H. Bhadeshia, "Computer modelling for yield strength of the mixed micro-structure of bainite and martensite," *De Physique IV*, vol. 5, pp. C8-267-C268-272, 1995.

[41] K. J. Irvine and F. B. Pickering, "Physical properties of martensite and bainite," *special report*, vol. 93, pp. 110-125, 1965.

[42] H. K. D. H. Bhadeshia and D. V. Edmond, "Bainite in silicon steels: new composition-property approach part 1," *Metal Science*, vol. 17, pp. 411-419, 1983.

[43] M. A. Meyers and K. K. Chawla, *Mechanical Behaviour Of Materials* University of Cambridge ,U.K., 2009.

[44] C. Windsor, G. Cottrell, and R. Kemp, "Prediction of the Charpy transition temperature in highly irradiated ferritic steels," *Modelling and Simulation in Materials Science and Engineering*, vol. 16, p 13, 2008.

[45] H. K. D. H. Bhadeshia, D. J. C. Mackay, and L. E. Svensson, "The impact toughness of C-Mn steel arc welds a bayesian neural network analysis," *Materials Science and Technology*, vol. 11, pp. 1046-1051, 1995.

[46] H. Fujii, D. J. C. MacKay, and H. K. D. H. Bhadeshia, "Bayesian neural network analysis of fatigue crack growth rate in nickel base superalloys," *ISIJ International*, vol. 36, pp. 1373-1382, 1996.

[47] J. M. Schooling, M. Brown, and P. A. S. Reed, "An example of the use of neural computing techniques in materials science -the modelling of fatigue thresholds in Ni-base superalloys," *Materials Science and Engineering A*, vol. A260, pp. 222-239, 1999.

[48] D. J. C. MacKay, *Information Theory, Inference and learning algorithms,* , Cambridge University, 1 edition, 2003.

[49] D. J. C. MacKay, "Practical Bayesian framework of back propagation networks," *Neural Computation*, vol. 4, pp. 448-472, 1992.

[50] H. K. D. H. Bhadeshia, "Review neural networks in materials science," *ISIJ International*, vol. 39, pp. 966-979, 1999.

[51] D. J. C. MacKay, *Bayesian non linear modelling with neural networks*, University of Cambridge program for industry: modelling phase transformations in steels, 1995.

[52] D. J. C. MacKay, *Bayesian methods for adaptive models* Ph. D. thesis, California Institute of Technology, U.S.A., 1992.

[53] D. J. C. MacKay, "Bayesian interpolation," *Neural Computation*, vol. 4, pp. 415-447, 1992.

[54] T. Sourmail and H. K. D. H. Bhadeshia, *Neural Networks Introduction to Materials Modelling*, ed. Z. Barbeer, Institute of Materials, London, 2005.

[55] S. A. Forsik, *Mechanical Properties Of Material For Fusion Power Plants*, Ph. D. thesis, University of Cambridge U.K., 2009.

[56] H. K. D. H. Bhadeshia, "Mathematical models in materials science," *Materials Science and Technology*, vol. 24, pp. 128-136, 2008.

[57] H. K. D. H. Bhadeshia, R. C. Dimitriu, S. Forsik, J. H. Pak, and J. H. Ryu, "Performance of neural networks in materials science," *Materials Science and Technology*, vol. 25, pp. 504-510, 2009.

[58] M. A. Yescas-González, *Modelling the microstructure and mechanical properties of austempered ductile irons*, Ph. D. thesis, University of Cambridge, U.K., 2001.

[59] M. Peet, *Assessment of the steel produced by carpenter speciality alloys*, Internal Report Submitted to The University of Cambridge, Materials Science and Metallurgy, Cambridge, 2005.

[60] H. M. Rietveld, "Line profiles of neutron powder-diffraction peaks for structure refinement," *Acta Cryst*, vol. 22, pp. 151-152, 1968.

[61] H. M. Rietveld, "A profile refinement method for nuclear and magnetic structures," *Applied Crystal*, vol. 2, pp. 65-71, 1969.

[62] *ASTM: E 399-90 Standard Test Method for Plane-Strain Fracture Toughness of Metallic Materials*, Copyright © ASTM International, 100 Barr Harbor Drive, PO Box C700, West Conshohocken, PA 19428-2959, United States, 1997.

[63] *Department of Materials Science and Metallurgy, http://www.msm.cam.ac.uk/mechtest/machine%20pages/mayes100.html*.

[64] *Department of Materials Science and Metallurgy, http://www.msm.cam.ac.uk/mechtest/machine%20pages/LCF%20testing. html*.

[65] *Department of Materials Science and Metallurgy, http://www.msm.cam.ac.uk/mechtest/machine%20pages/hounsfield.html*.

[66] T. Fujita, T. Ochi, and T. Tarui, "Prediction of hardness distribution in forged steel by neural network model," *Nippon Steel Technical Report*, vol. 96, pp. 57-61, 2007.

[67] W. G. Vermeulen, P. F. Morris, A. P. d. Weijer, and S. V. D. Zwaag, "Prediction of martensite start temperature using artificial neural networks," *Ironmaking and Steelmaking*, vol. 23, pp. 433-437, 1996.

[68] *http://www.msm.cam.ac.uk/map/steel/steelprog.html*.

[69] L. Gavard, H. K. D. H. Bhadeshia, D. J. C. Macky, and S. Suzuki, "Bayesian Neural Network Model for Austenite Formation in steels," *Materials Science and Technology*, vol. 12, pp. 453-463, 1996.

[70] *ATLAS of Isothermal Transformation Diagrams of B.S.En steels, Second Edition*, The Iron and Steel, London, 1956.

[71] C. Garcia-Mateo, M. Peet, F. G. Caballero, and H. K. D. H. Bhadeshia, "Tempering of hard mixture of bainitic ferrite and austenite," *Materials Science and Technology*, vol. 20, pp. 814-818, 2004.

[72] D. P. Koistinen and R. E. Marburger, "A general equation prescribing the extent of the austenite-martensite transformation in pure iron-carbon alloys and plain carbon steels," *Acta Metallurgica*, vol. 7, pp. 59-60, 1959.

[73] E. Kozeschnik and H. K. D. H. Bhadeshia, "Influence of silicon on cementite precipitation in steels," *Materials Science and Technology*, vol. 24, pp. 343-347, 2008.

[74] F. C. Zhang, T. S. Wang, P. Zhang, C. L. Zheng, B. Lv, M. Zhang, and Y. Z. Zheng, "A novel method for the development of a low-temperature bainitic microstructure in the surface layer of low-carbon steel," *Scripta Materialia*, vol. 59, pp. 294-296, 2008.

[75] H. K. D. H. Bhadeshia, "Nanostructured bainite," *Proceedings the royal of society*, vol. 466, pp. 3-18, 2009.

[76] H. K. D. H. Bhadeshia and D. V. Edmond, "Bainite in silicon steels: new composition-property approach: part 2," *Metal Science*, vol. 17, pp. 420-425, 1983.

[77] F. G. Caballero, H. K. D. H. Bhadeshia, K. J. A. Mawella, D. G. Jones, and P. Brown, "Design of novel high strength bainitic steels: Part 2," *Materials Science and Technology*, vol. 17, pp. 517-522, 2001.

[78] H. S. Hasan, M. Peet, H. Bhadeshia, S. Wood, and E. Booth, "Temperature cycling and the rate of the bainite transformation," *Materials Science and Technology*, vol. 26, pp. 453-456, 2010.

[79] T. N. Rouns, D. J. Moore, and K. B. Rundman, "Effect of manganese on structure and properties of austempered ductile iron: a processing window concept " *AFS Transactions*, vol. 94, pp. 255-264, 1986.

[80] M. A. Yescas, H. K. D. H. Bhadeshia, and D. J. MacKay, "Estimation of the amount of retained austenite in austempered ductile irons using neural networks " *Materials Science and Engineering* vol. A311, pp. 162-173, 2001.

[81] M. A. Yescas and H. K. D. H. Bhadeshia, "Model for the maximum fraction of retained austenite in austempered ductile cat iron," *Materials Science and Engineering*, vol. A333, pp. 60-66, 2002.

[82] S. Chatterjee, M. Murugananth, and H. K. D. H. Bhadeshia, "d TRIP steel," *Materials Science and Technology*, vol. 23, pp. 819-827, 2007.

[83] S. Chatterjee, *Transformations in TRIP-assisted steels: microstructure and properties A*, University of Cambridge, UK., 2006.

[84] G. I. Rees and H. K. D. H. Bhadeshia, "Bainite transformation kinetics part 1 modified model," *Materials Science and Technology*, vol. 8, pp. 985-993, 1992.

[85] N. A. Chester and H. K. D. H. Bhadeshia, "Mathematical modelling of bainite transformation kinetics," *De Physique IV* vol. 7, pp. C5-41-C45-46, 1997.

[86] F. G. Caballero, H. K. D. H. Bhadeshia, K. J. A. Mawella, and D. G. Jones, "Very strong low temperature bainite," *Materials Science and Technology*, vol. 18, pp. 279-284, 2002.

[87] H. K. D. H. Bhadeshia, *http://www.msm.cam.ac.uk/map/steel/programs/mucg73-b.html*.

[88] C. G. Mateo, M. Peet, F. G. Caballero, and H. K. D. H. Bhadeshia, "Tempering of hard mixture of bainitic ferrite and austenite," *Materials Science and Technology*, vol. 20, pp. 814-818, 2004.

[89] C. Garcia-Mateo, F. G. Caballero, and H. K. D. H. Bhadeshia, "Mechanical properties of low-temperature bainite," *Materials Science Forum*, vol. 500-501, pp. 495-502, 2005.

[90] J. Y. Kang, B. I. Choi, and H. J. Lee, "Application of artificial neural network for predicting plain strain fracture toughness using tensile test results," *Fatigue & Fracture of Engineering Materials & Structures*, vol. 29, pp. 321-329, 2006.

[91] M. E. Haque and K. V. Sudhakar, "ANN back-propagation prediction model for fracture toughness in microalloy steel," *International Journal of Fatigue*, vol. 24, pp. 1003-1010, 2002.

[92] H. Y. Duan, Y. T. Li, G. P. He, and J. Zhang, "Application of ANN back-propagation for fracture toughness in microalloy steel," *International Journal of Modern Physics B*, vol. 23, pp. 1191-1196, 2009.

[93] A. pineau, "Development of the local approach to fracture over the past 25 years: theory and applications," *Anales de la Mecanica de Fractura*, vol. 1, pp. 9-24, 2007.

[94] H. K. D. H. Bhadeshia, *Neural networks in materials science: The importance of uncertainty*, Bengal Engineering and Science University, Shibpur, Howrah, India, 2006.

[95] H. K. D. H. Bhadeshia, "Review neural networks and information in materials science," *Wiley InterScience, DOI:10.1002/sam.10018*, vol., 2009.

[96] F. G. Caballero, M.Miller, S. S. Baba, and C. Garcia-Mateo, "Atomic scale observations of bainite transformation in a high

carbon high silicon steel " *Acta. Materialia*, vol. 55, pp. 381-390, 2007.

[97] Y. Hongliang, *δ-TRIP Steel*, Ph.D. thesis, Pohang University of Science and Technology, Koria, 2010.

[98] E. R. Parker and R. F. Mehl, "Interrelations of compositions transformation kinetics morphology and mechanical properties of alloy Steels," *Metallurgical and Materials Transactions A*, vol. 8A, pp. 1025-1042, 1977.

[99] S. C. Lee and F. J. Worzala, "Fracture-behavior of AISI M-2 high-speed tool steel," *Metallurgical Transactions a-Physical Metallurgy and Materials Science*, vol. 12, pp. 1477-1484, 1981.

[100] H. Fua, Q. Xiao, and H. Fuc, "Heat treatment of multi-element low alloy wear-resistant steel," *Materials Science and Engineering A*, vol. 396, pp. 206–212, 2005.

[101] R. O. Ritchie and J. F. Knott, "On the influence of high austenitizing temperatures and "Overheating" on fracture and fatigue crack propagation in a low alloy steel," *Metallurgical Transactions*, vol. 5, pp. 782-785, 1974.

[102] Y. Song, Q. Luo, Q. Chen, and Y. Chen, "Effects of Re-B modification on the strength and toughness of 30Cr Mn 2Si cast steel," *Materials science and Technology*, vol. 29, pp. 1492-1496, 1994.

[103] M. Peet, *Transformation and tempering of low-temperature bainite*, Ph.D. thesis, The University of Cambridge, UK., 2010.

[104] C. Carcia-Mateo and F. G. Caballero, "Ultra-high-strength bainitic steels," *ISIJ International*, vol. 45, pp. 1736-1740, 2005.

[105] *MTDATA: Metallurgical and thermochemical databank. Teddington, UK: National Physical Laboratory; http://www.npl.co.uk/mtdata*, 1995.

[106] H. Yang and H. K. D. H. Bhadeshia, "Uncertainties in dilatometric determination of martensite start temperature," *Materials Science and Technology*, vol. 23, pp. 556-560, 2007.

[107] H. Yang, *Low-Carbon Low-Temperature Bainite*, Pohang University of Science and Technology, Pohang, Korea, 2007.

[108] H. K. D. H. Bhadeshia, "A thermodynamic analysis of isothermal transformation diagrams," *Metal Science*, vol. 16, pp. 159-165, 1982.

[109] S. Chatterjee and H. K. D. H. Bhadeshia, "TRIP-assisted steels: cracking of high-carbon martensite," *Materials Science and Technology*, vol. 22, pp. 645-649, 2006.

[110] S. Chatterjee, *Transformations in TRIP-Assisted Steels: Microstructure and Properties*, Ph. D. thesis, University of Cambridge, UK., 2006.

[111] F. G. Caballero, M. K. Miller, A. J. Clarke, and C. Garcia-Mateo, *Examination of carbon partitioning into austenite during tempering of bainite doi:10.1016/i.scriptamat.2010.04.049*, 2010.

[112] A. S. Podder and H. K. D. H. Bhadeshia, "Thermal stability of austenite retained in bainitic steels," *Materials Science and Engineering A*, vol. A 527, pp. 2121–2128, 2010.

Appendix A

Publications used for the database of the fracture toughness model

[1]   Y. Tomita, "Review improved fracture toughness of ultrahigh strength steel through control of non-metallic inclusions " *Materials Science*, vol. 28, pp. 853-859, 1993.

[2]   S. K. Putatunda, "Development of austempered ductile cast iron (ADI) with simultaneous high yield strenfth and fracture toughness by a novel two-step austempering process," *Materials Science and Engineering A*, vol. 315, pp. 70-80, 2001.

[3]   K. H. Khan and W. E. Wood, "The effect of step quenching on the microstructure and fracture toughness of AISI 4340 steel," *Metallurgical transactions A*, vol. 9A, pp. 899-906, 1978.

[4]   J. P. Materkowski and G. Krauss, "Tempered martinsite embrittlement in ASE 4340 steel," *Metallurgical Transactions A*, vol. 10 A, pp. 1643-1651, 1979.

[5]   O. N. Romaniv, A. N. Tkach, Y. N. Gladkii, and Y. V.Zima, "Fracture toughness of steel with a martensite-ferrite structue," *Fiziko-Khimicheskaya Mekanika Materialov*, vol. 13, pp. 31-36, 1977.

[6]   C. Garcia-Mateo, F. G. Caballero, and H. K. D. H. Bhadeshia, "Low temperature bainite," *Journal de physique IV*, vol. 112, pp. 285-288, 2003.

[7]   F. G. Caballero, H. K. D. H. Bhadeshia, K. J. A. Mawella, D. G. Jones, and P. Brown, "Design of novel high strength bainitic steels: Part 2," *Materials Science and Technology*, vol. 17, pp. 517-522, 2001.

[8]   H. Qiu, M. Enoki, K. Hiraka, and T. Kishi, "Effect of pre-strain on fracturevtoughness of ductile structural steels under static and dynamic loading," *Engineering fracture Mechanics*, vol. 72, pp. 1624-1633, 2005.

Nomenclature

a_c	Critical crack length	mm
A_{e1}, A_{e2}	Lower and upper equilibrium temperatures	°C
A_{c1}, A_{c3}	Lower and upper critical temperatures	°C
B	Thickness of sample for compact tension test	mm
c_i	Concentration of a substitutional solute	
C_i	Chemical composition	Wt%
E_D	Overall error	
E_w	Training regulariser	
E_i	The error accompanying each prediction	
E_{bar}	Average size of error bars	
HV	Vickers hardness	HV
H_γ	Hardness of retained austenite	HV
$H_{\alpha'}$	Hardness of the martensite	HV
H_o	Martensite hardness at a carbon content of $\bar{x}=0.43$	HV
H_b	Hardness of baintic ferrite	HV

h_i	Hidden unit of the network	
K_L	Coefficient for strengthening due to lath size	
K_p	Coefficient for strengthening due to dislocations	
K	Stress intensity factor	MPa m$^{0.5}$
K_c	Critical stress intensity factor	MPa m$^{0.5}$
K_{Ic}	Plane Strain Fracture toughness	MPa m$^{0.5}$
K_{max}	Maximum stress intensity factor	MPa m$^{0.5}$
K_Q	Candidate or conditional fracture toughness	MPa m$^{0.5}$
L	Model used to obtain the prediction $y^{(l)}$	
L	Number of models in the committee	
$\overline{L}$	The mean linear intercept	
LPE	Log predictive error	
M	Objective function	
M_s	Martensite-start temperature	°C
M_p	Mechanical properties	
N	The total number of predictions	
P_{max}	Maximum applied load	N
P_Q	Peak fracture toughness load	N
P_f	Maximum fatigue load	N
Q	Constant dependence of martensite hardness on carbon content (1020 HV/ wt%)	
R_{test}	Root mean square residual (RMS)	
S	Amount of carbon trapped in the bainitic ferrite	

T	Temperature	°C
T_a	Austenitising temperature	°C
T_{temp}	Tempering temperature	°C
t_{temp}	Tempering time	Min
T_0	Te zero curve (the free energies of austenite and ferrite of the same chemical composition are identical)	
T_0^C	The Te zero curve plus strain energy	
T_1	The temperature corresponding to the free energy curves	°C
T_q	The lowest temperature reached during quenching	°C
T_{1t}, T_{t2}	Transformation temperature step1 and step2 used for the model of fracture toughness	°C
t_{t1}, t_{t2}	Time needed for the transformation step1 and step2 used for the model of fracture toughness	Min
t^k	The set of outputs	
T_γ	Austenitisation temperature	°C
T	Plate thickness of bainite	μm
L_γ	Austenite grain size	μm
V_b	Volume fraction of bainite	
V_θ	Volume fraction of cementite	
W	Weights	
UTS	Ultimate tensile strength	MPa
α, β	Control parameters	

$\theta,\ \theta_{(1)},\ \theta_{(2)}$	Constants used in neural-network	
$\in$	Martensite phase	
$\in_b$	Bainite phase	
$\in_w$	Widmanstätten ferrite phase	
$x_{T_0\subset}$	Austenite carbon content	
$\bar{x}$	Average carbon concentration in the alloy	
$x_{\in_b}$	Carbon concentration of the bainite	
$\gamma,\ \alpha$	The phases of austenite and ferrite	
wt %	Weight percentage	
∞O	Strength contribution	MPa
σ_{Fe}	Strength of pure iron	MPa
σ_{ss}	Strength of solid solution	MPa
σ_c	Strength due to carbon in solid solution	MPa
π	Constant number (3.14)	
σ_w	Significance of the input in the neural-network	
σ	Yield strength	MPa
V_γ	Volume fraction of retained austenite	
X	Un-normalised value in the database	
$x_{min},\ x_{max}$	Minimum and maximum values in the database	
x_j	Normalised value in the database	
x^k	Set of inputs	
y^k	Set of corresponding network outputs	

O_y^k Uncertainty of fitting

Y A parameter which depends on specimen and crack geometry

Y Output of the neural network

$y^{(l)}$ Prediction obtained with the model l

Appendix A

[9]   C.-H. Hsu and T.-L. Chuang, "Influence of stepped austempering process on the fracture toughness of austempered ductile iron," *Metallurgical and Materials Transactions A*, vol. 32A, pp. 2509-2513, 2001.

[10]   *http://www.matweb.com/search/QuickText.aspx*.

[11]   B. Ule, V. Leskovsek, and B. Tuma, "Estimation of plain strain fracture toughness of AISI M2 steel from precracked round-bar specimens," *Engineering fracture Mechanics*, vol. 65, pp. 559-572, 2000.

[12]   M. Kurkel, G. S. Frankel, and R. M. Latanision, "Influence of plastic deformation on hydrogen transport in 1/4 Cr-1Mo steel," *Scripta Metallurgica*, vol. 16, pp. 455-459, 1982.

[13]   R. D. K. Misra, T. V. Balasubramanian, and P. R. Rao, "AES analysis of fracture toughness variation with heat treatment in an 18 Ni (250 grade) maraging steel," *Materials Science*, vol. 6, pp. 125-130, 1987.

[14]   M. R. Zhang and H. C. Gu, "Fracture toughness of nanostructured railway wheels," *Engineering Fracture Mechanics*, vol. 75, pp. 5113-5121, 2008.

[15]   S. K. Putatunda, "Influence of austempering temperature on microstructure and fracture toughness of a high-carbon, high-silicon and high- manganese cast steel," *Materials & Design*, vol. 24, pp. 435-443, 2003.

[16]   W. M. Garrison, "A micromechanistic interpretation of the influence of undissolved carbides on the fracture toughness of a low alloy steel," *Scripta Metallurgica*, vol. 2Q, pp. 633-636, 1986.

[17]   Z. Q. Mu and C. W. Lung, "Studies on the fractal dimension and fracture toughness of steel," *Applied Physics.*, vol. 21, pp. 848-850, 1988.

[18]   S. K. Putatunda, "Fracture toughness of a high carbon and high silicon steel " *Materials Science and Engineering A*, vol. A297, pp. 31-43, 2001.

[19]   W. Chang, "Applying similarity methods to fracture " *Engineering fracture Mechanics*, vol. 31, pp. 807-816, 1988.

[20]   V. Leskovsek and B. Ule, "Improved vacuum heat-treatment for fine-blanking tools from high-speed steel M2," *Journal of Materials Processing Technology*, vol. 82, pp. 89-94, 1998.

[21]   A. Fernandez-Vicent, M. Carsi, F. Penalba, E. Taleff, and O. A. Ruao, "Toughness dependence on the microstructural parameters for an ultrahigh carbon steel (1.3 wt.% C)," *Materials Science and Engineering A*, vol. 335, pp. 175-185, 2002.

[22] X. Z. Zhang and J. F. Knott, "Cleavage fracture in bainitic and martensitic microstructures," *Acta mater.*, vol. 47, pp. 3483-3495, 1999.

[23] J. R. Klepaczko and A. Solecki, "Effect of Tempering on Quasi-Static and impact fracture toughness and mechanical properties for 5140 H steel," *Metallurgical and Materials Transactions A*, vol. 15A, pp. 901-911, 1984.

[24] K. Nakazawa and G. Krauss, "Microstructure and fracture of 52100 steel," *Metallurgical Transactions A*, vol. 9, pp. 681-689, 1978.

[25] R. S. Hyde, G. Krauss, and D. K. Matlock, "Phoshorus and carbon segregation: Effects on fatigue and fracture of gas-carburized modified 4320 steel," *Metallurgical and Materials Transactions A*, vol. 1994, pp. 1229-1240, 1994.

[26] J. L. Youngblood and M. Raghavan, "Correlation of microstructure with mechanical properties of 300M steel " *Metallurgical Transactions A*, vol. 8 A, p 14391448, 1977.

[27] J. W. Bray, J. L. Maloney, K. S. Raghavan, and W. M. Garrison, "A comparison of the fracture behavior of two commercially produced heats of HY180 steel Differing in sulfide type," *Metallurgical Transactions A*, vol. 22 A, pp. 2277-2285, 1991.

[28] H. K. Obermeyer and G. Krauss, "Toughness and Intergranular fracture of simulated carburized case in EX-24 steel," *Heat treating*, vol. 1, pp. 31-39, 1980.

[29] J. Toribio, "Effect of cold drawing on evironmentally assisted cracking of cold-drawn steel," *Materials Science*, vol. 31, pp. 6015-6024, 1996.

[30] B. Lou and B. L. Averbach, "The effects of heat treatment on fracture toughness and fatigue crack growth rates in 440C and BG42 steels," *Metallurgical Transactions A*, vol. 14A, pp. 1899-1906, 1983.

[31] Y. He, K. Yang, W. Qu, F. Kong, and G. Su, "Strengthening and toughening of a 2800-MPa grade maraging steel," *Materials Letters*, vol. 56, pp. 763-769, 2002.

[32] W. M. Garrison, "A microstructural interpretation of the fracture strain and characteristic fracture distance," *Scripta Metallurgica*, vol. 18, pp. 583-586, 1984.

[33] D. Firrao, J. A. Begley, G. Silva, R. Robertil, and B. D. Benedetti, "The influence of notch root radius and austenitizing temperature on fracture appearance as-quenched charpy-v type AISI 4340 steel specimens," *Metallurgical Transactions A*, vol. 13A, pp. 1003-1013, 1982.

[34] L. C. A. Folch and F. M. Burdekin, "Application of coupled brittle-ductile model to study correlation between charpy energy and fracture

toughness values," *Engineering fracture Mechanics*, vol. 63, pp. 57-80, 1999.

[35] V. Leskovsek, B. Sustarsic, and G. Jutrisa, "The influence of austenitizing and tempering temperature on the hardness and fracture toughness of hot-worked H11 tool steel," *Journal of Materials Processing Technology*, vol. 178, pp. 328-334, 2006.

[36] J. M. Hyzak and I. M. Bernstein, "The role of microstructure on the strength and toughness of fully pearlitic steels," *METALLURGICAL TRANSACTIONS A*, vol. 7A, pp. 1217-1221, 1976.

[37] B. T. Timofeev, G. P. Karzov, A. A. Blumin, and V. V. Anikovsky, "Fracture toughness of 15X2MFA steel and its weldments," *International Journal of Pressure Vessels and Piping*, vol. 77, pp. 41-52, 2000.

[38] R. Ayer and P. M. Machmeier, "Transmission electron microscopy examination of hardening and toughness phenomena in aermet 100," *Metallurgical transactions A*, vol. 24A, pp. 1943-1955, 1993.

[39] C. Kim, J. I. Park, S. Lee, Y. C. Kim, N. J. Kim, and J. S. Yang, "Effects of alloying elements on microstructure hardness and fracture toughness of centrifugally cast high-speed steel rolls," *Metallurgical and Materials Transactions A*, vol. 36A, pp. 87-97, 2005.

[40] R. O. Ritchie, M. H. C. Cedeno, V. F. Zackay, and E. R. Parker, "Effect of silicon additions and retained austenite on stress corrosion cracking in ultrahigh strength steel," *Metallurgical Transactions A*, vol. 9A, pp. 35-40, 1978.

[41] R. O. Ritchie, "Influence of impurity segregation on temper embrittlement and on slow fatigue crack growth and threshold behavior in 300-M high strength steel," *Metallurgical Transactions A*, vol. 8A, p 1131, 1977.

[42] R. M. Horn and R. O. Ritchie, "Mechanisms of tempered martensite embrittlement in low alloy steels," *Metallurgical Transactions A*, vol. 9A, pp. 1039-1053, 1978.

[43] *Handbook, Fatigue and fracture*, vol. 19.

[44] A. R. Johnson, "Fracture toughness of AISI M2 and AISI M7 high-speed steels," *Metallurgical Transactions A*, vol. 8A, pp. 891-897, 1977.

[45] C.-H. Hsu, Y.-H. Shy, Y.-H. Yu, and S.-C. Lee, "Effect of austempering heat treatment on fracture toughness of copper alloyed gray iron " *Materials Chemistry and Physics*, vol. 63, pp. 75-81, 2000.

[46] C. N. Sastry, Khalid, H. Khan, and W. E. Wood, "Mechanical stability of retained austenite in quenched and tempered AISI 4340 steel," *Metallurgical Transactions A*, vol. 13A, pp. 676-680, 1982.

[47] C. Garcia-Mateo, M. Peet, F. G. Caballero, and H. K. D. H. Bhadeshia, "Tempering of hard mixture of bainitic ferrite and austenite," *Materials Science and Technology*, vol. 20, pp. 814-818, 2004.

[48] P. P. Rao and S. K. Putatunda, "Dependence of fracture toughness of austempered ductile iron on austempering temperature," *Metallurgical and Materials Transactions A*, vol. 29A, pp. 3005-3016, 1998.

[49] S. Lee, C.Hsun, C. Chang, and H.Feng, "Influence of casting size and graphite nodule refinement of fracture toughness of Autempered ductile iron," *Metallurgical and Materials Transactions A*, vol. 29A, p 25112521, 1998.

[50] P. P. Rao and S. K. Putatunda, "Investigation on the fracture toughness of austempered ductile iron alloy with chromium," *Materials Science and Engineering A*, vol. 346, pp. 254-265, 2003.

[51] J. Yang and S. K. Putatunda, "Improvement in strength and toughness of austempered ductile cast iron by a novel two-step austempering process " *Materials & Design*, vol. 25, pp. 219-230, 2004.

[52] P. P. Rao and S. K. Putatunda, "Investigations on the fracture toughness of austempered ductile irons austenitized at different temperatures," *Materials Science and Engineering A*, vol. 349, pp. 136-149, 2003.

[53] L. Bartosiewicz, I. Singh, F. A. Alberts, A. R. Krause, and S. K. Putatunda, "The influence of chromium on mechanical properties of austempered ductile cast iron," *Materials Engineering and Performance*, vol. 4(1), pp. 90-94, 1995.

[54] X. Chen and Y. Li, "Fracture toughness improvemet of austempered high silicon steel by titanium vanadium and rare earth elements modification," *Materials Science and Engineering A*, vol. 444, pp. 298-305, 2007.

[55] P. W. Shelton and A. A. Bonner, "The effect of copper additions to the mechanical properties of austempered ductile iron (ADI)," *Materials processing technology*, vol. 173, pp. 269-274, 2006.

[56] V. Leskovsek, B. Ule, and B. Liscic, "Relations between fracture toughness, hardness and microstructure of vacuum heat-treated high-speed steel," *Journal of Materials Processing Technology*, vol. 127, pp. 298-308, 2002.

[57] H. A. Aglan, Z. Y. Liu, M. F. Hassan, and A. Fateh, "Mechanical and fracture behavior of bainitic rail steel," *Journal of Materials Processing Technology*, vol. 151, pp. 268-274, 2004.

[58] Y. Ochi and A. J. McEvily, "AN EVALUATION OF THE FATIGUE CRACK-GROWTH AND FRACTURE-TOUGHNESS CHARACTERISTICS OF RAIL STEELS," *Engineering Fracture Mechanics*, vol. 29, pp. 159-172, 1988.

[59] K. Sawley and J. Kristan, "Development of bainitic rail steels with potential resistance to rolling contact fatigue," *Fatigue & Fracture of Engineering Materials & Structures*, vol. 26, pp. 1019-1029, 2003.

[60] S. K. Putatunda, "Development of an austenitic structural structural steel " *Materials & Design*, vol. 26, pp. 534-544, 2005.

[61] R. O. Ritchie, B. Francis, and W. L. Server, "Evaluation of toughness in AISI 4340 alloy steel austenitized at low and high tempertures," *Metallurgical Transactions A*, vol. 7A, pp. 831-838, 1976.

[62] R. O. Ritchie, V. A. Chang, and N. E. Paton, "Influence of retained austenite on fatigue crack propagation in HP 9-4-20 high strength alloy steel," *Fatigue of Engineering Materials and structures*, vol. 1, pp. 107-121, 1979.

[63] T. S. Thomas and C. F. Hickey, "Mechanical property characterization of ESR 4353 steel with a comparison to ESR 4340 steel," *Heat Treated*, vol. 7, pp. 49-55, 1989.

[64] R. Kerr, F. Solana, I. M. Bernstein, and A. W. Thompson, "Microstructural effects on the stress corrosion cracking behavior of medium and high strength steels " *Metallurgical Transactions A*, vol. 18A, pp. 1011-1019, 1987.

[65] R. J. Kar, R. M. Horn, and V. F. Zackay, "The effect of heat treatment on microstructure and mechanical properties in 52100 steel," *Metallurgical Transactions A*, vol. 10A, pp. 1711-1717, 1979.

[66] J. Pacyna, "The microstructure and properties of the new bainitic rail steels," *Achievements in Materials and Manufacturing Engineering rail steel*, vol. 28, pp. 19-22, 2008.

[67] H. A. Aglan and M. Fateh, "Fracture and fatigue crack growth analysis of rail steels," *Journal of Mechanics of Materials and Structures*, vol. 2, pp. 335-346, 2007.

[68] A. H. Elsayed, M. M. Megahed, A. A. Saek, and K. M. Abouelela, "Fracture toughness characterization of austempered ductile iron produced using both conventional and two-step austempering processes," *Materials & Design*, vol. 30, pp. 1866-1877, 2009.

[69] K. Ravishankar and K. R. Udupa, *Development of austempered ductile iron for high tensile and fracture toughness by two step austempering process*, Conference: Proceeding of 68th word foundy Congress, 2008.

[70] A. D. Basso, R. A. Martinez, and J. A. Sikora, "Influence of austenitising and austempering temperatures on microstructure and properties of dual phase ADI " *Materials Science and Technology*, vol. 23, pp. 1321-1326, 2007.

[71] S. K. Putatunda, M. T. Ambooken, and B. J. Pullum, "Thermo-magnetic processing of ductile cast iron " *Materials Science and Engineering A*, vol. 460-461, 2007.

[72] S. K. Putatunda, A. V. Singar, R. Tackett, and G. Lawes, "Development of a high strength high toughness ausferritc steel," *Materials Science and Engineering A*, vol. 513-514, pp. 329-339, 2009.

[73] S. Tarafder, S. Sivaprasad, and V. R. Ranganath, "Comparative assessment of fatigue and fracture behaviour of cast and forged railway wheels," *Fatigue & Fracture of Engineering Materials & Structures*, vol. 30, pp. 863-876, 2007.

[74] G. Y. Lai, W. E. Wood, R. A. Clark, V. F. Zackay, and E. R. Parker, "The effect of austenitizing temperature on the microstructure and mechanical properties," *Metallurgical Transactions*, vol. 5, pp. 1663-1670, 1974.

[75] Y. Tomita, "Effect of microstructure on plane strain fracture toughness of AISI 4340 steel," *Metallurgical Transactions A*, vol. 19A, pp. 2513-2521, 1988.

[76] J. M. Beswick, "Fracture and fatigue crack propagation properties of hardened 52100 steel," *Metallurgical Transactions A*, vol. 20A, pp. 1961-1973, 1989.

[77] W. M. Garrison, "The effect of silicon and nickel additions on the sulfide spacing and fracture toughness of a 0.4 carbon low alloy steel," *Metallurgical and Materials Transactions A*, vol. 17A, pp. 669-678, 1986.

[78] T. B. Cox and J. R. Low, "An investingation of the plastic fracture of AISI 4340," *Metallurgical Transactions*, vol. 5, 1974.

[79] E. R. Parker and R. F. Mehl, "Interrelations of compositions transformation kinetics morphology and mechanical properties of alloy Steels," *Metallurgical and Materials Transactions A*, vol. 8A, pp. 1025-1042, 1977.

[80] S. C. Lee and F. J. Worzala, "Fracture-behavior of AISI M-2 high-speed tool steel," *Metallurgical Transactions a-Physical Metallurgy and Materials Science*, vol. 12, pp. 1477-1484, 1981.

[81] C. F. Hickey and A. A. Anctil, "Split heat mechanical property comparison of ESR and VAR 4340 steel," *Heat treating*, vol. 4, pp. 177-183, 1985.

Appendix A

[82] B. Z. Margolin, V. A. Shvetsova, A. G. Gulenko, A. V. Ilyin, V. A. Nikolaev, and V. I. Smirnov, "Fracture toughness prediction for a reactor pressure vessel steel in the initial and highly embrittled states with the master curve approch and a probabilistic model," *International Journal of Pressure Vessels and Piping*, vol. 79, pp. 219-231, 2002.

[83] Y. Song, Q. Luo, Q. Chen, and Y. Chen, "Effects of Re-B modification on the strength and toughness of 30Cr Mn 2Si cast steel," *Materials science and Technology*, vol. 29, pp. 1492-1496, 1994.

[84] Y. Tomita, "Improved lower temperature fracture toughness of ultrahigh strength 4340 steel through modified heat treatment," *Metallurgical Transactions A*, vol. 18A, pp. 1495-1501, 1987.

[85] Y. Tomita, "Review Morphology control of ductile second phase and improveed mechanical properties in high-strength low-alloy steels with mixed structure " *Materials Science*, vol. 27, pp. 1705-1715, 1992.

[86] M. Jahazi and G. Ebrahimi, "The influence of flow-forming parameters and microstructure on the quality of a D6ac steel," *Journal of Materials Processing Technology*, vol. 103, pp. 362-366, 2000.

[87] V. P. Raghupathy, V. Srinivasan, and H. Krishnan, "The effect of suphid inclusion on fracture toughness and fatigue crack growth in 12 wt% Cr steels," *Materials Science*, vol. 17, pp. 2112-2126, 1982.

[88] G. M. Aiah, M. Srinivas, J. M. Murthy, and P. Ramarao, "Development of an ultra-high-strength low-alloy NiSiCrCoMo steel," *Bulletin of Material Science*, vol. 17, pp. 73-86, 1994.

[89] R. Hamano, "The effect of the precipitation of coherent and incoherent precipitates on the ductility and toughness of high-strength steel," *Metallurgical transactions A*, vol. 24A, pp. 127-138, 1993.

[90] R. J. Barnhurst and J. E. Gruzleski, "Fracture toughness and its development in high purity cast carbon and low alloy steels," *Metallurgical Transactions A*, vol. 16 A, pp. 613-622, 1985.

[91] C. Y. Li, P. M. Talda, and R. P. Wwi, "The effect of environments on fatigue-crack propagation in an ultra-high-strength steel " *International Journal of Fatigue*, vol. 3, pp. 29-36, 1966.

[92] *http://www.freepatentsonline.com/4076525.pdf*.

[93]
      "http://www.efunda.com/materials/alloys/tool_steels/show_tool.cfm?ID=AISI_H11&show_prop=all&Page_Title=AISI%20H11," vol.

[94] R. J. Sanford, *Fatigue and Fracture, fifteenth symposium* USA, http://books.google.com.sa/books?id=JW60YBcuZloC&printsec=frontcover&dq=fracture+mechanics+R.+J.+Sanford&source=bl&ots=XsaPkKbWFq&sig=ovdiZjxkFc9ZHCjWlIek2JHOS6c&hl=ar&ei=EN-

lTMqtA8u64Qag19CLDQ&sa=X&oi=book_result&ct=result&resnum=1&ved=0CAYQ6AEwAA#v=onepage&q&f=false,1984.

[95] *http://www-gmap.mecanica.ufrgs.br/~ignacio/%5B1%5DBatista2008.pdf*.

[96] *http://www.shotpeener.com/library/pdf/1973003.pdf*.

[97] W. F. Bron, *Review of developments in plane strain fracture toughness testing*, American society for testing and materials national aeronautics and space administration, 1970.